UNIVERSITY OF NAMUR

Research Center for the Physic of Mater and Radiation

Laboratoire de Physique des Matériaux Electroniques

Electrical, Optical and Structural Properties Of Functional Multilayers On Steel Sheets For Potential Applications In Cu(In,Ga)Se_2 Solar Cells

---

Dissertation

For The Degree Of

DOCTORATE IN SCIENCE

Presented by

Dodji AMOUZOU

[January 2014]

Accepted on the recommendation of:

Prof. Siva Sivananthan (University of Illinois, Chicago, Examiner)

Prof. Jean-Pierre Raskin (University of Louvain-la-Neuve, Examiner)

Prof. Guy Terwagne (University of Namur, Examiner)

Dr. Lionel Fourdrinier (CRM-Group, Industry Advisor)

Prof. Laurent Houssiau (University of Namur, Chairman)

Prof. Robert Sporken (University of Namur, Promoter)

Abstract

$Cu(In,Ga)Se_2$, in short CIGS, solar cells have received considerable attention among photovoltaic solar cells because of their high conversion efficiency, flexibility and lightweight. The challenge in CIGS technology nowadays is not only to enhance performances but also to find low cost processing options. The use of CIGS modules built from monolithic interconnected cells on steel sheets is a promising solution; however it requires an additional dielectric layer interposed between the substrate and the entire active stack. Thus, the focus of this thesis was to elaborate a novel dielectric systems prepared on steel substrates and to optimize molybdenum layers as contacts for the fabrication of "high temperature" flexible CIGS solar cells.

Polysilazane hybrid polymers were identified and explored to act as a dielectric layer for CIGS solar cells. Coatings were performed on stainless steel substrates using a straightforward "bar coating" deposition method which is suitable for industrial rolling processes. The problem with polysilazane coatings is that they often suffer from thermal instability and cracking due to the high annealing temperature required for growing the CIGS absorbing layer. Indeed, our thermal analysis reveals an important mass loss of around 25 wt. % for type of polysilazane we use. The mass reduction was assigned to chemical transformations of the polymer evidenced by volatilization of different gases and evolution of solvent. Such degradations show a severe weakening of the dielectric strength of polysilazane coatings. It was shown that polysilazanes can be stabilized after annealing at 550°C. Polysilazane single layers with a thickness below 2 µm are crack-free even after annealing but, unfortunately do not fulfill the dielectric requirements. Single layers with a thickness higher than 2 µm systematically cracked after annealing.

With a subtle combination of three layers of polysilazane and a sputtered SiO_xAl_y layer we succeeded in growing a crack-free dielectric stack with total thickness of more or less 4 µm. Constant voltage stress measurements performed on metal-insulating-metal capacitors reveal that such dielectric stacks can tolerate an applied voltage of 1000 V before annealing and 500 V after annealing at 500°C.

Optimization of Mo films was then performed on dielectric stacks and a method to produce crack-free and well-adhered Mo films was established. Two solutions were found and each solution was obtained by combining two different layers. Both solutions pass adhesion testing and exhibit very low sheet resistance required for Mo back contacts.

The interface between a set of Mo films and polysilazane was also studied. There seems to be a link between Mo-O-Si covalent bonds and good adhesion at the interface. Adhesion loss observed for some Mo/polysilazane samples occurred due to decohesion in polysilazane itself. The decohesion is assigned to the weakening of polysilazane due to the formation of molybdenum carbide at the interface.

Finally, the analysis of steel modified by ultra-thin polysilazane reveals the presence of Cr-O-Si and Fe-O-Si covalent bonds which may explain the good adhesion observed with polysilazane/steel samples.

Contents

Contents

Remerciements

Cette thèse de doctorat a été réalisée au Centre de Recherches et Développement CRM-Group anciennement Centre de Recherches et Développements d'ArcelorMittal de Liège et au Laboratoire de Physique des Matériaux Electroniques (LPME) de l'Université de Namur. Je tiens donc à remercier tout d'abord Monsieur Michel Beguin, directeur du CRM-Group à l'époque de mon stage de fin d'études et au début de ma thèse, Monsieur Jean-Claude Herman, directeur actuel du CRM-Group et le Professeur Robert Sporken, 1ier Vice-Recteur de l'Université de Namur et directeur du LPME pour m'avoir accueilli dans leurs laboratoires.

Je remercie le Docteur Fabrizio Maseri, directeur du service Advanced Nanocoatings & Energy (ANAE) et de la plateforme PVSTEEL du CRM-Group pour m'avoir proposé la thématique de recherche et accepté dans son service. Malgré ses importantes responsabilités, M. Maseri a suivi avec attention ce travail. Ses conseils et propositions m'ont permis de bien avancer dans le travail.

Je suis particulièrement reconnaissant envers le Professeur R. Sporken, promoteur de ma thèse, pour m'avoir encadré malgré ses importantes charges de 1ier Vice-Recteur (d'abord doyen puis vice-recteur…). Un tout grand merci à M. Sporken pour m'avoir offert la possibilité de réaliser ce projet sous sa responsabilité. Sa compétence et sa grande connaissance des techniques d'analyse dans le domaine de l'ingénierie de surface et interfaces des matériaux m'ont été d'une grande utilité.

Je remercie le Professeur Laurent Houssiau qui me fait l'honneur de présider le jury. Mes remerciements vont également au Professeur Siva Sivananthan pour avoir accepté de faire partie du jury de ma thèse et fait le déplacement de Chicago. J'adresse ma profonde reconnaissance au Professeur Jean-Pierre Raskin, au Professeur Guy Terwagne et au Docteur Lionel Fourdrinier pour avoir accepté de participer au jury de ma thèse et de juger mon travail.

Mes remerciements vont encore au Docteur Lionel Fourdrinier puis à M. Jean-Baptiste Richir, au Docteur Philippe Guaino et au Docteur Jacques Dumont pour le temps qu'ils ont consacré à m'encadrer, me conseiller et me montrer le métier de chercheur.

J'adresse encore mes remerciements au Professeur Jean-Pierre Raskin, au Professeur Isabelle Huynen pour m'avoir permis de réaliser une partie des caractérisations électriques au centre de recherche ICTEAM et plus particulièrement à Mlle Aline Emplit pour les caractérisations électriques à basses fréquences.

Mes reconnaissances vont au Professeur Duy Nguyen pour m'avoir aidé dans la modélisation et l'interprétation des mesures électriques.

Je remercie très sincèrement toux ceux et celles sans qui la plupart des caractérisations réalisées au cours de ce travail n'auraient pu avoir lieu :

- *au CRM-Group : C. Le Pen, D. Alain, X. Vanden Eynde, S. Renaud, V. Raisi, G. Cajot, V. Pire, S. Galluzzo, L. Confetti, Vervort Laurent, P. Hanquet, J. Brasseur, A.Ceunen , P. Lambotte, P. Bourgignon ;*
- *et à l'Université de Namur : E. Gennart, P. Louette, N. Mine, C. Meunier, L. Nittler, F. Cecchet, Y. Caudano, F. Come, L. Avril,*
  pour m'avoir formé sur les techniques d'élaboration et d'analyses, pour avoir réalisé des caractérisations avec moi, pour leurs conseils, leurs soutiens techniques et surtout pour l'intérêt qu'ils ont portés à mon travail.

Je tiens à remercier très sincèrement Madame et Monsieur Ghijsen pour leur aide précieuse dans la relecture de ce manuscrit.

J'adresse un tout grand merci à tous les membres du LPME, anciens et comme nouveaux que j'ai croisés: Etienne Gennart, Fernande Frising, Frédéric Joucken, Thanh Trung Pham, Jacques Dumont, Mac Mugumaoderha, CedricVolcke, Tijani Tabrrant, Thomas Seldrum pour l'excellente ambiance de travail et pour leur soutien scientifique.

Je tiens à mentionner le plaisir que j'ai eu à travailler au CRM-Group et plus particulièrement dans le service ANAE ; un tout grand merci à tous les membres. Je remercie tout particulièrement David Vicky, un collègue du bureau pour nos échanges et l'attention qu'il a toujours porté à mon égard. Je remercie également : Samy Muthu, Adeline Lafort, Lucie Gaouyat, Audrey Monier, Frédéric Mirabella, Aline Teillet, Claire Poirier pour les échanges et leur encouragement.

Egalement merci à mes amis et « compagnons du repas de midi » : David Ponce, Arnaud Collet, Caroline Quoilin, Innocent Niyonzima, Harona Diara, François Finet pour nos diverses discussions, la bonne humeur, leurs encouragements et les agréables moments passés ensemble.

J'exprime ma profonde gratitude à M. Messan Abbevi et sa femme Chantale pour tout le soutien qu'ils m'ont apporté depuis que je suis arrivé à Liège. Un spécial merci à eux.

A mes amis de NOVINYO asbl: M. Koffi Quenum, Philippe Amedodji, Claude Agbo, Adjévi Laclé, un grand merci pour m'avoir accepté comme un frère dans la communauté togolaise de Liège et permis d'apporter ma modeste contribution dans le Conseil d'Administration de l'Asbl en me confiant le rôle de secrétaire.

Egalement merci à tous les membres du Togodo Art & Dancing Club : Joel et sa femme Brigitte, Joyce, Brigitte, Sarah, Jean-Philippe, Basile, John, Sassou, Eric, Marc, Emmanuel, Cédric et sa femme Stéphanie, Muriel, Delphine pour m'avoir permis de découvrir et pratiquer les danses traditionnelles de chez moi, le Togo. Avec eux, je suis certain d'avoir le sourire, vous restez gravés dans ma mémoire.

Merci du fond du cœur à Clotilde, Anick, Sonia, Amadou, Clément, Lino, Nelly, Christelle, Josiane, Caroline, Stéphanie, Armande, Romaric, pour tout ce que vous avez été pour moi, votre soutien, votre encouragement, nos discussions, votre amour. J'ai partagé d'agréables moments avec vous. Merci.

Toute ma gratitude à mon cousin Yaovi Gagou et sa femme Eliane pour l'incroyable soutien qu'ils m'ont apporté durant mes années passées en France. A mes cousins Denis et sa femme Sidonie et Joseph, Richard, Ben, Ayi, Santos et sa femme Sylvie pour leur aide et encouragement. Merci.

Je ne peux passer sous silence l'énorme soutien que ma famille m'a donné, qui loin des yeux, certes, a toujours été près de mon cœur. ***Papa****, pour tes conseils, ton encouragement et tes efforts envers moi depuis mon enfance, Merci. Merci* ***Maman*** *pour ta tendresse, tes conseils, tes prières ; tu sais que je t'aime. Vous devez être fiers. Merci Simplice pour ton important rôle d'aîné de famille « au sens africain du terme », pour tes soutiens à tous les niveaux. Mes frères : Auger, Barthélémy, David, Ygnace, Marlain, Charles et à ma sœur Jolie Bésina pour votre*

fraternité, amour et l'unité bien que nous vivions dans de différents pays et loin les uns les autres.

Abbreviations

Acronyms	**Full name**
AFM	Atomic Force Microscopy
ATR	Attenuated Total Reflectance
CCD	Charge Coupled Device
CIGS	Copper Indium Gallium Diselenide
CTE	Coefficient of Thermal Expansion
CVD	Chemical Vapor Deposition
CVS	Constant Voltage Stress
DBL	Diffusion Barrier Layer
DSC	Differential Scanning Calorimetry
F-N	Fowler Nordheim
FTIR	Fourier Transformed Infrared
GDOES	Glow Discharge Optical Emission Spectroscopy
HDMSO	Hexamethyl Disiloxane
HVPS	High Voltage Power Supply
MIM	Metal Insulating Metal
OPSZ	Organic Polysilazane
OPV	Organic Photovoltaic
PCBM	Phenyl C61 Butyric acid Methyl Ester
PECVD	Plasma Enhanced Chemical Vapor Deposition
PCD	Polymer Derived Ceramic
PHPS	Perhydropolysilazane
PMT	Photo Multipliers Tube
PSZ	Polysilazane
P3HT	Poly-3-Hexylt Thiophene
PV	Photovoltaic
PVD	Physical Vapor Deposition
SEM	Scanning Electron Spectroscopy

SCLC	Space Charge Limited Current
SIMS	Secondary Ions Mass Spectroscopy
SLG	Soda Lime Glass
SS	Stainless Steel
TCO	Transparent Conducting Oxide
TF	Thin Film
XRD	X-ray Diffraction

The list of my publications

Article 1: Adhesion, resistivity and structural, optical properties of molybdenum on steel sheet coated with barrier layer done by sol–gel for CIGS solar cells.

D. Amouzou, J. Dumont, L. Fourdrinier, J-B. Richir, F. Maseri, R. Sporken, Thin Solid Films, 531-15 (2013) 535/540.

Article 2: Dielectric and diffusion barrier multilayer for CIGS solar cells integration on stainless steel sheet

D. Amouzou, P. Guaino, L. Fourdrinier, J-B Richir, F. Maseri, R. Sporken, Thin Solid Films 542 (2013) 270–275.

Article 3: Novel high thermal barrier layers for flexible CIGS solar cells on stainless steel substrates

D. *Amouzou, P. Guaino, J. Dumont, L. Fourdrinier,J-B Richir, R. Sporken, F. Maseri, Proceeding of Photovoltaic Specialists Conference (PVSC), 2011 37th IEEE, (2011) 1229/1234, doi: 10.1109/PVSC.2011.6186179.*

Article 4: XPS and IRRAS investigations of the interface of steel/hybrid-sol-gel coatings *D. Amouzou, L. Fourdrinier, J-B. Richir, R. Sporken, under correction in Journal of Applied Surface Science.*

CHAPTER 1
Flexible Cu(In,Ga)Se_2 Technology

I.1. Introduction

In this chapter, we introduce the relevant technology and the basic operating principle of CIGS solar cells. First, challenges related to material aspects for integration of CIGS solar cells on steel sheets are documented. Second, the state of the art of important results reported on flexible CIGS is reviewed. Finally, the requirements of monolithical integration of CIGS solar cells on metal substrates and progress in the use of solid dielectric systems as barrier layers are highlighted to help understanding our research presented in chapters II – IV.

I. 2. CIGS solar cells

I. 2.1. Device structure and operating principle of CIGS solar cells

A classical device structure of CIGS solar cells is given in figure 1. Most CIGS solar cells are formed in a configuration where processing starts from the substrate, using the following procedure:

- The back contact commonly used is the sputtered molybdenum film and it has to form a non-blocking charge carrier contact with the CIGS absorbing layer. Mo was chosen because it does not add n-type dopant to compensate p-type doped CIGS [1];

- The p-type CIGS absorbing layer with a typical thickness of 1 to 2 µm is deposited by various processes that can be categorized into non vacuum (e.g. electrodeposition or ink deposition) [2] and vacuum (co-evaporation and sputtering) techniques, both deposition techniques may be combined with selenization [3,4, 5] based deposition methods. The band-gap

energy of the CIGS absorber is variable [6]: by varying the Ga/(Ga + In) ratio from 0 to 1, it was reported in [7] that the band gap energy can vary from 1.02 eV to 1.66 eV.

- The n-type CdS buffer and ZnO window layer are successively deposited on the top of the CIGS absorbing layer using chemical bath deposition and sputtering, respectively. ZnO layers are often realized in a bi-layer configuration of intrinsic (50 nm-thick) and Al-doped (500 - 700 nm-thick) transparent conducting oxide (TCO), which plays the role of top electrode. A review of buffer and window layers, including an evaluation of possible alternatives, was conducted by Pudov et al. [8]. Currently, a metal grid such as Ni-Al is deposited on the TCO layer for current collection and finally anti-reflection coatings such MgF_2 complete the cell [9].

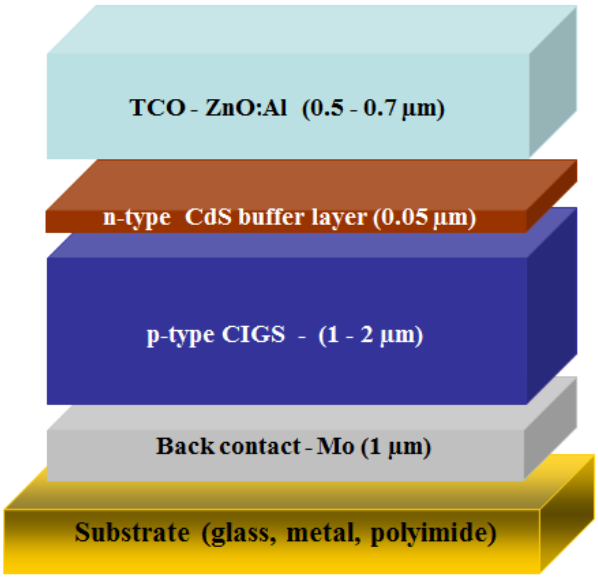

Figure 1: Classical structure of CIGS solar cells.

CIGS based photovoltaic solar cells convert the sun light (photon) into direct current. Upon illumination, photons with an energy higher than the band-gap of the CIGS absorbing layer are absorbed leading to the generation of electron-hole pairs called excitons as displayed in figure 2. The ultra-thin n-type semiconductor coating (i.e.: CdS) is required to establish a p–n junction with the CIGS absorbing layer. The built-in electric field is then created at the interface of the p/n junction due to the depletion; it ensures a role of excitons separation and injecting of charges into either n-type or p-type semiconductors. Electrons photo-generated in depletion region are

transported in electron acceptor while holes are propelled into the absorbing layer leading to a flow of charges. When photon absorption takes place in quasi-neutral region of each semiconductor, quasi-particles should diffuse into the space-charge region before they can be separated. Some photo-excited electrons will be lost due to recombination; especially the photo-excitation which takes place far from p/n junction is more affected. Bulk, interface; and trap recombination also strongly reduce the quantity of charge collected at the interface [10]. M. Gloeckler et al. used numerical simulation tools to evaluate the effects of an increase in bulk and interface recombination on absorber band gaps [11]. It was demonstrated that this recombination can limit the open voltage circuit of the device (V_{oc}) which is shown to decrease with band gap. Their results suggest that typical window/buffer layer materials for low-band-gap CIGS materials will not allow high device efficiency for wide-band-gap CIGS. The band gap of the buffer layer should be wide to allow incoming radiation easily transmitted into the absorber.

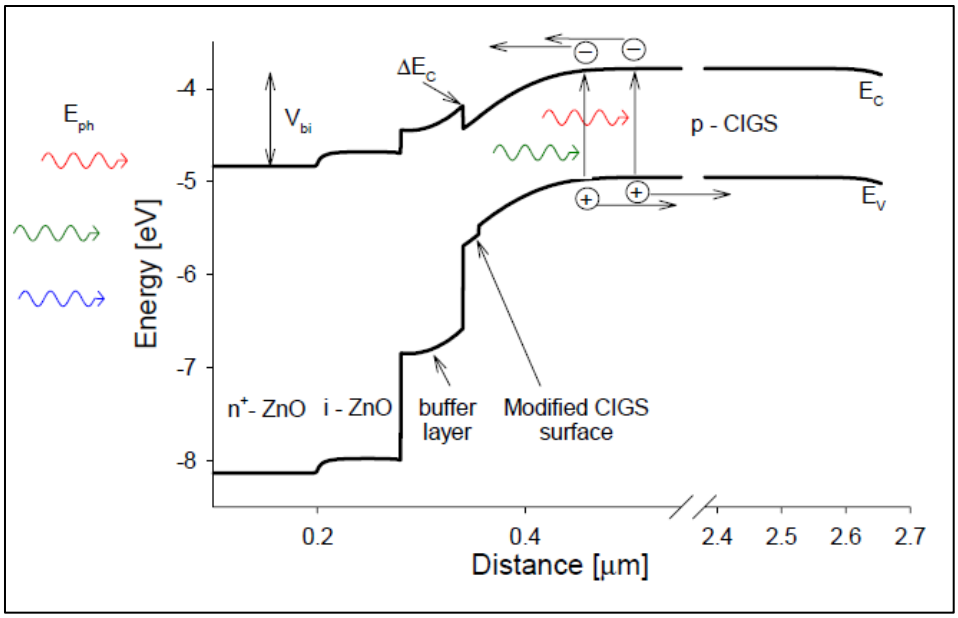

Figure 2: Band diagram of CIGS solar cells [8].

Naturally, for effective collection of charge carriers, electrode materials which exhibit low sheet resistance and form an ohmic contact with the corresponding semiconductor are preferred. In addition, the front contact should be as transparent as possible to the incident radiation.

I.2.2. Growth of CIGS layers

The crystal structure of Cu-In-Ga-Se systems is a chalcopyrite. A chalcopyrite unit cell is tetragonal and corresponds to two stacked zinc blende unit cells, where metal atoms are ordered as shown in figure 3. Each Se atom is bonded to two Cu and two In atoms and each metal atom has four Se atoms as nearest neighbors. A partial substitution of In by Ga in $CuInSe_2$ leads to the structure of Cu(In,Ga)Se_2. Discussion on chalcopyrite structures can be found in the well documented work of Stambery in [12].

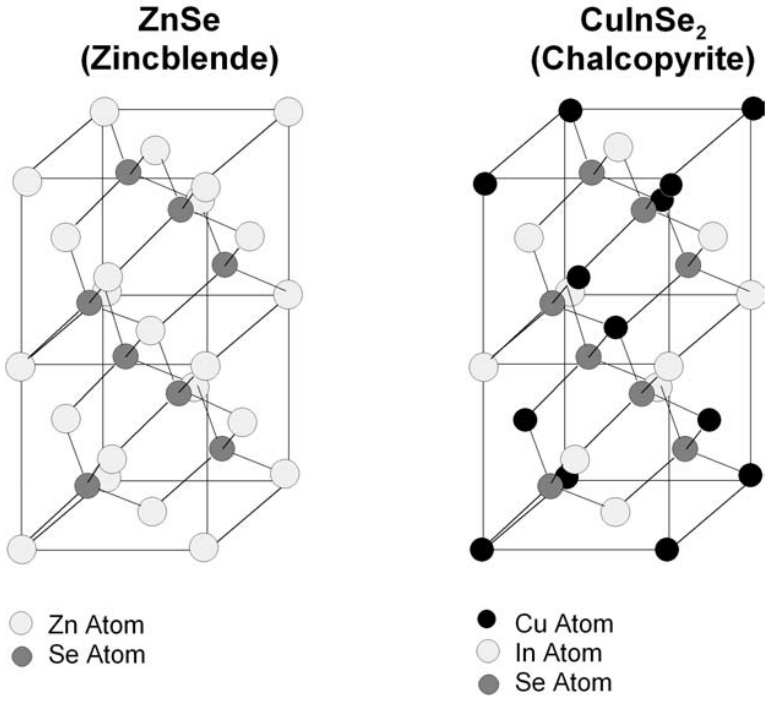

Figure 3: Unit cells of ZnSe (zinc blende structure) at the left and $CuInSe_2$ (chalcopyrite) at the right [9].

Considering the phase diagram helps in understanding of the growth of CIGS quaternary semiconductor and especially the reasons of the high temperature involved in the fabrication of CIGS solar cells [13].

As presented in [9], a phase diagram of CIGS is derived from the well-known ternary CIS phase diagram which can be obtained with Cu_2Se–In_2Se_3binary compounds. Authors of reference [9]

show that the phase of interest in the Cu–In–Se systems for solar cells is the δ- phase and the transformation of Cu-In-Se ternary compound into δ-CIS occurs around 800°C.

The structure of δ-phase is also referred as sphalerite and differs from chalcopyrite in the fact that Cu and In atoms are randomly distributed on cation sites.

One of problems met with CIS ternary and CIGS quaternary systems is the difficulty to obtain monophasic compositions (table 1) [14]. Beak et al. [15] worked on the growth of CIGS films and reported that metallic precursors react to form the compound and the expected self-mixing process occurs during annealing at high temperature, producing a stoichiometric composition. To obtain a monophasic compound and the appropriate stoichiometric phases, a high temperature is required. This explains why high temperature treatments are involved in current CIGS deposition methods [16,17,18].

Table 1: Different phases detected at various temperatures [14].

Temperature (°C)	Detected phase
250	CuSe, In, Se, Cu, In_2Se_3, InSe, GaSe
350 - 450	CuSe, In, Se, InSe, In_2Se_3, GaSe, $CuInSe_2$, $CuGa_{0.3}In_{0.7}Se_2$
550	$CuGa_{0.3}In_{0.7}Se_2$, CuSe, Se, In, GaSe; InSe, $CuInSe_2$
725 - 825	$CuGa_{0.3}In_{0.7}Se_2$, CuSe, Cu_2Se, $CuInSe_2$, $CuGa_{0.5}In_{0.5}Se_2$
925	$CuGa_{0.3}In_{0.7}Se_2$, $CuInSe_2$, CuSe
1025 - 1100	$CuGa_{0.3}In_{0.7}Se_2$, $CuInSe_2$
1200	$CuGa_{0.3}In_{0.7}Se_2$

The most widely and successfully employed deposition method is co-evaporation which permits to obtain efficient CIGS solar cells [19]. In co-evaporation all the four constituent elements are simultaneously deposited onto the substrate and the CIGS layer is formed in a single step. An evolution of this method is the sequential deposition of CIGS constituent atoms known as a three

stage process. In this method, the procedure consists in the deposition of In, Ga, and Se elements at a low substrate temperature plus Cu and Se which are deposited at higher substrate temperature (500 – 600°C) to form Cu-rich CIGS films [20]. The main advantage of these processes is a good control of the composition of the resulting absorbing layer. CIGS solar modules from this process easily reach efficiency of 12 – 13 % [21] and the record efficiency of 15.7 % is achieved by Miasolé [22] with modules of one square meter in size.

Another vacuum based method often used to obtain CIGS layer is based on the post-selenization of Cu, In, and Ga metallic precursors deposited by sputtering [23]. In this case, the step of selenization can be prepared by annealing process such as rapid thermal processing and is usually carried out at 450 – 600°C under selenium or selenium hydride (H_2Se) atmosphere. Modules obtained with post-selenization achieve an efficiency of 16.0 % [24]. One-step sputtered CIGS films deposition method has also been explored [25].

For solution based deposition methods, recent studies reported a fabrication of CIGS absorbing layer by using electrodeposition and nanoparticle-ink. The most important and recent progresses in electrodeposited CIGS absorbing layer are reviewed in [26]. The procedure of CIGS deposition using inkjet can be found in [27,28]. Others nanoparticle-based processes sometimes employed consist in a synthesis of CIGS powders [29] using a mechanical alloying method [30]. For latter methods, sintering is required to help in densification of precursor films.

Even if important efforts are ongoing to develop low temperature process [31,32] for CIGS solar cells, high thermal treatments steps are still essential in the standard deposition techniques. As a consequence, substrates used for the growth of efficient CIGS layer today have to tolerate temperatures up to 550°C; this makes current technologies especially hard and limits the choice of suitable substrates. The following sections will be focused on possibilities to the use of flexible substrates for CIGS solar cells with respect to the aims of the thesis.

I.3. Flexible substrates for CIGS technology

The standard substrate used for the fabrication of efficient CIGS solar cells is soda lime glass (SLG). The main advantage of SLG is its thermal expansion coefficient (CTE) which matches that of CIGS layer. Additionally, SLG substrates contain sodium, Na [33]; this is a key advantage because Na has demonstrated positive impacts on performances of CIGS solar cells.

Indeed, it was shown that the incorporation of 0.1 at. % of Na positively influences the growth of CIGS layer and the band gap grading thereby increases performances of cells [34]. Drawbacks of SLG substrate are its rigidity which limits potential applications and the lower stability at temperatures above 500°C limiting its applicability to lower temperature processing.

To benefit from mechanical properties of CIGS thin layers such as their flexibility, technological aspects of flexible CIGS solar cells have been explored [35]. The flexibility of the CIGS material eases the use of a large variety of substrates which can be classified into two categories: metallic and polymeric substrates [36 , 37 , 38]. In addition to the fact that substrates should be commercially available at reasonable cost, the main requirements for all flexible substrates can be:

- high thermal stability to allow high thermal treatments required for efficient cells;
- appropriate or adapted coefficient of thermal expansion (CTE); mismatched CTEs can lead to adhesion loss;
- appropriate surface roughness to prevent shunts;
- no surface defects;
- high chemical inertia in Se atmosphere;
- suitability for a rolling process.

To date, there is no raw substrate-material which rigorously fills out all these requirements. Suitable substrate solutions can be met but most solutions are often home-made and are strongly based on materials optimization. In CIGS technology, the physical and chemical natures of the used substrates dictate CIGS processing steps. As an example, chemical decompositions and degasing of substrates are incompatible for vacuum based processing. Se or S atmosphere compatibility should be otherwise checked for the used substrate. To prevent Se attacks, an additional protection should be used to protect the back side of most metallic substrates. A release of some impurities into CIGS absorbing layer is not tolerable.

The CTE of substrate should match as well as possible those of the subsequent coatings. Figure 4 shows CTEs of several materials used for the fabrication of CIGS solar cells and gives prominence to their mismatch. Ideally, CTEs of materials must match each other. Due to the CTE incompatibility of materials usually used, differential dilatation occurs during the thermal treatments and consequently, exfoliation or delamination can be observed for some coatings. It

was shown in [39] that developments on soda lime glass (SLG) do not have this limitation because its CTE is around of 9 x 10^{-6} K^{-1} while that of CISG perpendicular to and along the c-axis are 11.4 x 10^{-6} and 7.9 – 8.6 x 10^{-6} K^{-1} respectively. Molybdenum back contact is always sandwiched between the substrate and CIGS active layers, thus it can often suffer from the mismatch between its CTE and those of the subsequent and the underlying layers.

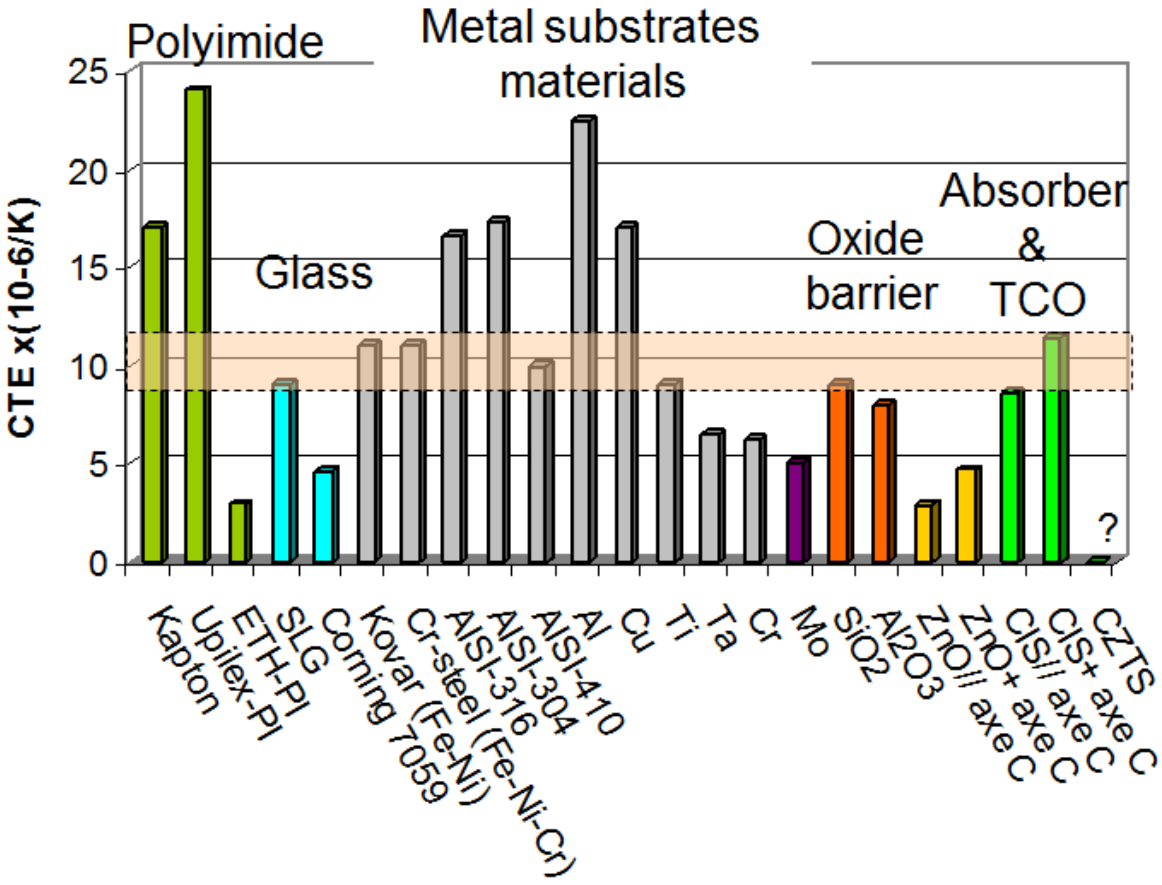

Figure 4: Histogram of CTE of materials tested in CIGS technology. Only materials used for emitter such as cadmium sulfide (CdS) and its derivate are not presented.

Bremaud et al. reported that Mo is often cracked if the CTE of the used substrate is too high [40] but they do not mention the critical or the appropriate value of CTE. In the following section, important results available in the public domain on plastic and metallic substrates will be presented.

I.3.1. Plastic substrates

Polyimides (PI) are a class of thermally stable polymers that are often used in flexible optoelectronic devices. The thermal stability of this kind of polymers is a consequence of their aromatic backbones [41]. The chemistry of polyimides is in itself a vast field and it includes a wide variety of available monomers and different synthetic methodologies.

In comparison with metallic substrates, PI substrates have the advantage of being electrically insulating and thus enabling direct monolithic interconnection (see insulating barrier layers section in I.4.2 for details). PI is also free of metallic impurities which could diffuse into the CIGS layer during processing and adversely affect the electronic properties of the absorbing layer. However, PI substrates are temperature sensitive and the maximum applicable temperature for PI is typically below 500°C. It is reported in [42,43] that this restriction has for a long time constrained the maximum demonstrated conversion efficiencies of CIGS solar cells on PI below 16 %. The fundamental issues of low-temperature grown CIGS which rigorously restrict the conversion efficiency to significantly lower values were unknown.

Efforts have been done recently to succeed in the fabrication of efficient CIGS solar cells on PI. Kapton developed by DuPont and Upilex from UBE industries have been tested by several authors [44,45,46,47]. Bollero et al. [48] tested the suitability of Upilex for the fabrication of CIGS cells by checking structural and thermal degradation of Mo/Upilex under argon and selenium atmospheres at 400°C. They deduced practical applications of these structures as back contact layers for CIGS solar cells on PI because their Mo films combined a low electrical resistivity of around of 30 μΩ·cm with a smooth surface free of cracks even after heating.

An efficiency of 14.1 % measured under simulated AM1.5 standard test conditions has been confirmed as conference record in 2005 for CIGS grown on Upilex films at a temperature lower than 500 °C by Rudman and co-workers [49]. Tentative works have been reported on the fabrication of CIGS solar cells on PET plastic substrates using ink. The maximum efficiency obtained by Faraj et al. on PET substrates is 4.12 % [50].

In 2011, Chirila et al. has developed a vacuum evaporation process for the growth of high quality CIGS absorber layers at a relatively low temperature around 450°C suitable for Upilex flexible substrates. By testing a modified growth recipe [51], they achieved a remarkable efficiency of 18.7 % on PI. The main advantage in this work is the relatively low-temperature deposition

method developed for the growth of CIGS absorbing layer [52]. In 2013, EMPA lab reported a record efficiency of 20.4% for thin film CIGS solar cell on a PI substrate [53].

I.3.2. Metallic substrates

To test suitability on metal pure substrates, some original works have been reported on fabrication of CIGS solar cells on uncoated selected metal substrates. Stainless steel (SS), titanium, Kovar (Fe/Ni/Co), mild steel, molybdenum or copper were tested by different research teams [54,35]. Ti has interesting physical properties such as low weight (4.51 g/ cm^3) and a CTE (8.4 x 10^6 K^{-1}) which matches well to that of CIGS absorbing layer; an efficiency of 17.4 % is reached on it [55]. Takeshi and Tokio also obtained in [56] an efficiency of 17.9 % for ZnS(O,OH)/CIGS based cells on Ti. The problem with Ti is the cost which is too high. Thus, Ti should be useful for specific space applications but not for the market dedicated to a general public. Aluminum foils failed due to their too high CTE but Yun and co-workers surprisingly reported on Al substrates an efficiency of 13.34 % [57]. As reported in [58], Cu substrate should be interesting thanks to the fact that it can be provided with very low surface roughness but is not a preferred flexible substrate because of its high CTE, diffusion rate and costs compared to other metals. Of all tested metallic substrates, steel substrates seem to be the most attractive substrate materials especially for terrestrial applications thanks to their cost advantage [59]. Contreras et al. reported in 1999 an efficiency of 17.4 % on pure stainless steel [60].

Nevertheless, efficiencies reported for CIGS solar cells on pure metallic substrates are often lower compared to performances of CIGS solar cells on SLG substrates [61,62]. Table 2 shows gaps in performances observed between cells performed on metals and those fabricated on glass substrates. The efficiency gap is particularly pronounced for the mild steel which has the highest content of Fe. The main reason for this gap is that metallic substrates such as steels may contain a great variety of atoms which can deteriorate or contaminate the CIGS absorbing layer [63]. Substrate atoms diffuse into the CIGS absorber during the thermal treatment step and the diffusion might be especially higher on rough substrates since it can be promoted at peaks of roughness.

Table 2: CTE and maximal surface roughness (Rz) of soda lime glass and current metal sheets with the best efficiency obtained for each family of substrate for a comparison. Cells are completed on metal substrates without any barrier layer.

	SLG	Ti	SS	Mild steel
CTE (ppm/K)	9	8,6	11-12	13
Rz (nm)	10 - 15	1900	680	500 - 2000
Efficiency (%)	20.3 [54]	17.9 [64]	17.7 [65]	12.8 [66]

To investigate effects caused by contaminant metallic atoms to CIGS absorber properly, the best procedure is probably to evaluate separately influences of the main atoms of the substrate. To check this, Jackson et al. [67] used a standard soda-lime-glass covered by a thin sputtered films of the different metallic atoms mainly present in the current metallic substrates. The standard CIGS solar cell as shown in the figure 5 has been then deposited at approximately 600°C and atomic concentration profiles have been obtained using secondary ions mass spectroscopy (SIMS). Thus, they found that Ni does not diffuse into the absorber in measurable concentrations but it has clearly a negative effect on performances of the solar cell.

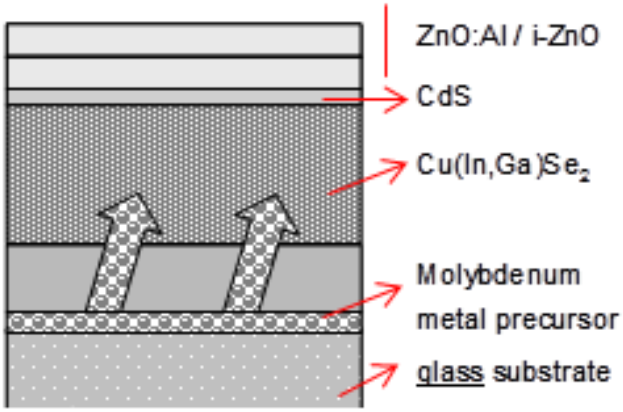

Figure 5: CIGS solar cell using glass substrate on which a metallic layer (called metal precursors) is deposited to test their effects on performances of the solar cell. The metal precursors can diffuse into CIGS through the molybdenum back-contact [67].

Low concentrations of Ti and Al have been detected. Extremely high concentrations of Mn and Fe are measured as shown in table 3. It has been observed that cells do not show photoelectrical signals any more when highly contaminated by Fe. It has been also observed that some elements with high concentrations in CIGS do not lead to a reduction of efficiency. As an example, the concentration of Cr in CIGS was especially high but negative impacts on the performance of cells were not observed at all. Finally, the most critical elements are Fe and Ni as both considerably reduce the solar cell efficiency even when they are present in the absorbing layer in very small concentration.

Table 3: Concentration of various atoms in the CIGS absorber correlated with the efficiency of the solar cell. The thickness of each tested metallic layer is around 100 nm while the thickness of the molybdenum films is approximately 0.6 µm [67].

Metal	Concentration in absorber	Efficiency evaluation
V	≈ 0 ppm	neutral
Ti	70 ppm	neutral
Cr	1750 ppm	neutral
Al	100 ppm	slight reduction
Ni	≈ 0 ppm	reduction
Mn	>10 at.%	destruction
Fe	10 at.%	destruction

Another problem met with metal substrates is the negative influence rising from their rough surface morphology. A smooth substrate surface is required since abrupt changes in the surface topography such as spikes or cavities may lead to shunts between the top and the bottom contacts. Especially, metal foils suffer from the rolling process currently used for foils production due to the fact that it leaves deep grooves, peaks and cavities on the surface. The maximum roughness of standard commercial steel sheets can be as high as 2 µm [62]; this can be detrimental in terms of shunt for CIGS solar cells since the distance between the top and the bottom electrodes is the same order of magnitude. Any surface inhomogeneity which can prevent the growth of a closed film can also cause pinholes between the front and the back contacts. Generally, a source of shunts results from particles which are stuck at the surface.

Otherwise, impurities diffused from the substrate into the CIGS during the high-temperature CIGS growth can be increased because of imperfect coverage of the substrate by the back contact. The amount of impurity diffusion occurring into the absorber could also be a function of the growth temperature and substrate composition [68].

In summary, steel substrates are definitely attractive for flexible CIGS technology especially when the high temperature deposition methods are used but, it is important to shield the absorbing layer from contamination by substrate atoms [69,70]. To solve this problem, metallic or non-metallic coatings can be interposed between the Mo back contact and the SS substrate to block the diffusion of unwanted elements [71]; this will be discussed in the following section.

I.4. Steel substrates and barrier layers

Additional layers interposed between the substrate and the Mo back contact to block the diffusion of contaminants as previously exposed are called diffusion barrier layers (DBLs). Normally, a 2 µm-thick Mo film should be sufficient to reduce the diffusion of the main undesired atoms but the use of thick Mo films is limited due to the high cost and the long deposition time. Alternative DBLs using metallic and non-metallic layers have been developed.

I.4.1. Metallic barrier layers

Various metallic DBLs have been tested for CIGS solar cells and detail can be found in [72,40]. As reported in these references, metal coatings with neutral effect on CIGS absorber have to be used in order to avoid contamination. Consequently, Cr, Ti and their nitrides are widely used. Thin Cr layers are tested in [73,74]. Khelifi et al. compared cells efficiency on different metallic sheets coated with Mo/Cr, Mo/CrN and CrN [71]. They found that a decrease of efficiencies is caused by the presence of defects which decrease open-circuit voltages of solar cells. Their best cells were found with CIGS layer grown on the stainless steel substrate coated with a 100 nm-thick Cr barriers layer combined with 1 µm-thick Mo back-contact; the maximum efficiency exceeding 13 % has been reached. L. Guo et al. [75] have demonstrated that a 300 nm-thick layer of nickel phosphorus can be an effective DBL.

I.4.2. Insulating barrier layers

Insulating coatings can be also used to block the diffusion of undesired atoms into CIGS layer. In addition to their diffusion barrier properties, insulating materials also allow the fabrication of monolithically integrated modules onto metallic substrates where different cells should be electrically isolated from each other and directly interconnected during their deposition. Monolithic interconnection of CIGS solar cells integrated on PI and insulated metallic substrates such as steels is shown in figure 6. It can be clearly seen that insulating DBL is essential on metallic substrate.

The thickness required for insulating DBL to ensure a good electrical insulation is usually higher than the one needed for suppression of diffusion. Thus, good insulating DBLs are usually sufficiently thick to block the diffusion of metallic substrate atoms. On the other hand, barrier layers should survive high temperatures in Se atmosphere without cracks formation and withstand all patterning steps without losing their insulating properties. SiO_2 and Al_2O_3 coatings, high thermal polymer coatings or polymer-derived ceramics (PDCs) can play the role of insulating BDLs and will be presented in the following sections.

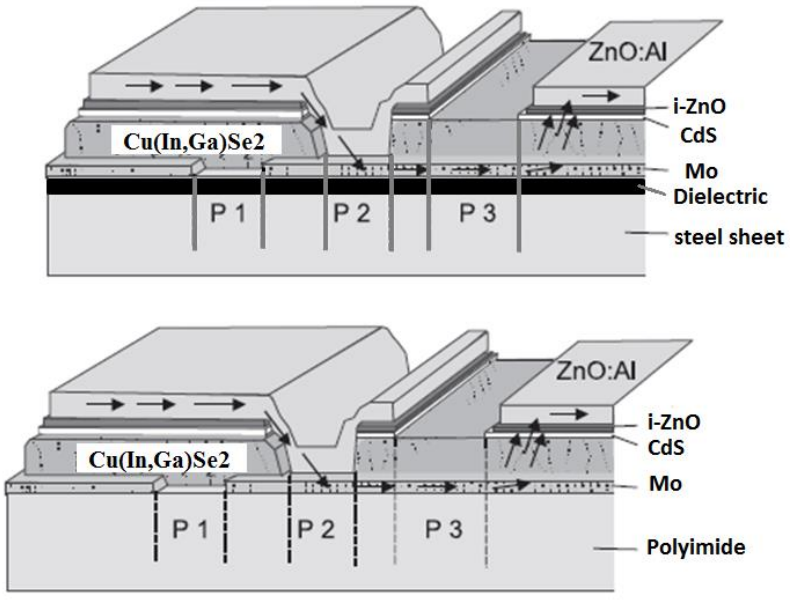

Figure 6: Illustration of monolithic cells integration on steel sheets (top) and polyimide (bottom) for comparison. Modified from [35].

I.4.2.1. SiO_2 and Al_2O_3 coatings

SiO_2 and Al_2O_3 dielectric layers prepared by either vacuum processing such as PECVD deposition technique or sol–gel methods are tested [71,76]. Technologically, sol–gel coatings are compatible with a rolling process and permit Na doping. PECVD process is a scalable and fast technique and SiO_2 coatings widely used for a role of insulating DBL in CIGS solar cells are often prepared by this technique using an appropriate mixture of hexamethyldisiloxane (HMDSO) and O_2 as precursors [77].

Insulating layers of SiO_2 and Al_2O_3 prepared by both PECVD and sol-gel deposition methods were tested at Zentrum für Sonnenenergie und Wasserstoff (ZSW) by using 3 to 10 μm-thick, with encouraging results [78]. Unfortunately, pinholes are often observed in such coatings; they result from the formation and the precipitation of particles during the growth. Pinholes generation in thin films can considerably reduce the dielectric strength. It was reported in [79] that particles can be prevented in any case by using an appropriate method for cleaning of the substrate and of the deposition chamber. The compactness of oxide coatings was tested on commercially available unpolished Cr–steel, Ti, and Kovar substrates by measuring the resistivity before and after the CIGS process and by the application of a galvanic method which detects pinholes quantitatively via the generation of bubbles [79].

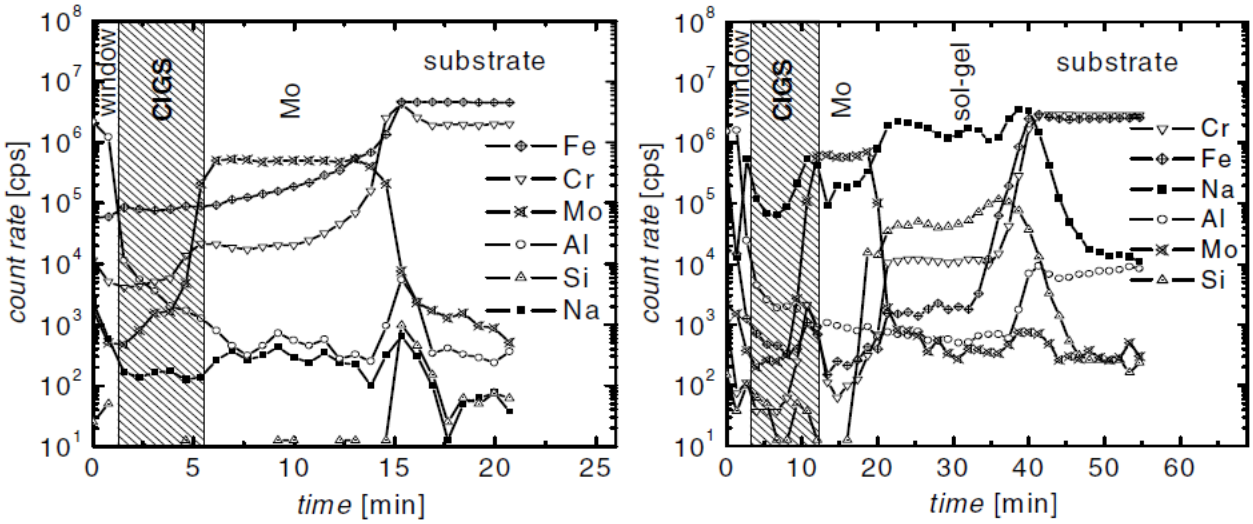

Figure 7: Secondary ion mass spectroscopy (SIMS) depth profiles of CIGS solar cells on stainless steel foil without barrier layer (left) and with sodium containing SiO_x:Na (sol/gel) layer (right) [79].

To check the suitability of SiO_x layers prepared using the sol-gel process, authors of [79] carried out SIMS profiles for CIGS solar cells prepared on uncoated Kovar substrate and Kovar substrate coated with SiO_x. It was found that sol-gel can significantly reduce the amount of contaminants in CIGS films as shown in figure 7. As summarized in table 4, the application of a sodium-containing sol-gel layer leads to a considerable increase in efficiency (from 3.1 to 10.2 %) probably due to:

- sufficient sodium-supply into the CIGS absorber;
- the reduction of out-diffusion of substrate atoms.

Table 4: Performances of CIGS solar cells on Kovar with and without diffusion barrier layer compared to reference cells performed on SLG substrates [73].

Substrate	Efficiency (%)
SLG	14.7
Uncoated Kovar	3.1
Sol-gel (SiOx:Na)/Kovar	10.2
PECVD (SiOx)/Sol-gel/Kovar	13.1

Thick insulating DBLs are good electrical insulators, but often suffer from extreme surface roughness, cracks and reduced flexibility as can be observed in figure 8. These disadvantages could be overcome by using thin barrier layers with thickness less than 10 µm. Herz et al. [76] investigated the electrical characteristics of Al_2O_3 films of 1 to 6 µm-thick on Kovar, Cr-steel and titanium. They found that the electrical insulation is worse for 1 to 2 µm-thick Al_2O_3 coatings on all tested substrates.

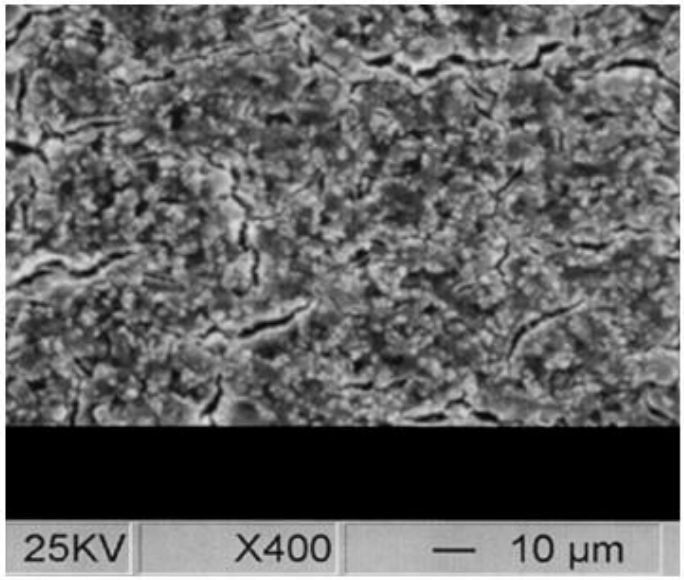

Figure 8: High temperature varnish on Ti. [83].

Their coatings of 3 to 6 µm-thick Al_2O_3 seem to yield good insulation on Ti [80]. It was also found in [81] that 3 µm-thick Al_2O_3 can significantly reduce the diffusion. Based on statistical analysis of the correlation of efficiency and barrier thickness using SIMS analysis, the authors of [81] recommended Al_2O_3 films of 2 µm-thick on Cr-steel and 1 µm-thick on Kovar substrates for impurities diffusion blocking.

Wuerz and co-workers tested on a steel sheet a stack of four layers of SiO_x deposited by PECVD and an alternative Na modified silicate prepared by sol-gel [66]. In their study, SiO_x is in some cases coupled with Ti thin films which promote adhesion and reduce diffusion of undesired atoms. The maximum cell efficiency achieved on uncoated steel and steel coated with a sol–gel barrier are respectively 6 % and 10.6 % while the value of 11.6 % is reached on SLG reference substrate. By combining a plasma SiO_x layer, a sol-gel coating and the Ti thin layer, they could achieve an efficiency of 12.8 %. They assigned the enhancing in the solar cell performances to the reduction of the amount of metallic contaminants in the CIGS layer.

I.4.2.2. Polymer coatings

Recent developments are exploring diffusion barrier layer based on organic polymer wet coatings based diffusion barrier layers. Resin like polyimide films meet the criteria for the dielectric aspects, but have the restriction of lower maximum substrate temperatures because of

their low thermal stability. It can be clearly seen in table 5 that the current temperature resistant organic polymers exhibit stability lower than the minimum temperature (450°C) required for the growth of CIGS layer using standard growth methods. Note however that alternative deposition methods are being developed for lower the growth of CIGS at lower temperature and details can be found in [31,82,83].

Table 5: High thermal polymers commercially available.

Polymer	Thermal stability
Elastomer silicate	260°C – 300°C
Epoxy	275°C – 350°C
Polyimide	300°C – 400°C

I.4.2.3. Polymer-derived ceramics (PDCs)

Silicon-based advanced ceramics or polymer-derived ceramic (PDCs) are high temperature (up to 2000°C) resistant dielectric ceramics [84] and are commonly synthetized by the pyrolysis of organosilicon polymers. PDCs are currently used in ceramic technology but the high thermal dielectric aspects of these materials can be explored for CIGS applications. Thus, different types of PDCs are presented with an especial emphasis made on polysilazanes retained as a base for all DBL systems used in this thesis.

PDCs are mainly prepared using inorganic or organometallic polymer precursors which have to be converted into ceramic coatings [85]. Several kinds of PDCs exist, a detailed description of which is found in [86]:

- the binary systems (Si-N, Si-C, B-N, Al-N, etc.) ;
- the ternary systems (Si-C-N, Si-C-O, B-C-N, etc.) ;
- and the quaternary systems (Si-C-N-O, Si-B-C-N, Si-B-C-O, Si-Al-C-N, etc.).

PDCs are remarkably temperature resistant and exhibit an excellent resistance to oxidation [87]. As an example, silicon carbonitride (Si-C-N) ceramics were found to resist to temperatures from 1000°C to 1500°C [88,89]. Riedel et al. [90] reported that when boron atoms are added to silicon

carbonitride ternary materials, the resulting Si-B-C-N quaternary materials exhibit remarkable thermal, chemical, and mechanical stability higher than that of Si-C-N even at extremely high temperatures (> 2000°C). They attributed this to structural disorder in Si-B-C-N systems which results in increased free activation energies of both crystallization and the solid-state reactions of Si–N bonds with carbon atoms.

- ***Deposition methods for PDCs***

PDCs are usually prepared using conventional polymer-forming techniques such as polymer infiltration pyrolysis, injection molding, extrusion, coatings from solvent and resin transfer molding as reported in [84]. In the case of development of PDCs layers as is required for our application, other deposition methods should be used for the generation of coatings. The well-known techniques for coatings depositions are thermal spraying, plasma enhanced chemical vapor deposition (PECVD), physical vapor deposition (PVD), or sol–gel processes [91,92]. Generally, plasma and high vacuum based techniques are complex and expensive. It was also demonstrated that the generated ceramic coatings through these technologies are often highly micro-porous [90]. Wet coatings are easier to implement but the resulting coatings can be highly nano-porous [93,94]. However, processes involved in wet coating preparations are often inexpensive and are straightforward compared to vacuum based techniques such as chemical vapor deposition (CVD) or PVD methods. Moreover, the wet coatings technique such as sol-gel processes has a great potential for the industrial rolling process. For these reasons, special emphasis should be given to wet coating processes for elaboration of our DBLs.

- ***Molecular structure of PDCs materials***

The general formula of silicon based polymers commonly used as precursor for PDCs materials is shown in figure 9. Two important components can be identified at the molecular level and are commonly used to modify the structural properties of the resulting PDC. The first component is the group (X) and the second one consists of substituents (R1) and (R2) attached to Si atoms. It was reported in [88] that the class of Si based PDCs depends on the nature of X which can be Si, NH, CH_2 or O, etc. while the nature of groups (R1) and (R2) at the silicon atoms defines the chemical and thermal stability of these hybrid polymers. Groups (R) are mostly hydrogen, aliphatic or aromatic groups. Electronic, optical and rheological properties of these polymers can be modified or adjusted by adapting the chemical nature of groups (R) [95].

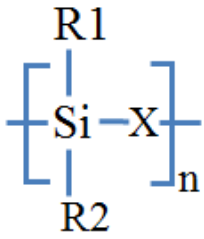

Figure 9: Simplified illustration of the molecular structure of silicon based PDCs.

A non-exhaustive list of reference families of Si-based PDCs commonly used in ceramic technology is provided in table 6 with some important specifications. Several variants exist for each class and details on these PDCs are described already in [84]. It was reported in [80] that at temperatures lower than 600°C most non-metallic dopant PDC bulks can be normally considered as insulators with average dc conduction lower than 10^{10} $\Omega.cm^{-1}$; the dielectric character depends of course on the polymeric precursors, chemical composition, and pyrolysis temperature and/or atmosphere.

Table 6: Current silicon-based polymer-derived ceramics.

Class of PDC	Groups (X)	Some important specifications
Poly(organosilanes)	Si-Si	Exhibit photo-conductive, luminescence or semiconductor functions [96], properties originated from σ conjugation [97].
Poly(organocarbosilane)	Si-C-Si	Applications in SiC based fibers area. Most of them are synthesized from poly(methylcarbosilane), they have a great interest because of their high ceramic conversion yield [84].
Poly(organosilazanes)	Si-NH-Si	Can be used as single-source precursors for ceramic materials using vapor, liquid or solid phase pyrolysis [98].

- ***Polysilazanes (PSZs)***

PSZs are a family of PDCs where silicon and nitrogen atoms are alternated as shown in figure 10. Compared to the general formula of PDCs, groups (R1) and (R2) are attached to silicon atoms and are usually hydrogen atoms or any other organic substituents. When all groups (R) are represented by H atoms, the polymer is inorganic and is called polyperhydridosilazane (PHPS) with general formula given by $[H_2Si–NH]_n$.

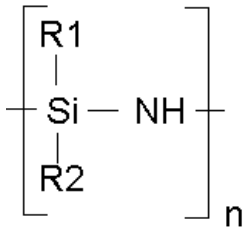

R1 and R2 can be hydrogen or organic substituents

Figure 10: The chemical formula of polysilazane: polymer in which silicon and nitrogen atoms alternate to form the basic backbone.

In the structure where organic substituents like hydrocarbons are bound to silicon atom or nitrogen, PSZs are called organopolysilazanes (OPSZ) and are close to the well-known polysiloxane $[R1\text{-}R2Si–O]_n$ [99]. Polysilzanes are widely used in industry for protection and conservation functions like easy-to-clean, anti-graffiti, corrosion inhibition and high temperature performances and they cover several markets such as automotive (truck pipe and car body protection), railway transportation (anti-graffiti protection), marine (protection of boats), architecture (aluminum window profiles) and microelectronics.

One of the main problems for their use as DBL for CIGS solar cells is that they often show significant mass loss during thermal treatments. By using thermogravimetric analysis (TGA), Günthner et al [87] reported for pure PHPS and ammonolysed bis(dichlormethyl)silylethane (ABSE) mass changes of 15 wt.% and 12 % respectively at 550-600°C in nitrogen. Gardelle et al. [100] tested vinyl polysilazane (VPSP) and demonstrated an excellent thermal resistance to mass loss for this material. Aluminum trihydroxide was added to their VPSP to enhance the fire performance of the coating and has otherwise beneficial effects on the weight loss (7 wt. % at 400 - 550°C).

For dielectric aspects, J.H. Wang and co-workers [101] reported that PHPS coatings are ultra-low constant dielectric material (*k* is around of 2.2).

I.5. Summary

In this chapter, we reviewed progress made on flexible substrates for the fabrication of CIGS-based solar cells. It was shown that polymer or metal substrates can be used for the fabrication of this type of solar cells. However, the high temperature treatment step required for current CIGS growth methods limits the choice of suitable substrates. Thus, thermal properties such a high thermal stability and CTE constitute the key parameters to check for all layers under the CIGS absorber.

Among the tested substrates, steel sheets have been revealed more attractive. Steels contain however detrimental atoms for CIGS absorber; the use of this type of substrates requires an additional layer called DBL to block the diffusion of impurities. For the interconnection of monolithically integrated cells on metallic substrates, insulating DBLs are required. Achieving good quality electrical insulation is especially difficult due to the high temperature treatment step required for the fabrication of CIGS devices.

To our knowledge, the best barrier layer in the literature is obtained by K. Herz et al. with 6 µm-thick of combi-layers SiO_x (SiO_x (double sol-gel layers + stirring at 500°C)/three SiO_x layers (PECVD) or Al_2O_3 (sputtered)/ three SiO_x layers (PECVD)). The combi-layer yields a good electrical insulation on Ti substrates since a breakdown voltage of 300 V can be reached on non-annealed coatings but is worse on stainless steel [77]. The fact that a cleaning step is required between each layer makes the process especially complex. Ceramics are good dielectrics but their limitations rise mainly from the reduced flexibility. Thin ceramics can tolerate some conformability but are porous therefore suffer from electrical isolation. These results revealed that the electrical insulation suitability for DBLs and the thermal stability of the whole systems are particularly hard to reach and are still a challenge. Hybrid polymers (a mixture of polymer and inorganic compounds) such as polysilazanes have good dielectric properties and thermal stability. Polysilzanes are widely used in industry for protection and conservation functions like easy-to-clean, anti-graffiti, corrosion inhibition and high temperature performances. To our

knowledge, polysilazanes have never been used in the fabrication of CIGS solar cells. Based on its properties potentially excellent for flexible CIGS technology, we explored a sort of commercial polysilazane in this thesis to act as insulating DBL for CIGS solar cells.

References

[1] M.A. Contreras, K. Ramanathan, J. AbuShama, F. Hasoon, D.L. Young, B. Egaas, R. Noufi, Prog. Photovolt Res. Appl. 13 (2005) 209.

[2] S.H. Mousavi, T.S. Müller, P.W. de Oliveira, Journal of Colloid and Interface Science 382 (2012) 48/52.

[3] J. López-García, C. Guillén, Thin Film Solids 517 (2009) 2240/2243.

[4] Y.B.K. Reddy, V.S. Raja, B. Sreedhar, J. Phys. D: Appl. Phys. 39-24 (2006) 5124.

[5] B. Munir, R.A. Wibowo, E.S. Lee, K.H. Kim, J. Ceram Process. Res. 8-4 (2007) 252.

[6] B.M. Basol, V.K. Kapur, A.H. Halani, C.R. Leidholm, J. Sharp, J.R. Sites, A. Swarzlander, R. Matson, H. Ulla, J. Vac. Sci. Technol. A 14 (1996) 2251/2256.

[7] O. Lundberg, J. Lu, A. Rockett, M. Edoff, L. Stolt, Journal of Physics and Chemistry of Solids 64 (2003) 1499/1504.

[8] A. Pudov, Ph.D. thesis, Colorado State University (2005).

[9] D. Rudmann, Ph.D. thesis, Swiss Federal Institute of Technology (ETH), Zürich (2004).

[10] N. E. Gorji, U. Reggiani, L. Sandrolini, Solar Energy 86 (2012) 920/925.

[11] M. Gloeckler, J.R. Sites, Thin Solid Films 480-481 (2005) 241/245.

[12] B. J. Stanbery, Reviews in Solid State and Materials Sciences, 27-2 (2002) 73/117.

[13] J.S. Park, Z. Dong, Sungtae Kim, J.H. Perepezkoa, J. Appl. Phys. 87-8 (2000) 3683/3690.

[14] W.K. Kim, E.A. Payzant, S. Yoon, T.J. Anderson, Journal of Crystal Growth 294 (2006) 231/235.

[15] E.R. Baek, Vita Astini, Andy Tirta, Bora Kim, Current Applied Physics 11 (2011) S76/S80.

[16] O. Savadogo, Sol. Energy Mater. Sol. Cells 52 (1998) 361/388.

[17] S. J. Park, E. Lee, H. S. Jeon, S. J. Ahn, M-K. Oh, B. K. Min, Applied Surface Science 258 (2011) 120/125.

[18] M. Venkatachalam, M.D. Kannan, N. Muthukumarasamy, S. Prasanna, S. Jayakumar, R. Balasundaraprabhu, M. Saroja, Sol. Energy 83 (2009) 1652/1655.

[19] P. Jackson, R. Wurz, U. Rau, J. Mattheis, M. Kurth, T. Schlotzer, G. Bilger, J.H. Werner, Prog. Photovoltaics Res. Appl. 15 (2007) 507/519.

[20] I. Repins, M.A. Contreras, B. Egaas, C. DeHart, J. Scharf, C.L. Perkins, B. To, R. Noufi, Prog. Photovoltaics Res. Appl. 16 (2008) 235/239.

[21] B. Dimmler, R. Wachter, Thin Solid Films 515 (2007) 5973.

[22] http://www.miasole.com/sites/default/files/MiaSole_release_Dec_02_2010.pdf.

[23] M. Kaelin, D. Rudmann, A.N. Tiwari, Sol. Energy 77 (2004) 749/756.

[24] Y. Chiba, S. Kijima, H. Sugimoto, Y. Kawaguchi, M. Nagahashi, T. Morimoto, T. Yagioka, T. Miyano, T. Aramoto, 35th IEEE Photovoltaic Specialists Conference, 2010, p. 164.

[25] Z. Yu, Y. Yan, S. Li, Y. Zhang, C. Yan, L. Liu, Y. Zhang, Y. Zhao, Appl. Surf. Sci. 264 (2013) 197.

[26] V. S. Saji, I-H. Choi, C-W. Lee, Solar Energy 85 (2011) 2666/2678.

[27] C. P. Liu, C. L. Chuang, Powder Technology 229 (2012) 78/83.

[28] S.H. Mousavi, T.S. Müller, P.W. de Oliveira, Journal of Colloid and Interface Science 382 (2012) 48/52.

[29] Q. Guo, G.M. Ford, H.W. Hillhouse, R. Agrawal, Proceedings 37th IEEE PVSC Conference, 2011 Seattle.

[30] N. Benslim, S. Mehedaoui, O. Aissaoui, M. Benabdeslem, A. Bouasla, L. Bechiri, A. Otmani, X. Portier, Journal of Alloys and Compounds 489 (2010) 437/440.

[31] C-C. Chen , X. Qi, M-G. Tsai, Y-F. Wu, I-G. Chen, C-Y. Lin, P-H. Wu, K-P. Chang, Surface & Coatings Technology (2012).

[32] R. Caballero, C.A. Kaufmann, T. Eisenbarth, M. Cancela, R. Hesse, T. Unold, A. Eicke, R. Klenk, H.W. Schock R. Caballero, C.A. Kaufmann, T. Eisenbarth, M. Cancela, R. Hesse, T. Unold, A. Eicke, Thin Solid Films 517 (2009) 2187/2190.

[33] http://glassproperties.com.

[34] S. A. Pethe, V. Hadagali, N G. Dhere, Proceeding of SPIE Vol. 7409 (2009) 740911.

[35] F. Kessler, D. Herrmann, M. Powalla, Thin Solid Films 480–481 (2005) 491/498.

[36] D. Amouzou, P. Guaino, J. Dumont, L. Fourdrinier, J.B. Richir, R. Sporken, F. Masen, in: Proceedings of the 26th PVSC, 2011.

[37] P. Blosch, A. Chirila, F. Ianezzi, S. Seyrling, P. Rossbach, S. Buecheler, S. Nishiwaki, A.N. Tiwari, in: Proceedings of the 26th PVSC, 2011.

[38] A.N. Tiwari, M. Krejci, F.J. Haug, H. Zogg, Progress in Photovoltaics: Research and Applications 7 (1999) 393/397.

[39] F. Kessler, D. Rudmann, Solar Energy 77 (2004) 685.

[40] D. J. L. Bremaud, Ph.D thesis, University of Zurich (2009).

[41] D-J. Liawa, K-L. Wang, Y-C. Huang, K-R. Lee, J-Y Lai, C-S Ha, Progress in Polymer Science 37 (2012) 907/ 974.

[42] Nakada, T. Proc. 24th Eur. PV Solar Energy Conf. (EUPVSEC),WIP_Renewable Energies (2010).

[43] P. Jackson, M. Powalla, E. Lotter, D. Hariskos, S. Paetel , R. Wuerz,R. Menner, W. Wischmann, Progress in Photovoltaics: Research and Applications 19 (2011) 894/897.

[44] H. Zachmann, S. Heinker, A. Braun, A.V. Mudryi, V.F. Gremenok, A.V. Ivaniukovich, M.V. Yakushev, Thin Solid Films 517 (2009) 2209.

[45] S. Ishizuka, H. Hommoto, N. Kido, K. Hashimoto, A. Yamada, S. Niki, Appl. Phys. Express 1 (2008) 10.

[46] C-C. Chen, X. Qi, M-G. Tsai, Y-F. Wu, I-G. Chen, C-Y. Lin, P-H. Wu, K.-P. Chang, Surf. & Coat. Techno. (2012) .

[47] H. Zachmann, S. Puttnins, M.V. Yakushev, F. Luckert, R.W. Martin, A.V. Karotki, V.F. Gremenok, A.V. Mudryi, Thin Solid Films 519 (2011) 7264/7267.

[48] A. Bollero, L. Kaupmees, T. Raadik, M. Grossberg, S. Fernández, Thin Solid Films 520 (2012) 4163/4168.

[49] D. Bremaud, D. Rudmann, G. Billger, H. Zogg, A.N. Tiwari, in: Proceedings of the 31th IEEE Photovoltaic Specialists Conference, Orlando, 2005, pp. 223/226.

[50] M.G. Faraj, K.Ibrahim, A.Salhin, Materials Science in Semiconductor Processing 15 (2012) 165/173.

[51] A. Chiril, Proc. 35th IEEE Phot. Spec. Conf. (PVSC) 656-660 (IEEE, 2010).

[52] A. Chiril, S. Buecheler, F. Pianezzi, P. Bloesch, C. Gretener, A.R.Uhl, C.Fella, L. Kranz, J. Perrenoud, S. Seyrling, R. Verma, S. Nishiwaki, Y. E. Romanyuk, G. Bilger, A. N. Tiwari, Nature Materials 10 (2011) 857–861.

[53] http://www.sciencedaily.com/releases/2013/01/130118064733.htm.

[54] M. A. Green, K. Emery, Y. Hishikawa, W. Warta, E. D. Dunlop, Prog. Photovolt, Res. Appl. 20 (2012) 606/614.

[55] S. Ishizuka, A. Yamada, K. Matsubara, P. Fons, K. Sakurai, S. Niki, Applied Physics Letters 93 (2008) 124105-1/124105-3.

[56] T. Yagioka, T. Nakada, Applied Physics Express 072201- 12 (2009) 072201/3.

[57] J. H. Yun, K. H. Kim, M. S. Kim, B. T. Ahn, S. J. Ahn, J. C. Lee, K. H. Yoon, Thin Solid Films 515 (2007) 5876/5879.

[58] O. Tober, J. Wienke, M. Winkler, J. Penndorf, J. Griesche, Mater. Res. Soc. Symp. Proc. 763 (2003) 371.

[59] R. Wuerz, A. Eicke, M. Frankenfeld, F. Kessler, M. Powalla, P. Rogin, O. Yazdani-Assl, Thin Solid Films 517 (2009) 2415/2418.

[60] M. A. Contreras, B. Egaas, K. Ramanathan, J. Hiltner, A. Swartzlander, F. Hasoon, R. Noufi, Prog. Photovolt: Res. Appl. 7 (1999) 311/316.

[61] K. Herz, A. Eicke, F. Kessler, R. Wa chter, M. Powalla, Thin Solid Films 431-432 (2003) 392/397.

[62] R. Wuerz, A. Eicke, F. Kessler, S. Paetel, S. Efimenko, C. Schlegel, Solar Energy Materials and Solar Cells, 100 (2012) 132/137.

[63] C.Y. Shi, Yun Sun, Qing He, F.Y. Li, J.C. Zhao, Solar Energy Materials & Solar Cells 93 (2009) 654/656.

[64] T. Nakada, T. Yagioka, K. Horiguchi, T. Kuraishi, T. Mise, Proceedings of the 24th European Photovoltaic Solar Energy Conference, 21–25 September 2009, Hamburg, Germany; pp. 2425/2428.

[65] F. Pianezzi, A. Chirila, P. B osch, S. Seyrling, S. Buecheler, L. Kranz, C. Fella, A. N. Tiwari, Progress in Photovoltaics: Research and Applications (2012),doi:10.1002/pip.1247.

[66] R.Wuerz, A. Eicke, M. Frankenfeld, F. Kessler, M. Powalla, P. Rogin, O. Yazdani-Assl, Thin Solid Films 517 (2009) 2415/2418.

[67] P. Jackson, P.O. Grabitz, A. Strohm, G. Bilger, H.W. Schock, unpublished from P. Jackson, contacted: Philip.Jackson@ipe.uni-stuttgart.de.

[68] W.K. Batchelora, I.L. Repins, J. Schaefer, M.E. Beck, Solar Energy Materials & Solar Cells 83 (2004) 67/80.

[69] Sh. Obeidi, R. Würz, M. Frankenfeld, A. Eicke, N.A. Stolwijk , Sh. Obeidi, R. Würz, M. Frankenfeld, A. Eicke, N.A. Stolwijk, Thin Films Solid 517 (2009) 2205/2208.

[70] P. Jackson, P. Grabitz, A. Strohm, G. Bilger, H.W. Schock, Proceedings of the 19th European Photovoltaic Solar Energy Conference, 7–11 June 2004, Paris, France; pp. 1936/1938.

[71] S. Khelifia, A. Belghachi, J. Lauwaerta, K. Decock, J. Wienke, R. Caballero, C. A. Kaufmann , M. Burgelman, Energy Procedia 2 (2010) 109/117.

[72] F. Kessler, K. Herz, M. Powalla, M. Hartmann, M. Schmidt, A. Jasenek, H.W. Schock , Mater. Res. Soc. Symp. Proc., 668 (2001), p. H3.6.1.

[73] W. K. Batchelor, M. E. Beck, R. Huntington, I. L. Repins, A. Rocket, W. N. Shafarman, F. S. Hasoon, and J. S. Britt, Proceedings of the 29th IEEE Photovoltaics Specialist's Conference, New Orleans, LA (2002) 716.

[74] J. R. Tuttle, A. Szalaj, J. Keane, 28th IEEE Photovoltaic Specialists Conference, Anchorage, AK (2000) 1042..

[75] L. Guo, M. Mason, M. Hopstaken, A. Kellock, L. T. Romankiw, H. Deligianni, Journal of The Electrochemical Society, 160 (2013) 3, D102-D106.

[76] K.Herz, F.Kessler, R.Wächter , M.Powalla , J.Schneider , A.Schulz , U.Schumacher, Thin Solid Films 403/404 (2002) 384/389.

[77] W. Petasch, E. Räuchle, H. Muegge, K. Muegge, Surf. Coat. Technol. 93 (1997) 112.

[78] F. Kessler, D. Herrmann, M. Powalla, Thin Solid Films 480–481 (2005) 491/ 498.

[79] D. Herrmann, F. Kessler, K. Herz, M. Powalla, A. Schulz, J. Schneider, U. Schumacher, Mat. Res. Soc. Symp. Proc. 763 (2003) B.6101/ B.6106.

[80] R.Wächter, F. Kessler, K. Herz, M. Powalla, Proceedings 10 Bundesdeutsche Fachtagung Plasma technology (2001) p. 39.

[81] G.S. Vicente, J. Herrero, A. Morales, C. Mafiotte, M.T. Gutierrez, M. Hartmann, A. Jasenek, H.W. Schock, Proceedings of the 17th Eur. Phot. Sol. Conf., Munich, 2001, p. 1098.

[82] A. Tverjanovich, E.N. Borisov, E.S. Vasilieva, O.V. Tolochko, I.E. Vahhi, S. Bereznev, Yu.S. Tveryanovich, Sol. Energy Mater. Sol. Cells 90 (2006).

[83] R. Teghil, L. Dalessio, A. Debonis, D. Ferro, A. Galasso, G. Lanza, A. Santagata, P. Villani, D. Sordelet, Thin Solid Films 517 (2009) 1880.

[84] P. Colombo, G. Mera, R. Riedel, G. D. Sorarù, J. Am. Ceram. Soc., 93 (2010) 1805/1837.

[85] S. Bernard, K. Fiaty, D. Cornu, P. Miele, P. Laurent, J. Phys. Chem. B, 110-18 (2006) 9048/60.

[86] P. Hoffmann, N. Fainer, M. Kosinova, O. Baake1 and W. Ensinger, www.intechopen.com.

[87] M. Günthner, T. Kraus, A. Dierdorf, D. Decker, W. Krenkel, G. Motz, Journal of European Cermaic Society, 29 (2009) 2061/2068.

[88] R. Riedel, G.Mera, R. Hauser, A. Klonczynski, J. Ceram. Soc., 114 (2006) 425/44.

[89] Z-C. Wang, F. Aldinger, R. Riedel, J. Am. Ceram. Soc., 84 (2001) 2179/83.

[90] R. Riedel, G. Mera, R. Hauser, A. Klonczynski, J. Ceram. Soc. Jpn., 114 (2006) 425/44.

[91] D. Allebrandt, H. Hoche, H. Scheerer, E. Broszeit, C. Berger, Surf. Coat. Technol. 201 (2007) 5172/5175.

[92] J.D. Torrey, R. K. Bordia, Jr. C. H. Henager, Y. Blum, Y. Shin, W. D. Samuels, J. Mater. Sci., 41 (2006) 4617/4622.

[93] C. Vakifahmetoglu, I. Menapace, A. Hirsch, L. Biasetto, R. Hauser, R. Riedel, P. Colombo, Ceramics International 35 (2009) 3281/3290.

[94]Y.-W. Kim, C. B. Park, Comp. Sci. Tech., 63 (2003) 2371/7.

[95] R. D. Miller, J.Michl, Chem. Rev. 89 (1989) 1359/410.

[96] R. West, J. Organomet. Chem., 300 (1986) 327/46.

[97] R. Crespo, M. C. Piqueras, F. Tomas, Proc. of ICSM, International Conference on Science and Technology of Synthetic Metals, pp.238/238, 24-29 July 1994.

[98] E. Kroke, Y-L. Li, C. Konetschny, E. Lecomte, C. Fasel, R. Riedel, Mater. Sci. Eng., 26 (200) 97/199.

[99] L. L. Hench, Technology Transfer, Noyes Publications (1998).

[100] B. Gardelle, S. Duquesne, C. Vu, S. Bourbigot, Thermochimica Acta 519 (2011) 28/37.

[101] J.H. Wang, P.T. Liu, T.S. Chang, T.C. Chang, L.J. Chen, Thin Solid Films 469–470 (2004) 393/ 397.

CHAPTER 2
Polysilazane Based Barrier Layers

II.1. Introduction

Major concerns for the monolithic integration of CIGS solar cells on metallic substrates such as steel sheets have been reported in chapter I. It was clearly exposed that the main challenge is to prepare the appropriate insulating DBLs which have to play the roles of diffusion barrier and electrical insulation [1,2,3] and to withstand thermal effects.

In this chapter, we investigate the capability of polysilazanes (PSZs) based coatings prepared on stainless steel sheets [4] to act as insulating DBL for CIGS solar cells. Results are organized into three important parts.

The first part discusses thermal analysis of PSZs coatings where thermal stability and influence of temperature on structural properties such as the surface morphology, roughness or crystallinity are investigated.

The second part deals with dielectric properties of stacks made with polysilazane coatings and SiO_xAl_y. Different stacks are tested and the effects of annealing on electrical properties are studied. Metal-Insulating-Metal, MIMs, capacitors are fabricated with these stacks. MIMs are characterized using constant voltage stress (CVS) measurements for investigations in DC mode. Thus, the leakage current, the dielectric strengths and the dielectric reliability are studied. Ramped voltage stress methods [5] are used for data recording and experimental data are processed in order to determine the conduction mechanism in the solid dielectrics. Conduction mechanisms follow analytical laws which allow the determination of key parameters for dielectric materials testing. AC mode analysis is also used to evaluate the dielectric behavior of some coatings especially because this method allows to access information from different regions in the dielectric slab. With this method, the electrical signals obtained experimentally are

modeled using simple electric elements such as pure resistance (R) and capacitance (C). Evaluations in AC mode also help for further understanding of frequency-dependent response of our dielectric to the electric field.

In the third part, the ability of our coatings to act against the diffusion of undesired Fe and Ni atoms from stainless steel substrates is investigated using time-of-flight secondary ion mass spectroscopy (ToF-SIMS) [6] and the glow discharge optical emission spectroscopy (GDOES).

II.2. Samples preparation

II.2.1. The used polysilazane

The polysilazane we used is an organic polysilazane developed by AZ Electronic Materials Company. It is a clear, colorless and low viscosity liquid resin. To give an idea of its molecular structure, the product is a derivative of a commercially available KiON HTA 1500 Slow Cure shown in figure 1.

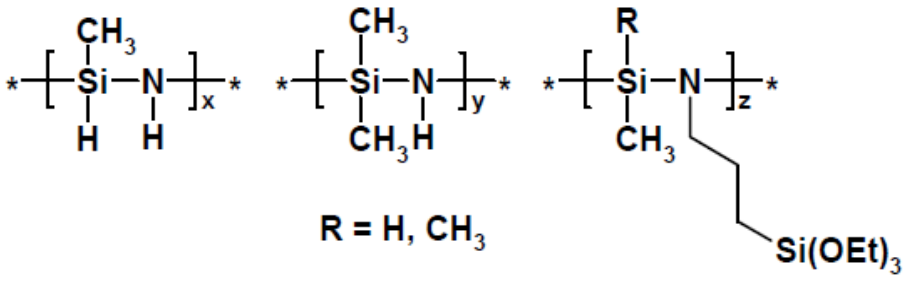

Figure 1: KION HTA 1500, mixture of the three molecules.

Technical data of KiON HTA 1500 Slow Cure are summarized in table 1. These products are especially designed for use in the formulation of ambient-curable coatings capable to withstand operating temperatures of 850 ºC or above [7]. The operating temperature depends on the exact formulation. It is supplied as 100 % polymer content. After application, the coating is dry-to-touch within 1 hour and is ready-for-use after 12 hours. The dry content of the product is around of 20 -70 wt. %.

The reason of the choice of polysilazane is that it possesses sufficiently high molecular weight to avoid volatilization of low-molecular components, and exhibits an appropriate solubility to be used for industrial rolling processes. It presents also reactivity (presence of functional groups) for rapid crosslinking and curing.

Table 1: Technical data of KION HTA 1500.

KION HTA 1500 is compatible with dry aprotic solvents (ester, ethers, dibutyl ether etc.)	
Viscosity	20 - 30 mPa.s (20 °C)
Polymer content	100 %
Flash point	16 °C
Shelf life	18 months from delivery date, at 20 °C
Crosslinking	270 °C during around 60 s
Curing	Room temperature: 8 to 12 hours 80 °C during 2 hours 130 - 180 °C during 1 hour 240 °C for a few minutes

II.2.2. Deposition procedures

Polysilazane coatings are prepared on stainless steel (SS) sheets. No polishing treatments were applied to the tested substrates.

The important points for polysilazane stacks deposition should be emphasized as follows. The deposition procedure starts with a cleaning of substrate. The cleaning is a crucial step to remove contaminations in order to promote the adhesion. Contaminants such as grease and dust commonly present on surface of commercial SS sheets strongly impede their covering by polysilazane coatings and limit their adhesion to the surface. The substrate cleaning is usually performed in successive ultrasonic baths using appropriate degreasing solvents followed by compressed-air drying. Classically, a sequence of dipping in acetone, water and alcohol with 600 seconds of duration in each bath is applied.

Substrates were then coated after drying with polysilazane sol-gel using several deposition techniques such as bar and spin coating processes (figure 2). The bar coating process is similar to the industrial rolling processes, while the spinning is not a roll-to-roll compatible process but is useful for deposition of very thin layers at lab scale. In our study, the bar coating process consists in depositing the wet hybrid-polymer by manually moving a coating bar on the surface of SS substrates as shown in figure 2.a. Some coatings are otherwise carried out using spin coating process (figure 2.b). In this case, spinning speed of 1500 rpm is used. The spin coating process is well documented in [8,9]. For all our polysilazane coatings, a rapid crosslinking is required and is performed either in a conventional oven (Mathis Labdryer) or on hot plate at 270 °C during 60 s as recommended by the supplier. Finally, coatings are exposed to air during 12 hours for a complete crosslinking before use.

Figure 2: Illustration of (a) the bar coating and (b) the spin coating processes mainly used for deposition of our polysilazane sol-gel coatings.

In bar coating processing, the thickness of resulting films depends on the viscosity of the used solution but also on the diameter of the spiral applicator. Bars with spiral applicators of 14 to 40 µm diameter steel wires are available in our lab (see detail of coating bar in figure 3).

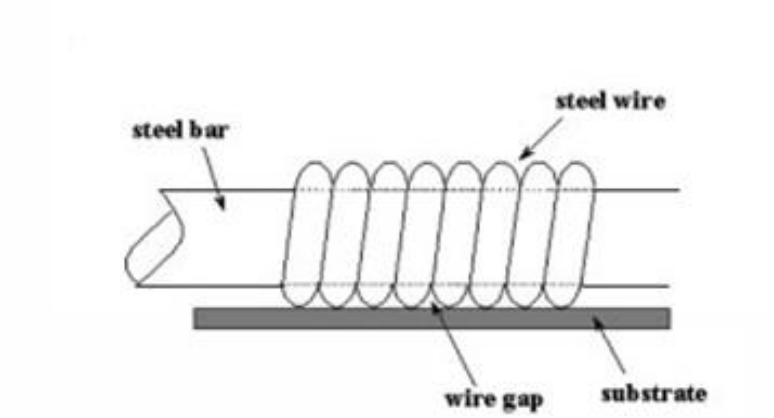

Figure 3: Illustration of coating bar to detail its different components.

Two variants of polysilazane have been tested and the main different between the two products rises from their dry content. The first product is called ZN100 with dry content of 75 wt. % while the second one called ZN200 exhibits a dry content of 20-50 wt.%. The evolution of thickness as a function of the diameter of the spiral applicator for ZN100 coatings is shown as an example in figure 4. As can be observed, the thickness of polysilazane coatings clearly increases with the diameter of the spiral applicator. Coatings obtained with ZN100 are all thicker than 2 µm even with the smallest spiral and are systematically cracked after annealing. Thus, we switched on ZN200.

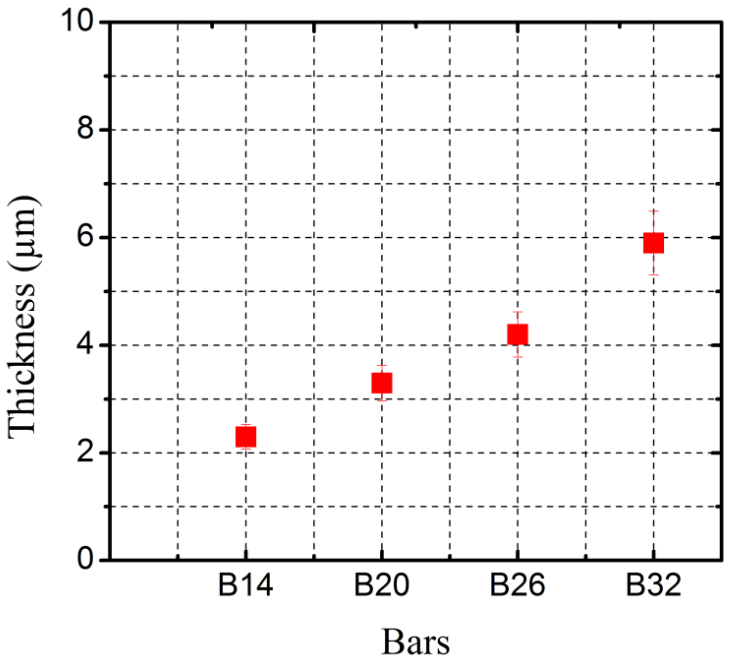

Figure 4: Evolution of thickness of ZN100 coatings versus the used bars. Numbers correspond to diameter of the spiral applicator involved.

ZN200 being less viscous than ZN100, it gives thinner films with the same coating bar. Coatings with thickness higher than 2 µm suffer from cracking after annealing; fortunately single layers with thickness lower than this value do not show this limitation. We found that the coating bar with a spiral applicator of 14 µm in diameter (B14) gives coatings definitely thinner than 2 µm (the ZN200 double layers are often lower than 2 µm). Thus, B14 is retained as the favorite bar for our depositions.

To obtain thicker films for good electrical insulation without cracking at high temperatures, stacks are explored. The first series of stacks are obtained by combining double layers of ZN200 deposited with B14. In this case, the second layer is prepared using exactly the deposition procedure used for deposition of the first layer. It was observed however that the deposition of subsequent coating failed especially when crosslinking of the first polymer layer is complete. The appropriate procedure found here is to apply the second layer immediately after rapid crosslinking of the first one. Efforts have also been done to deposit a third ZN200 layer on the first double layers directly but all are failed. This problem was solved by depositing a SiO_xAl_y layer prior to the third layer. SiO_xAl_y films (400 - 600 nm) are obtained from reactive DC magnetron sputtering using Kurt J. Lesker (KJL) equipment at CRM-Group, with a target-to-

substrate distance fixed at 17 cm. The magnetron sputter source was supplied with a DC power of 300 W and is connected with a pulse generator with a frequency of 50 Hz. During the deposition, the substrate holder was rotated around the central axis of the chamber at a speed of 20 rpm. Mixtures of argon and oxygen were used as sputtering gases; flows of O_2 and Ar were respectively 40 sccm and 72 sccm. The third sol-gel layer of ZN200 is then deposited on plasma SiO_xAl_y layer and crosslinked; it adheres well to subjacent layers. The whole stack forms a single unit that could be repeated as well as possible and is referred as reinforced polysilazane DBLs.

For reasons related to the fabrication of CIGS solar cells and a thermal stabilization of sol-gel coatings (details can found in II.4.1), our DBLs are annealed at temperatures up to 550 °C. The thermal treatments were done in three different atmospheres:

- in air;
- in vacuum or inert atmosphere such as argon;
- in HN_x (5 % H_2: 95 % N_2), this gas mixture is currently used in metallurgical technology to prevent oxidation during the annealing process and is often available on furnace used online. Thus, HN_x will be preferentially used for annealing our samples.

Finally, samples are currently completed with a 300 to 600 nm-thick layer of sputtered Mo. The base pressure for sputtering was approximately 4×10^{-5} Pa while the total working pressure was kept constant at around of 9 Pa. Schematic overview of ZN200 based DBL stacks is reported in figure 5 highlighting steps of depositions.

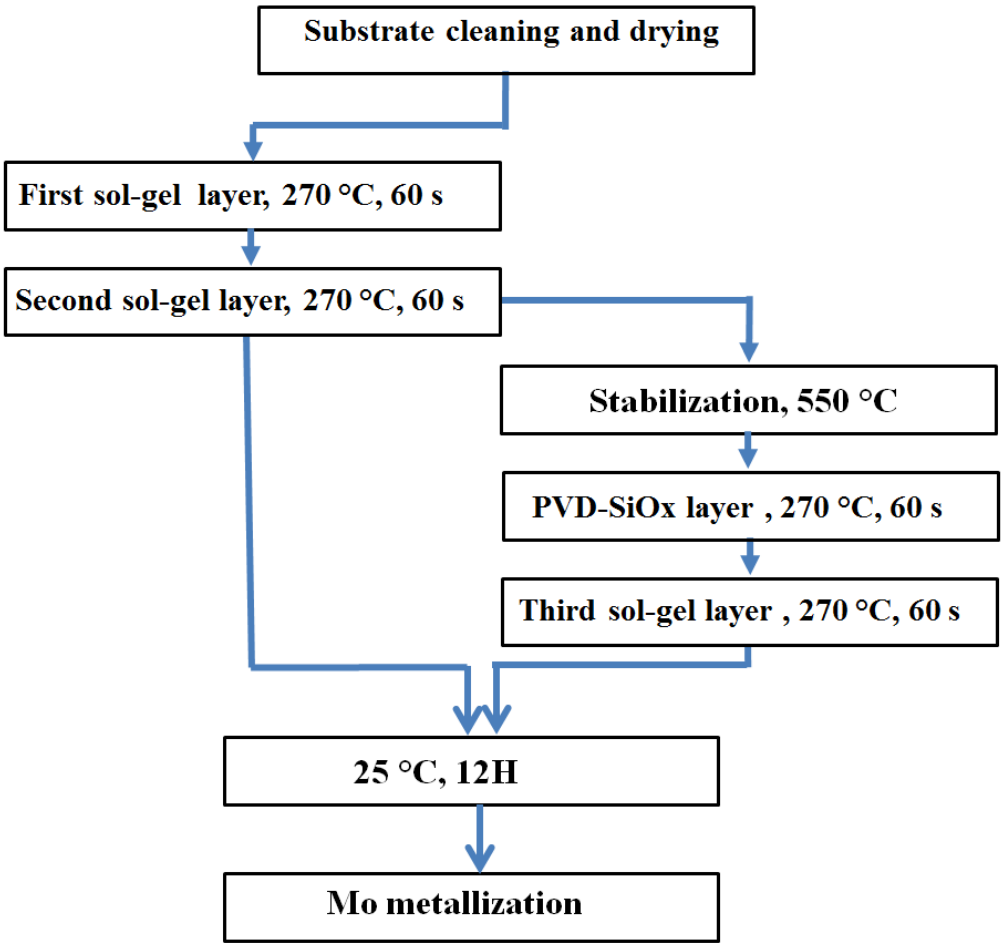

Figure 5: Processing steps of ZN200 polysilazane based DBLs tested.

II.3. Samples characterizations

II.3.1. Microscopic analysis

The morphology of our coatings was examined using Scanning Electron Microscopy, SEM, (Zeiss Ultra 55) at CRM-Group with an acceleration voltage of 10 kV and Atomic Force Microscopy (AFM). AFM images were recorded in air, in intermittent-contact mode (IC-AFM) with a Nanoscope III from Veeco Instruments at the University of Namur. Silicon cantilevers with a resonance frequency around 300 kHz and a typical spring constant of 40 N/m, were used together with an integrated silicon tip with a nominal apex radius of curvature lower than 10 nm. Soft-tapping conditions were used for hybrid polymer coatings, i.e. the ratio between the set-

point amplitude and the free amplitude of the cantilever vibration was always kept above 0.8. The surface roughness is evaluated over two areas: 40 μm × 40 μm and 1 μm x 1 μm.

II.3.2. Spectroscopic analysis

II.3.2.1. GDOES analysis

Glow Discharge Optical Emission Spectrometry (GDOES) [10] suitable for the analysis of nearly all elements including hydrogen, oxygen, carbon etc. in films of few annometers up to more than hundred micrometres of thickness is used to determine atomic concentration profiles in our coatings. GDOES is characterized by a high sensitivity (detection limit 0.1-10 μg/g) and high dynamic range (μg/g up to main components) [11]. The instrument consists of a discharge lamp, an optical spectrometer and a data acquisition and processing system. The operating principle of GDOES can be summarized as follows: Atoms from the tested sample are sputtered, ionized, excited and they emit characteristic light in the discharge plasma, which is then detected by an optical spectrometer. The detectors can be either photomultiplier tubes (PMTs) or charge coupled devices (CCD). The depth resolution of GDOES is around 5 - 10 % of the sputtered depth [12]. A modern commercial GDOES spectrometer (Spectruma, GDA 750) at CRM – Group is used for characterization of our samples.

For processing aspects, one should mention that the shape of the sputtered crater might be optimized to reach the best depth resolution. Adjustable parameters are mainly voltage and current. Suitable operating conditions were fixed to 8 W - 14 W and 700 V. In figure 6.a and b are respectively shown typical 2D and 3D interferometry images of GDOES spots obtained on our ZN200 coatings on SS substrates. Measurements of sputtered craters are performed using white light optical interferometry (Wyko NT 9100 from Vecco) at CRM-Group. The lateral resolution of this last technique is around 1 μm while the depth resolution is approximately 20 nm. As can be observed, craters have narrow edges with a moderately flat base.

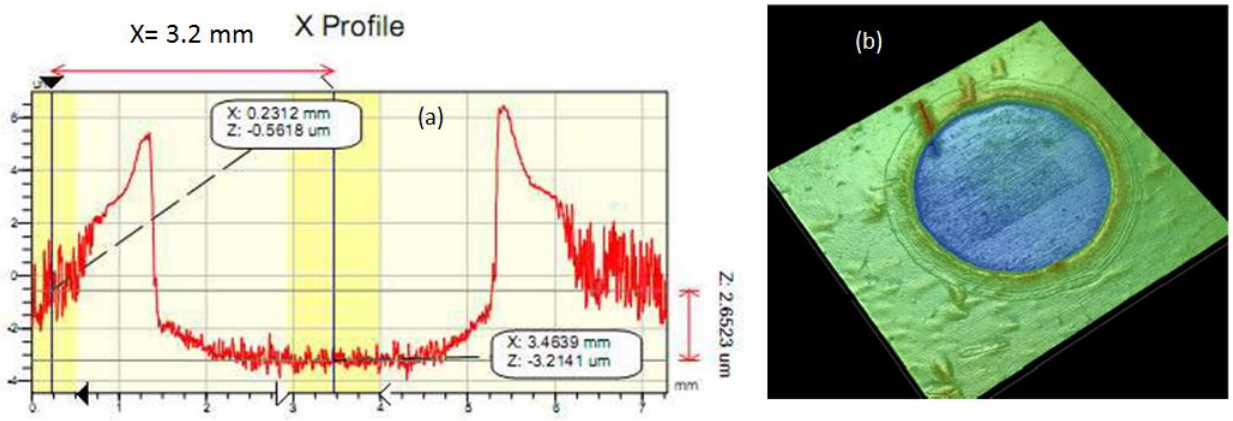

Figure 6: GDOES ion beam rastering of ZN200 coatings on SS substrate. a) 2D and b) 3D interferometer images.

II.3.2.2. SIMS analysis

For high resolution analysis of depth profiling, time of flight secondary ion mass spectroscopy (ToF-SIMS) is used to complement GDOES analysis. In SIMS the surface of samples is sputtered by an ion beam, removed layer by layer; ejected particles are analyzed using a mass spectrometer. Quantitative concentration-depth profiles with a depth range of only a few nanometers up to more than 10 µm can be recorded with this technique. SIMS gives access to chemical analysis of surface/interface, detection of trace elements with a very high degree of sensitivity to all elements including hydrogen (< 1 ppm). The technique has become a key tool for probing inter- and intradiffusion phenomena. The ION-TOF/ToF-SIMS 5-100 apparatus at the University of Namur is used for checking our DBL/SS systems and quantify the diffusion of poison atoms previously identified in chapter I for CIGS solar cells. Spectra were acquired in both positive and negative polarities over a mass range of m/z = 0 to 860. The rastering of the primary ion beam is over an area of 100 × 100 µm² or 200 × 200 µm² and the primary ion current was 1.5 pA.

II.3.3. Thermal analysis

II.3.3.1. TGA analysis

Thermogravimetric analysis or thermal gravimetric analysis (TGA) is used to access information about phase transitions occurring in our coatings and to investigate their thermal stability. TGA is a method in which changes in physical and chemical properties of materials are measured as a

function of increasing temperature (with constant heating rate), or as a function of time (with constant temperature and/or constant mass loss). TGA can provide information about physical phenomena such as second-order phase transitions including vaporization, sublimation, and absorption and desorption. The technique can also give information about chemical phenomena including chemisorption, desolvation (especially dehydration), and decomposition and solid-gas reactions (e.g.: oxidation or reduction). We used TGA (Setaram TG-DSC 111 of University of Namur) to check the thermal stability of our sol-gel coatings in air and argon atmospheres. As explained earlier, HN_x should be appropriate but is not available on the used TGA machine. TGA is combined with Differential Scanning Calorimetry (DSC). DSC is a thermoanalytical technique in which the difference in amount of heat required to increase the temperature of a sample and reference is measured as a function of temperature. To do so, liquid form of ZN200 polymer and powder were prepared and are pyrolyzed with a heating rate of 1°C/min up to 600 °C.

II.3.3.2. Micro-ATR analysis

Understanding curing reactions, thermal decomposition and crosslinking of our polymers-based hybrid sol-gel coatings is an integral part of this work. To do this, we used Fourier Transformed Infrared (FT- IR) in micro Attenuated Total Reflectance (micro-ATR) mode carried out on Nicolet iN10 MX from Thermo Scientific instrument available at CRM-Group to complement or to detail TGA analysis. The principle of micro-ATR is based on the interaction between matter and infrared (IR) radiation which occurs when the dipole moment changes during the vibration of chemical bond within the tested coating. Different bonds and functional groups will result in IR absorptions at characteristic wave numbers. The resulting IR spectrum can be considered as a fingerprint of the molecule or material. All FT-IR spectroscopies can offer information on various chemical functional groups present in the material.

Here, IR spectra were recorded between 400 cm^{-1} and 4000 cm^{-1} using germanium crystal with penetration depth of 0.2 to 0.6 µm and resolution of 4 cm^{-1}. Micro-ATR is dedicated to surface analysis and is well established in FTIR spectroscopy for direct measurement of solid materials without sample preparation. Thus, our sol-gel coatings are thick enough to enable not to detect SS substrates.

II.3.4. Thickness and adhesion measurements

Thicknesses of our coatings are determined from SEM observations on samples cross sections. Another method used here especially to determine thicknesses of our plasma coatings is profilometry (Dektak instrument available at CRM-Group). Cross-cut and tape standard tests were used to measure films adhesion according to ASTM D3359-07 Standard Test Methods [13].

II.3.5. Electrical measurement

- **Equipment for electrical measurement in DC mode**

All electrical investigations are done in ambient atmosphere at room temperature. Constant voltage stressing (CVS) and dielectric breakdown tests have been performed on MIM capacitors using a test bench illustrated in figure 7. For stressing up to 1000 V, a high voltage power supply (HVPS) operating at 0 – 1 KV is connected in series with a Keithley 2400 and is used as ammeter (figure 7.a). For measurements involving voltages lower than 200 V, Keithley source meter is sufficient and is used in the voltage input / current output mode (figure 7.b). Keithley 2400 is sensitive to the range of 10 pA to 1 A input current.

The source meter is driven by two different softwares developed under LabView. The first one allows reading leakage current values over time by means of the source meter station and is especially required when HVPS is used because in this case the voltage is applied manually. The second software permitted to drive the voltage source and read current values versus time. The current compliance of the source is fixed to 20 mA.

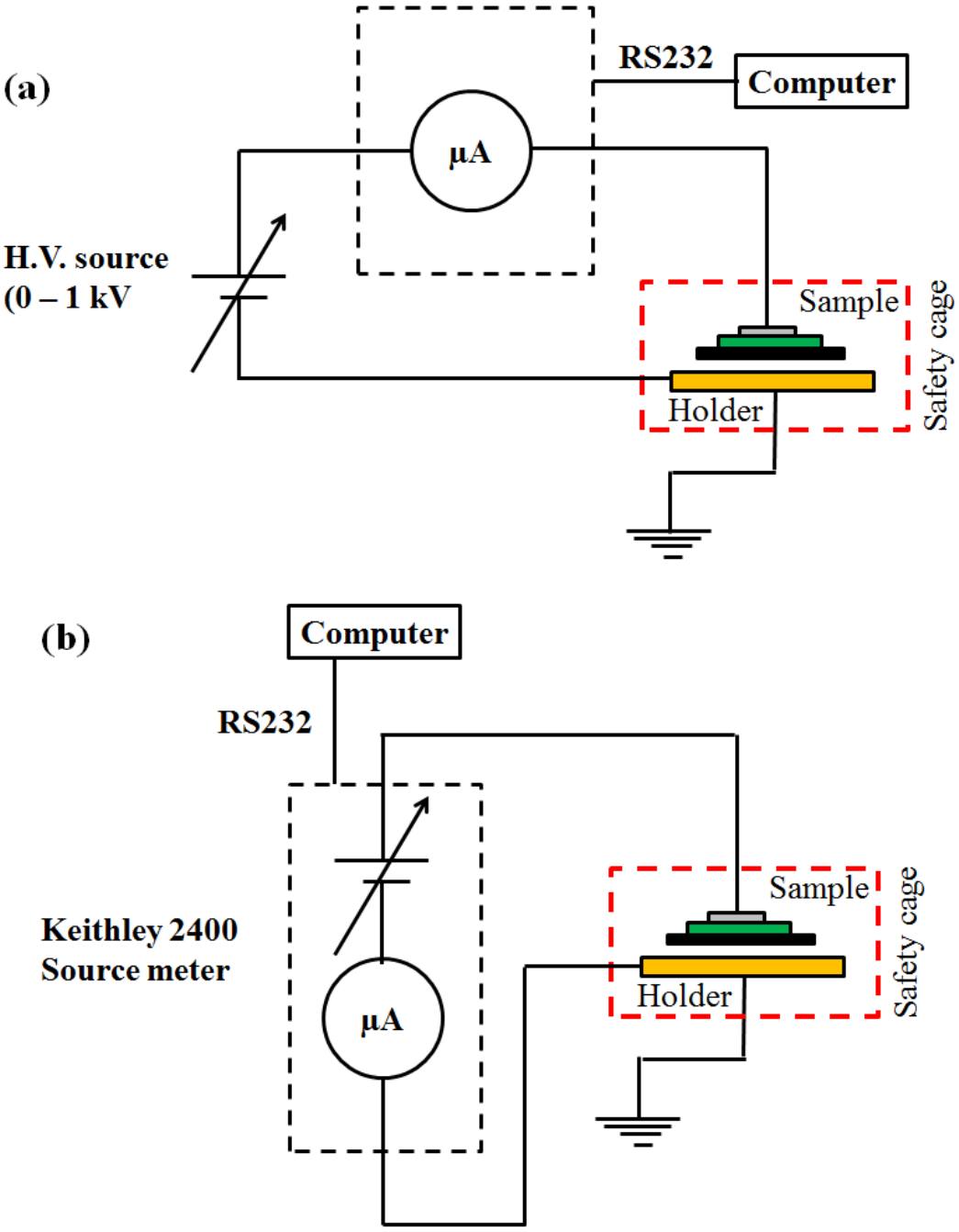

Figure 7: Illustration of system used for constant voltage stressing (CVS): a) for high voltage measurement where the high voltage power supply is connected with Keithley source meter which is used as ammeter, b) for voltage lower than 200 V.

- **Equipment for electrical measurement in AC mode**

The Novocontrol Alpha A analyser set up of ICTEAM, Electrical Engineering, Université Catholique de Louvain, is used for our characterization in dielectric spectroscopy. Novocontrol

Alpha is a high performance inductance, capacitance and resistance (LCR) meter with characteristics summarized in table 2. The analyser has an ultra-wide impedance range (10^{-2} to 10^{14} Ω) and covers materials ranging from conductors to good insulators. Operation, data acquisition, data evaluation and graphical representation are conducted using WinDETA software. Alpha A offers resolutions of 0.002° and 3.10^{-5} for phase and loss factor respectively.

Table 2: Technical data of the spectroscope analyzer used.

Characteristics	**Novocontrol Aplha**
Frequency range	3.10^{-6} Hz – 20 MHz
DC voltage out	+/- 40 V
AC voltage out	100 µV – 3 V
Impedance range	10^{-2} Ω – 10^{14} Ω
Capacitance	1fF – 1 F
Software	WinDETA

Figure 8 shows a basic operating principle of an LCR-meter. The characterization of metal-insulating-metal based capacitors is achieved by applying an alternating voltage (or current) and measuring the current (or voltage) over frequencies. Measurement of the output signal is possible thanks to current to voltage converter (operational amplifier). The comparison of both current and voltage amplitudes gives access to magnitude of the complex impedance while the phase shift allows to reach the ratio between imaginary and real parts of the impedance.

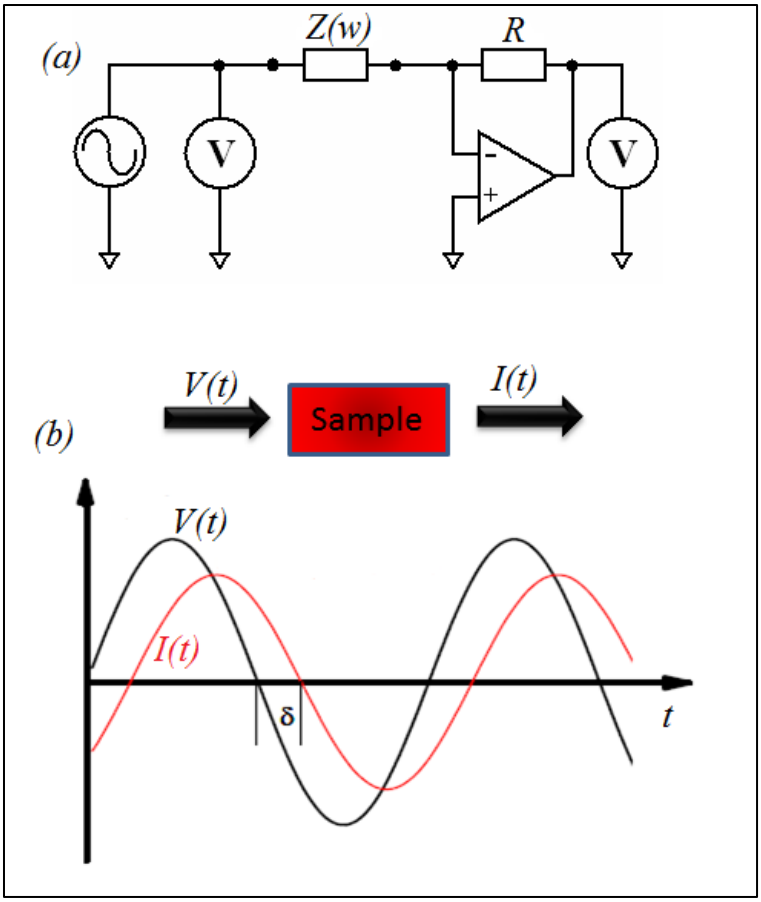

Figure 8: (a) Basic principle of LCR -meter and (b) dephasing between applied voltage and the leakage current.

II. 4. Results and discussion

Physical and chemical properties such as morphology, adhesion, thermal stability, structural, electrical and diffusion barrier properties are investigated to validate insulating DBLs requirements for our ZN200 based stacks. Results of characterizations of all these aspects are reported in the following sections.

II.4.1. Thermolysis of ZN200

II.4.1.1. Curing of ZN200

Micro-ATR analysis has been performed using infra-red analysis to investigate the curing and the chemical evolution of ZN200. Three different samples have been considered: coatings deposited at room temperature, coatings deposited at room temperature and cross-linked in air at temperatures up to 270 °C, and coatings annealed at temperatures up to 550 °C in vacuum.

Micro-ATR spectra of the different samples are shown in figure 9. Several absorption regions could be identified for ZN200 films deposited at room temperature (figure 9, black curve). The vibration peak close to 2959 cm^{-1} is identified as a stretching of CH_3 groups [14] while small peaks located approximately at 1650 cm^{-1} and 1400 cm^{-1} are assigned to vibrations of H_2O and H-O bonds respectively. The presence of water could result from the fact that tested coatings are exposed to air before ATR characterization. Moreover, both Si-CH_3 bonds symmetric stretching and Si-H bonds stretching are located near 1260 cm^{-1} and 2360 cm^{-1} respectively [15]. Vibrations of O-Si-CH_3, Si-O-Si and Si-NH-Si bonds are found close to 777 cm^{-1}, 890 cm^{-1} and 1077 cm^{-1} respectively [16,17]. Peaks corresponding to Si-NH-Si and O-Si-CH_3 bonds are remarkably intense.

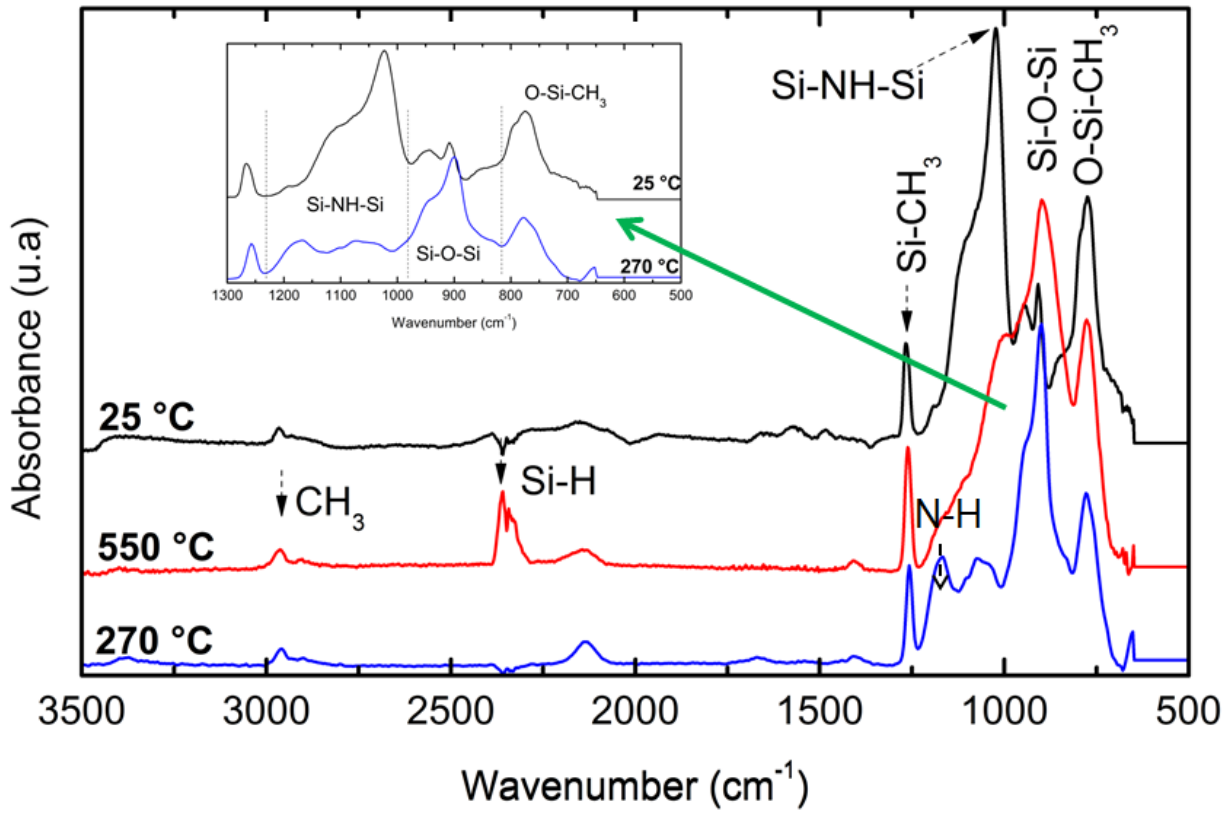

Figure 9: Micro ATR spectra of ZN200 (black) deposited at room temperature, (blue) coatings deposited at room temperature and cross-linked in air up to 270 °C and (red) coatings cross-linked up to 270 °C following by annealing up to 550 °C in vacuum.

ATR analysis was also performed on coatings annealed up to 270 °C in air according to our crosslinking procedure (figure 9, blue curve) to check the crosslinking of ZN200. Significant changes can be clearly observed. Compared to as-deposited samples, the intensities of Si-NH-Si and O-Si-CH_3 noticeably decrease and could result from an evolution of ammonia (NH_3) and CH_4 [18]. Besides, the intensity of the peak assigned to Si-O-Si vibrations is substantially increased. These changes are a signature of polymer crosslinking which occurs through reactions of hydrolysis and condensation as illustrated schematically in figure 10 [19].

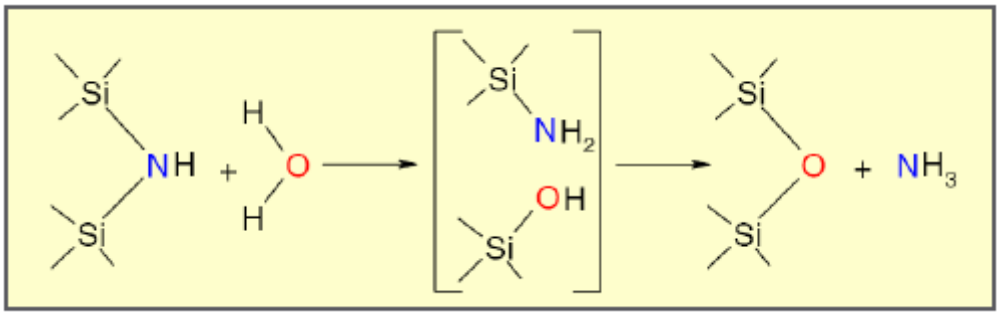

Figure 10: Crosslinking of polysilazanes through hydrolysis and condensation reactions.

The red line in figure 9 corresponds to micro-ATR spectrum for ZN200 annealed up to 550 °C in vacuum to evaluate effects of temperature in inert atmosphere. It can be clearly seen that peaks related to vibrations of Si-HN-Si groups are definitely suppressed when the contribution of Si-O-Si bonds are more intense. The broadening of peaks related to Si-O bonds is especially pronounced. There is no evidence of a difference between intensities of O-Si-CH_3 vibrations for cross-linked and annealed samples; both peaks are however clearly lower than that of as-deposited samples. This effect can be assigned to the conversion of our ZN200 hybrid polymer into a $SiC_xN_yO_z$ based pre-ceramic quaternary compounds.

Micro-ATR analysis seems to confirm the curing of ZN200 coatings using our procedure of crosslinking and clearly reveals the evolution of chemical components such as HN_3 and CH_4 during thermal treatments The evolution of such chemical components can generate pinholes in the sol-gel coating with a reduction of mass as a consequence.

II.4.1.2. Mass loss of ZN200

- ***Analysis in air atmosphere***

Figure 11 depicts the TGA curve of the liquid form of ZN200 in air from room temperature up to 680°C. Different peaks observed in mass change and heat transfer curves mean that the decomposition of the liquid precursors results in several transitions steps. It can be checked in part I of figure 11 that below 100 °C, no weight loss is detected. Between 100 °C to 200 °C however a significant mass loss of 16 wt. % is measured (see figure 11, part II). This could correspond to a release of solvent followed by a start of polymer crosslinking. The main solvent in ZN200 is metoxy-1-methyl ethyl acetate, $C_6H_{12}O_3$ with a concentration of 50 - 70 % and a

boiling point of 146°C. The solvent releasing is evidenced by the endothermic peak detected in the heat flow curve at around 145°C.

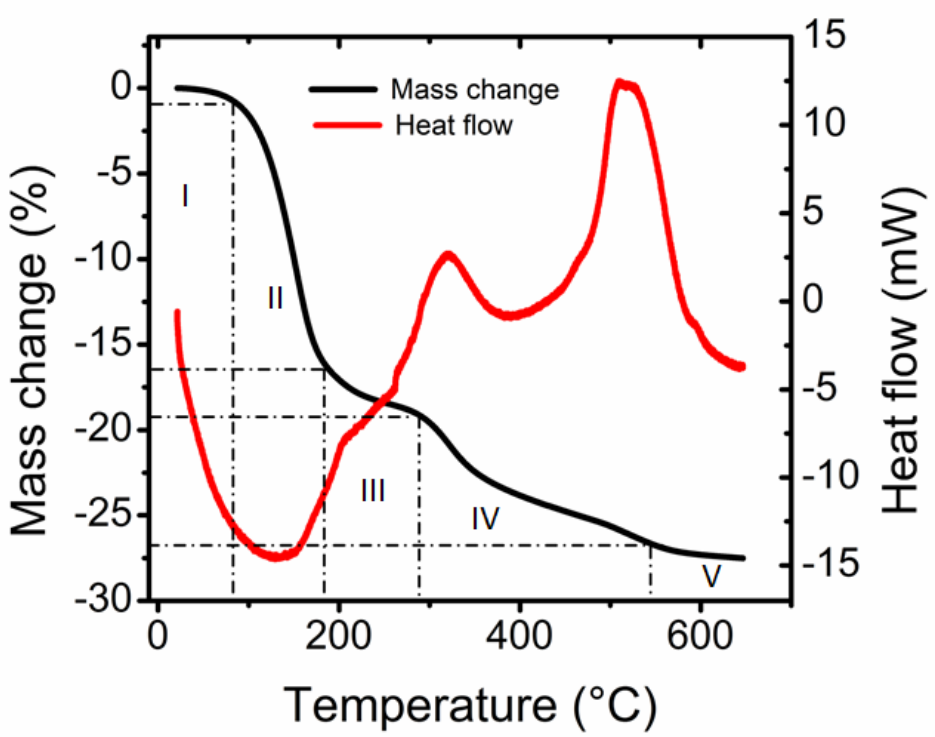

Figure 11: TGA analysis of ZN200-liquid in air at temperature up to 680 °C.

In the range of temperature of 200°C to 300°C (figure 11, part III), the liquid form of polysilazane should be progressively converted into solid materials due to a crosslinking of molecular chains followed by a release of NH_3. The total mass loss of 19 wt. % is probably caused by solvent evaporation combined with volatilization of some lower molecular weight in silazane compounds, and is in agreement with results in [20]. In the range of 300°C and 550°C (figure 11, part IV), the pyrolysis or mineralization of polymer may really have started; the mass loss related to this step of transformation is around 7 wt. %. This is remarkably lower than the mass loss observed in step of polymerization (part II) and is possibly a signature for the initiation of conversion into pre-ceramic of the solid hybrid polymer formed during the crosslinking phase of our polysilazane precursors. The maximum gas release is observed at temperatures around 500°C and could be related to exothermic reactions due to decompositions, probably of residual metoxy-1-methyl ethyl acetate solvent and the polymer into hydrocarbons (methyl, ethyl etc.). The second exothermic peak could be explained by a transamination reaction of ZN200-based

polymer at temperature comprised between 400 °C and 450 °C where HN_3 spices should be generated as found in [21]. Different mechanisms are summarized in table 3.

Table 3: Summary of mechanisms occurring during TGA analysis in air.

Different parts	**Mechanisms**
Part I (25 – 100 °C)	The liquid polymer is stable.
Part II (100 – 200 °C)	Solvent evaporation
Part III (200 – 300 °C)	Crosslinking of the polymer
Part IV (300 – 550 °C)	Decomposition of a part of polymer into hydrocarbons (methyl, ethyl…)
Part V (> 550 °C)	Thermally stabilized. Conversion into hard coating

Gonon and co-workers [22] investigated the thermal behavior of polyvinylsilazane and found four steps of thermal transformation of polymer similar to transformation steps observed here. They also evidenced two large peaks for NH_3 species in mass spectroscopy; the first peak is observed between 100 and 300°C while the second peak is observed in the range from 300 to 600°C.

For practical aspects, TGA examination should be based on pyrolytic behavior evaluation of ZN200 films on SS substrates. However, the compartment of sample holder available on TGA equipment used for characterizations is limited to 5 × 15 mm^2. Thus, only a small amount of ZN200 could be deposited on these size-limited substrates. Some tests have been done in this direction but unfortunately failed. To approach an estimation of the pyrolytic behavior of ZN200-films, TGA-DSC analysis has been performed on a powder obtained from ZN200 precursors beforehand cross-linked (see section 2.1.2, chapter II). Figure 12 depicted TGA-DSC curves performed on ZN200-powder in air from room temperature to 680 °C. Two important steps can be observed in powder conversion.

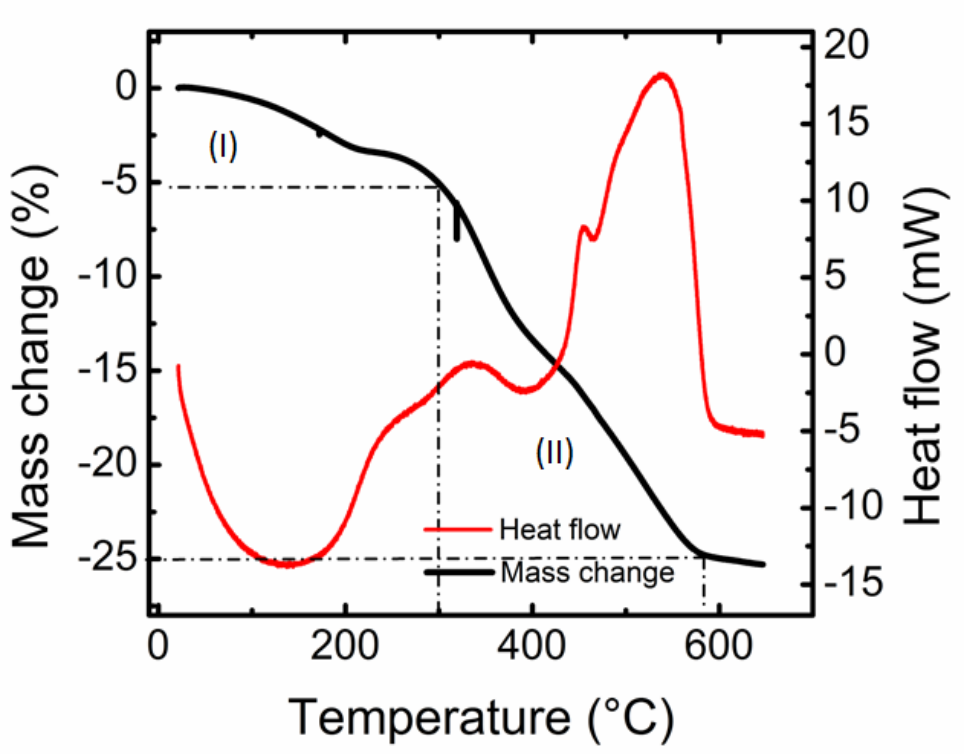

Figure 12: TGA analysis of ZN200 powder in air at temperature up to 680 °C.

In the first transition corresponding approximately to the range from 25°C to 300°C (figure 12, part I), a clear endothermic effect has been detected. During this step, the absorbed heat (from the oven) can help in increasing the density of the cross-linked chains of polymer [23]. This should be a signature of the fact that the process of crosslinking of ZN200 precursor molecules to form a higher molecular weight polymer found to be initiated in the first procedure is not complete. In other terms, the vulcanization of ZN200 polymer is not achieved during the crosslinking procedure. Moreover, a mass loss of around of 5 wt. % is observed in the same transformation phase and may result from evolving of ammonia (NH_3). This result is in accordance with data published by Breuning et al. in [24] where the pyrolysis transformation of polysilazane precursors obtained from ammonolysis of methylchlorosilane was investigated using TGA coupled with pyrolysis-gas chromatography-mass spectrometry (Py-GC/MS) techniques. At temperatures up to 350 °C, they considered the measured mass loss of polymer as a consequence of volatilizing of ammonia.

Between 300°C and 600°C, a major mass loss (the total mass loss is 25 wt. %) is detected due to the final conversion of the polymer into pre-ceramic. This transformation corresponds probably

to the escape of alkyl groups and hydrogen via the observed exothermic reactions. The sharpness of the mass loss curve is similar to that previously observed in the same temperature range for the liquid form of ZN200. In this step, the breaking of chemical bonds can mainly occur and the peak detected at 500°C in the heat transfer spectrum relates to exothermic reactions of these chemical compounds, because the chemical species found in the literature for most of OPSZs precursors in the range from 300°C to 600°C are mainly methane, propane, ammonia and hydrogen [25]. Above 600°C, the curve of mass loss even for that of the heat flow is quite stable. The stabilization of both mass loss and heat transfer processes observed can be assigned to the end of the escaping of volatile species which could give place to the three dimensional reorganization of the solid hybrid polymer.

- ***Analysis under argon atmosphere***

Studying the pyrolysis behavior of ZN200 in liquid and powder forms has to be carried out in vacuum to reproduce the conditions of full vacuum solar cells processing. The TGA machine used for our characterization is however not equipped with a vacuum chamber thus analyses are carried out in argon. Results of thermal degradations in vacuum should be different even if argon is an inert atmosphere. Results of characterization in argon are shown in figure 13. It is found that the conversion of the liquid form takes place in five steps similarly to what is found in ambient (see figure 12). As can be checked, the total mass loss (50 wt. %) at 600°C is surprisingly two times higher in argon than in air (around of 27 wt. %). This should result mainly from the contribution of the second conversion step (figure 13, part II) where the mass loss is highly or remarkably pronounced. It could be considered as a consequence of the escape of a large amount of solvent (50 - 70 wt. %) related to an important endothermic peak with its maximum at 150°C observed in heat flow curve. However, the fact that the mass loss is two time higher than in air (competition with probable oxidation in air) is something surprising and has to be clarified.

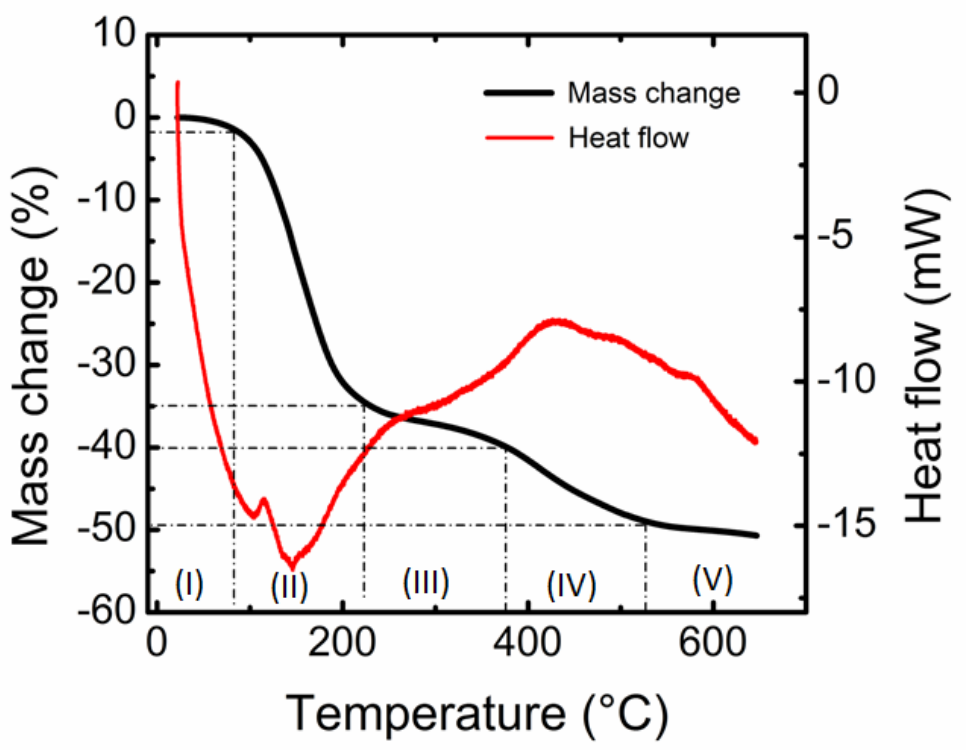

Figure 13: TGA analysis of ZN200-liquid in argon atmosphere from room temperature to 680 °C.

The TGA curve of ZN200 powder in argon is shown in figure 14,. it exhibits two mass losses located between 25°C and 200 °C and between 200 °C and 600 °C with a total mass loss of around of 25 wt. % which is comparable to that found in air. In the heat flow curve, an important peak located at 150 °C is observed and can be a signature of the release of the rest of solvent. The exothermic peak observed in air is definitely suppressed; this is difficult to interpret without any mass spectroscopic analysis. Nevertheless, these results reveal the fact that in air, there should be a competition between the mass loss and oxidation of PZS which has been shown to start at 270°C [26,27,28]. Mass gain in air could not be quantifiable here. One can however imagine that the oxidation slightly increases a mass in air with gained amount probably much lower than that lost. As a consequence, the mass loss can be reduced in air than in argon.

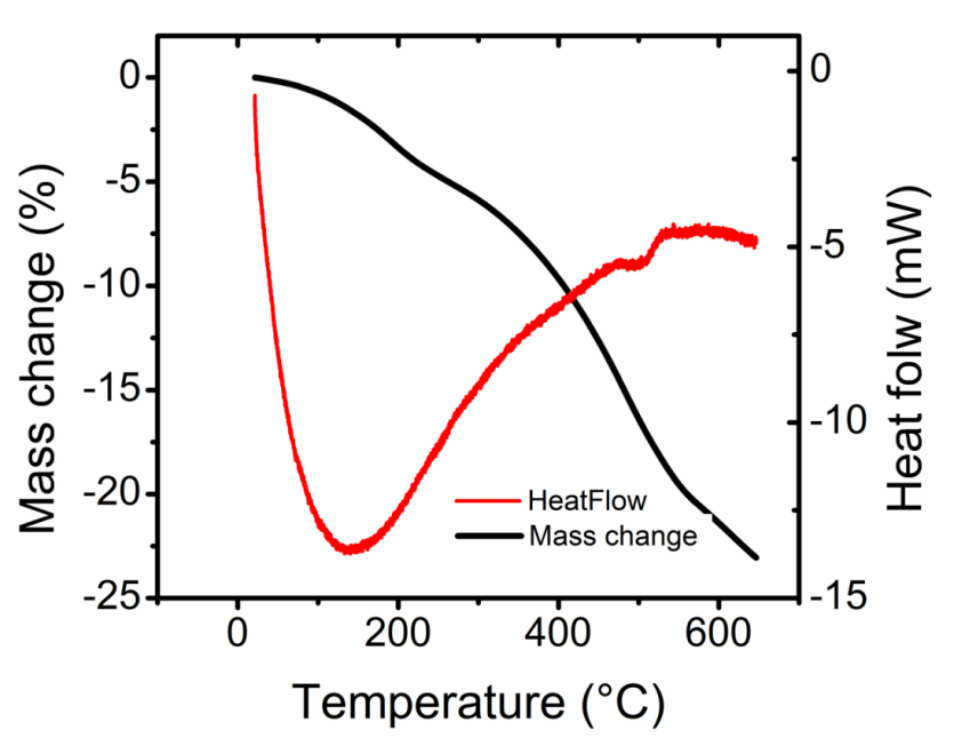

Figure 14: TGA analysis of ZN200-B powder in argon atmosphere from room temperature to 680 °C.

Compared to ZN200 powder in air where the thermal stabilization can be clearly seen from 600°C, the mass of ZN200 powder in argon still decreases in this range of temperatures. Thus, TGA analysis is performed on ZN200 powder at a fixed temperature of 550°C during 11 hours in argon to evaluate the thermal stability properly. As it can be observed in figure 15, the total mass loss is about 5 wt. % and the heat flow is stable over time. One can then consider that ZN200 coatings are also thermally stabilized around 550 to 600°C in inert atmosphere.

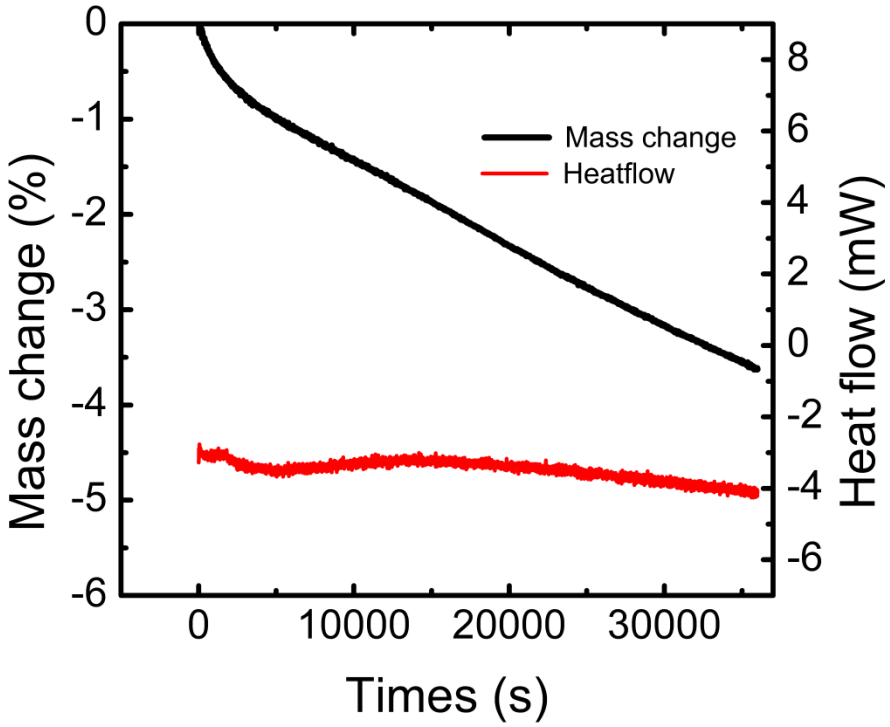

Figure 15: Thermal stability of ZN200 at 550 °C in argon using TGA analysis.

In summary, TGA analysis in both air and argon atmospheres reveals an important mass loss for ZN200. It has been shown that the mass reduction should be caused by chemical transformations such as volatilizing different gases and the evolution of solvent is clearly seen. Crosslinked ZN200 seems to have a similar behavior in both air and argon atmospheres. The general tendency of the mass loss seems showing stability at temperatures around 550 - 600°C with approximately a total mass loss of 25 wt. %. The stabilization can be otherwise related to the pre-ceramization previously observed in ATR analysis for our coatings annealed up to 550°C. Several other negative impacts unattainable neither in ATR nor in TGA can be met occur in our coatings during annealing. The mass loss can lead to the generation of pinholes and a reduction of the thickness of coatings as an example. The surface morphology of the polymer coatings can be also impacted. The mass loss and gases volatilizing can otherwise strongly impact mechanical strength of subsequent layers such Mo films. These impacts can be investigated using microscopic analysis.

II.4.1.3. Effects of mass loss of ZN200 on Mo films

To check effects of thermal evolutions of crosslinked ZN200 coatings on molybdenum subsequent layers, a set of Mo/ZN200/AISI316 samples have been annealed in air and HN_x (for validation in atmosphere appropriated to industrial process). In figure 16 are shown SEM images of representative samples. Figure 16.a shows Mo films from non-annealed samples and it can be observed that samples are cracked without any exfoliation. When samples are annealed up to 550°C (figure 16.b), Mo films are completely exfoliated and the surface has the visual appearance of "cream brûlée". Exfoliation of Mo films could be a consequence of differential thermal dilatation; it could also result from confinement of volatile gases under Mo films during annealing. The formation of such gas was indeed observed by ATR and TGA analysis. The same type of analysis has been also conducted in air (images not shown) and the stack is completely exfoliated.

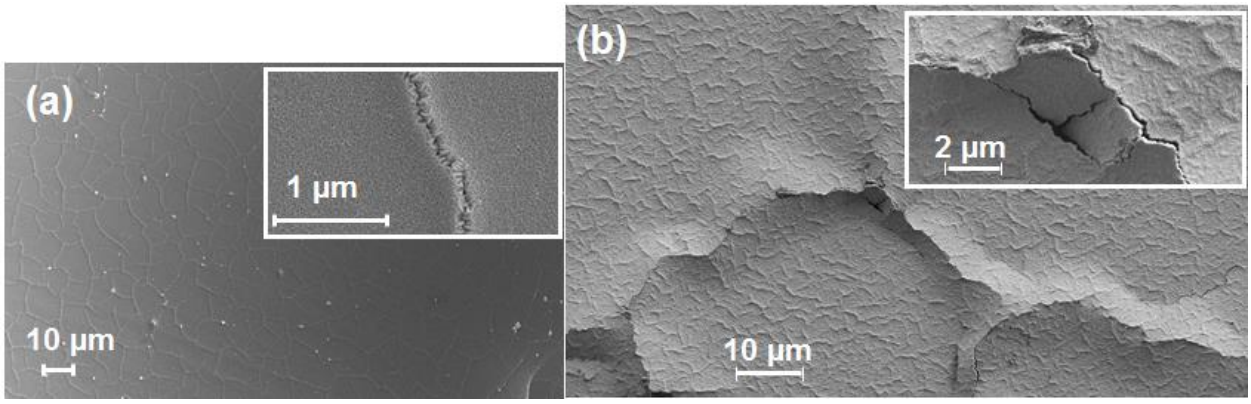

Figure 16: SEM micrographs of 300 nm-thick Mo films deposited at 0.53 Pa onto AISI316 SS substrate coated with ZN200 coating. a) Non-annealed sample and b) sample is annealed at temperature up to 550°C in HNx.

II.4.1.4. Effects of temperature on thickness of ZN200 coatings

To check the effect of annealing on thickness, cross sectional SEM has been performed on crosslinked and annealed coatings and the corresponding images are shown in figure 17.a and b. It can clearly be seen that the thickness of coatings is significantly reduced after annealing up to 550°C. The average thickness measured at ten different points reveals that it is reduced from 1.8 µm to 1.5 µm, corresponding to 17 % decrease in thickness.

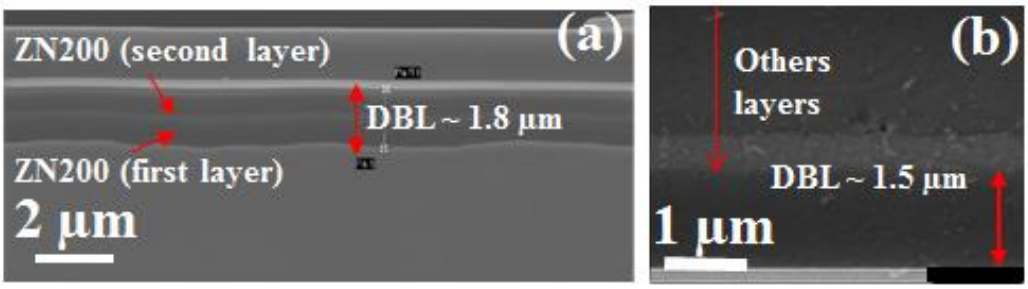

Figure 17: Cross-sectional SEM image of (a) non annealed ZN200 double layers and (b) ZN200 double layers annealed up to 550 °C.

II.4.1.5. Effects of temperature on morphology of ZN200 coatings

In this section, effects of thermal degradation on the morphology of ZN200 coatings prepared on AISI316 and AISI430 stainless steel (SS) substrates have been examined using AFM and SEM techniques. Especial emphasis has been put on comparisons of the roughness and morphology of uncoated and ZN200coated SS substrates to evaluate planarization effects of ZN200 hybrid polymer coatings.

Figure 18 shows AFM images of uncoated AISI316 substrate before cleaning recorded in tapping mode. As can be checked, regular streaks resulting from rolling process are observed on steel surface. The maximum surface roughness (Rz) value is 500 nm while the average roughness (Ra) or Root Mean Square (RMS) value is equal to 56 nm.

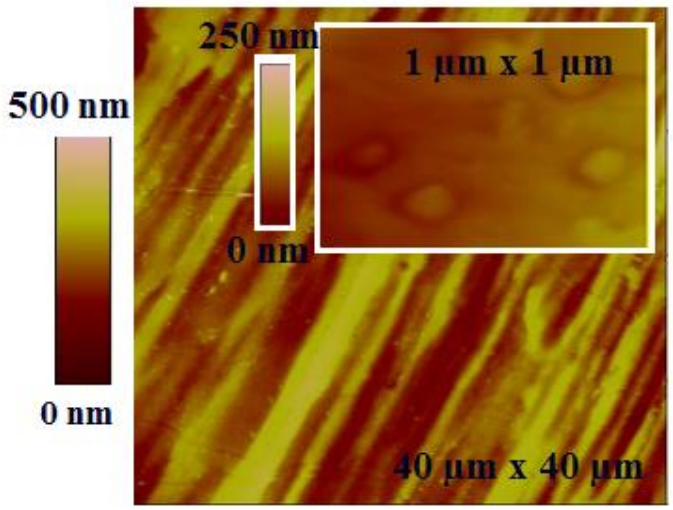

Figure 18: Typical AFM image of uncoated AISI-316-2RB substrate.

Figure 19.a shows topographic AFM images (40 µm x 40 µm and 1 µm x 1 µm) and SEM image (1 µm x 1 µm) of a representative ZN200 films freshly deposited and crosslinked on AISI316 SS substrate while figure 19.b shows images recorded on the same type of samples annealed up to 550 °C under a HN_x atmosphere and cooled down. Neither cracking nor exfoliation is observed on both kinds of samples. Coatings look visually smooth. In 40 µm × 40 µm AFM image, one can observe wave-effects. This could be related to the presence of streaks initially detected on steel surface. The only difference remains in the presence on annealed sample of few embedded particles in the annealed ZN200 coatings. Origins of these particles are not well clarified yet but they could be assigned to coagulation of polysilazane precursors or impurities. Coatings are processed in ambient atmosphere therefore they are subject of dusts contamination.

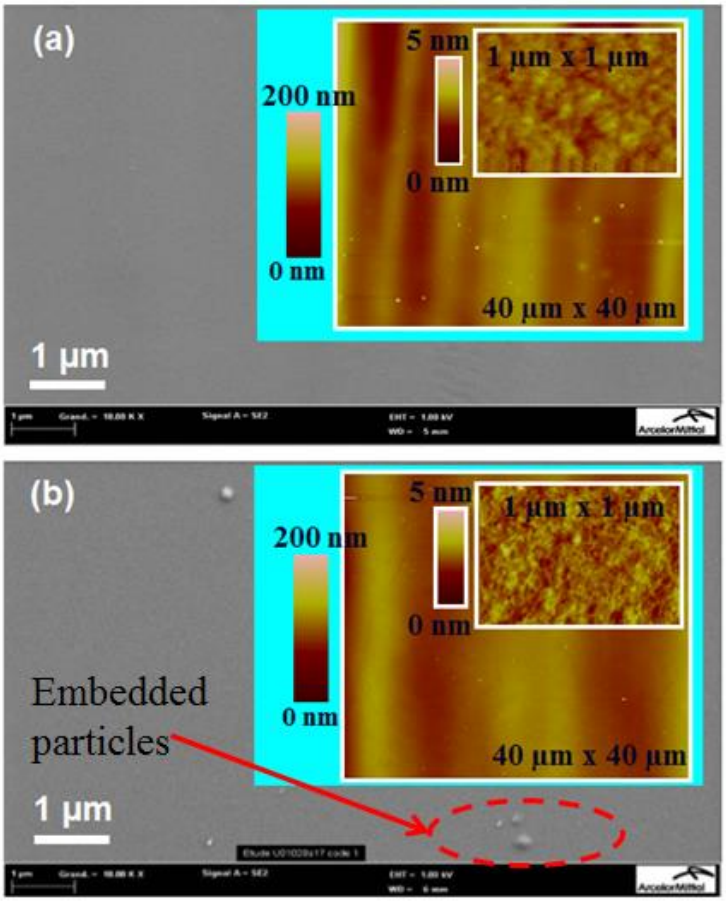

Figure 19: SEM and AFM images of (a) as-deposited ZN200-based coatings and (b) ZN200-based coatings annealed at 550°C in HN_x on AISI-316-2RB substrates.

Values of surface roughness of non-annealed and annealed samples are also measured from AFM images processing and are compared to that found for uncoated substrates (table 4). For

non-annealed ZN200 coatings, RMS is around of 8 nm while R_z is approximately 90 nm. Both the maximal and the average roughness values are approximately five times lower than values reported on uncoated steel substrates. This confirms the fact that ZN200 coatings significantly reduce the surface roughness of SS substrates. After the annealing, values of the roughness become slightly higher and are around 176 nm and 16 nm for Rz and RMS respectively. The increase in roughness is assigned to the thermal degradation of our ZN200-based hybrid polymers, as expected from our TGA analysis. Compared to the uncoated surface, the roughness is much lower with application of ZN200 coatings even after annealing. This is a signature of the fact that ZN200 coatings definitely ensure the planarization of our SS substrates.

Table 4: Surface roughness of uncoated AISI316 SS and ZN200 coated substrates.

	AISI316	Crosslinked ZN200	Annealed ZN200
Ra (nm)	56	8	16
Rz (nm)	500	90	176

The annealing of ZN200 coatings prepared on AISI316 SS substrates is also performed in vacuum and the morphology of resulting samples is examined by SEM (figure 20). One can see that there is no cracking in SEM images and images look as that previously obtained for samples annealed in HNx.

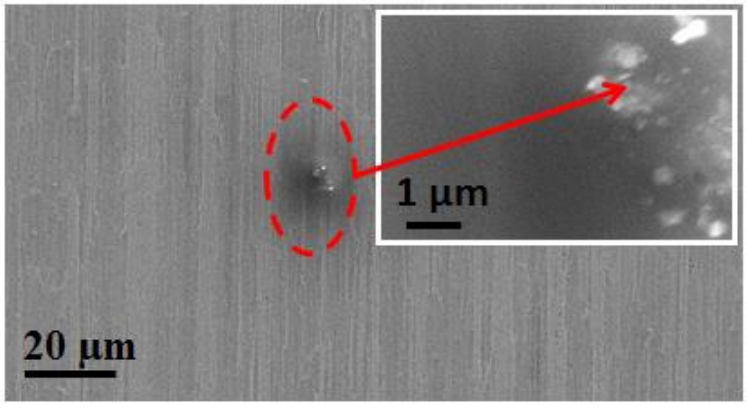

Figure 20: SEM images of ZN200/AISI316 samples annealed up to 550 °C in vacuum.

ZN200 coatings are also tested on AISI430 SS substrates. Figure 21 shows SEM images of crosslinked ZN200 (figure 21.a) and ZN200 coatings annealed up to 550 °C in HNx (figure 21.b) on this type of SS substrate. In both cases, ZN200 coatings are continuous without cracking. Samples visually look smooth and results seem to be similar to that obtained on AISI316.

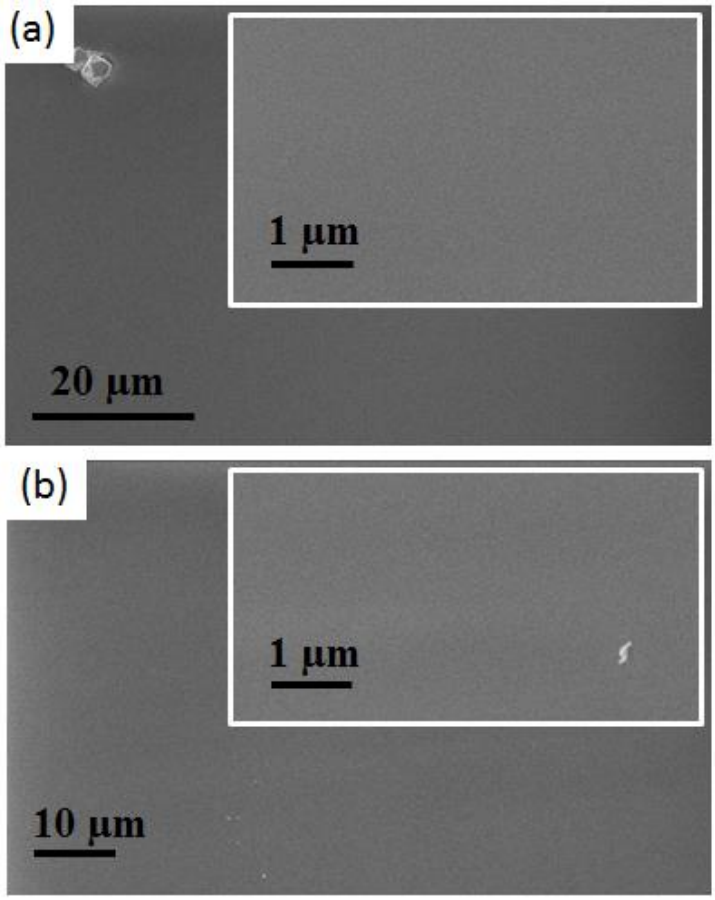

Figure 21: AISI430 SS substrates coated with ZN200 coatings. a) Crosslinked ZN200 coating and b) ZN200 coating annealed up to 550 °C in HN_x.

In contrast to TGA analyses where considerable impacts of temperatures such mass losses and molecules volatilizing are reported, ZN200 coatings seem in view of morphology to resist to effects of temperature. Annealing treatments performed in vacuum and HN_x atmosphere on AISI316 slightly degrade the surface smoothness but coatings remarkably show good resilience to thermal stress. The fact that coatings are also continuous without any cracking after annealing at temperature up to 550 °C in HN_x on AISI430 SS substrates confirms the transferability of our results on this type of steel which is today the better preferred metallic substrate for CIGS community as reported in chapter I.

II.4.1.6. Effects of temperature on crystallinity

XRD analysis are performed on crosslinked ZN200 based coatings and those annealed up to 550°C to evaluate effects of thermal treatments on the crystallinity (figure 22). In accordance with the literature [22,29], the well-defined peaks related to binary (e.g: SiC), ternary (e.g: SiCN) or quaternary (e.g: SiCNO) phases, that should be the crystalline phases for our PZSs coatings, are not detected. Besides, XRD curves obtained for the two types of samples are quite similar. This could be explained by the fact that our ZN200 coatings remain totally amorphous even after annealing up to 550°C.

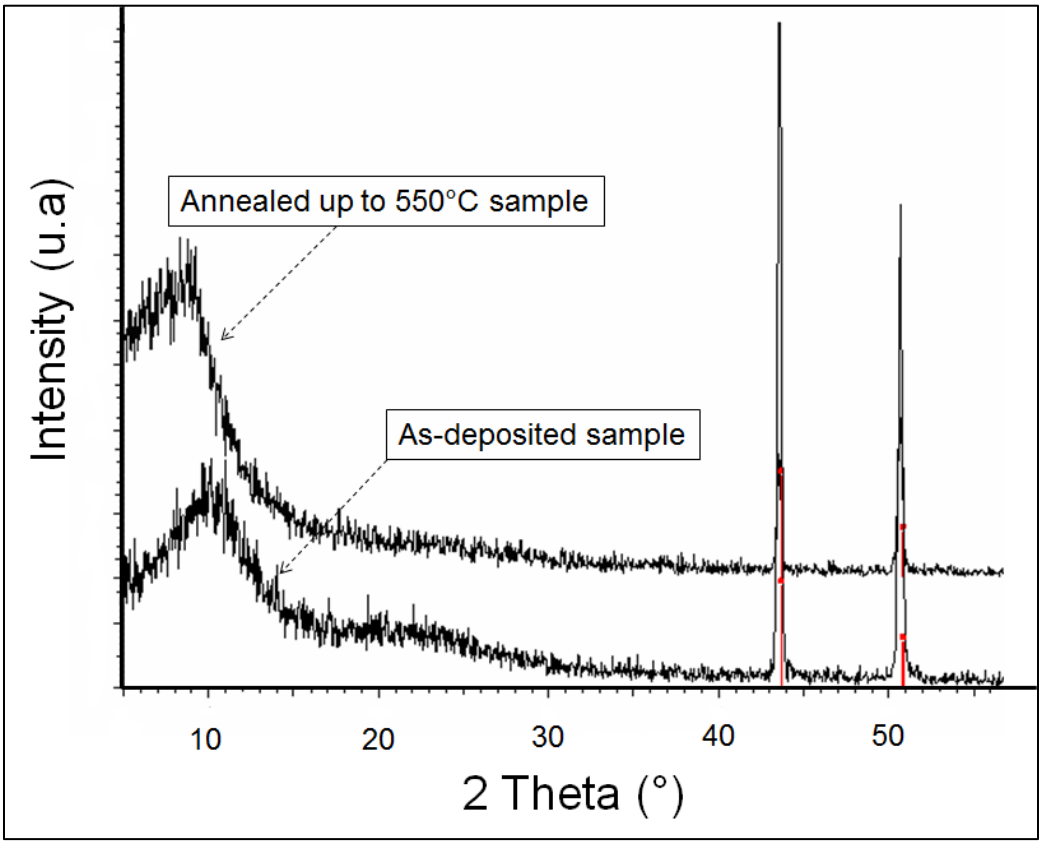

Figure 22: XRD diagrams of as-deposited ZN200 and ZN200 coatings annealed up to 550°C in N_2: 5% H_2. Coatings are deposited on AISI316 substrates.

For most PSZs coating and for all PCDs based precursors converted into ceramics, it was widely reported that the crystallization starts at temperature above 1400°C [22,16]. The two well-defined peaks at 43° and 51° should correspond respectively to (111) and (200) diffraction planes, and are signatures of peaks for AISI316 SS used here as substrate [30]. The large peaks detected in diffraction angles covering 5° to 15° are for ZN200 coatings, they are tentatively

assigned to a short scale organization of a fraction of crystalline phases in the coating even if a significant amount of carbon atoms in the polymer can hinder the crystallization of ceramic phases over the tested temperature range [31].

II.4.2. Electrical properties of ZN200 based DBLs

This section deals with dielectric properties of ZN200 coatings with respect to requirements of DBL for CIGS solar cells. They were characterized in DC mode for leakage current and dielectric strength measurements, and in AC mode for impedance spectroscopy.

II.4.2.1. Electrical characterization in DC mode

- ***Concepts***

The back side of CIGS solar cells monolithically fabricated and interconnected on steel substrates is typically made of steel/dielectric-layer/molybdenum. The structure of such system can be described as a parallel plate capacitor. The most important conduction or leakage current mechanisms in MIMs are already described in [32,33,34], where it was demonstrated that the formalism of such mechanisms can be most of time fitted with E^n $(n \leq 1)$ models. As an example, Allers et al. [35] investigated silicon-nitride based MIM capacitors and found that the field dependence of leakage current in dielectrics goes as $\sqrt{E}$, obeying the Poole-Frenkel conduction mechanism. The voltage acceleration factor, the activation energy and constant dielectric have been evaluated for such SiN coatings within the frame of $\sqrt{E}$ models. The $\sqrt{E}$ model is also reported for tantalum pentoxide dielectric in [36]. McPherson et al. [37] in their investigations found that when SiO_2 is stored under constant electric field it will breakdown with time and suggested that the time to failure (t_{bd}) of this type of oxide strongly depends on both the electric field and temperature. They conclude that t_{bd} can obey two main models: $E-$ model and $1/E-$ model. Otherwise, Fowler-Nordheim conduction mechanism has currently been found for Si-SiO_2-Al based MIM capacitors [38,39]. All these investigations reveal the fact that there is no universal conduction model for solid dielectrics and that conduction mechanisms strongly depend on the nature and geometry of the dielectric material [5]. These concepts will be used in the following section to investigate electrical properties of our insulating coatings.

II.4.2.1.1. Leakage current

Electric field and temperature dependence of the inter-metal dielectric in the back-side of CIGS solar cells prepared on metal substrates become a serious concern especially when PSZ materials such as ZN200 coatings [15] are used because these materials can be electrically weaker and break faster. Another difficulty met with ZN200 coatings concerns the dielectric quality of

coatings over large areas. Besides, the use of commercial substrates and industrial deposition method such as the bar-coating process which inherently entails several contaminations makes impurities control more complex.

Effects of such impurities in our DBLs are evaluated through measurement of leakage current using pads matrix. Pads matrix on large area can also allow to investigate the impact of defects on IMDs statistically. The testing structure developed for our insulating DBL characterization is displayed in figure 23. The system offers a possibility to make seventeen MIM capacitors simultaneously on the top of dielectric stacks of total area of 100 mm × 100 mm, using a mask system. Two different Mo pads of 10 mm² and 2500 mm² areas are deposited on each sample in order to take into account effects of defects distribution in lateral dimensions.

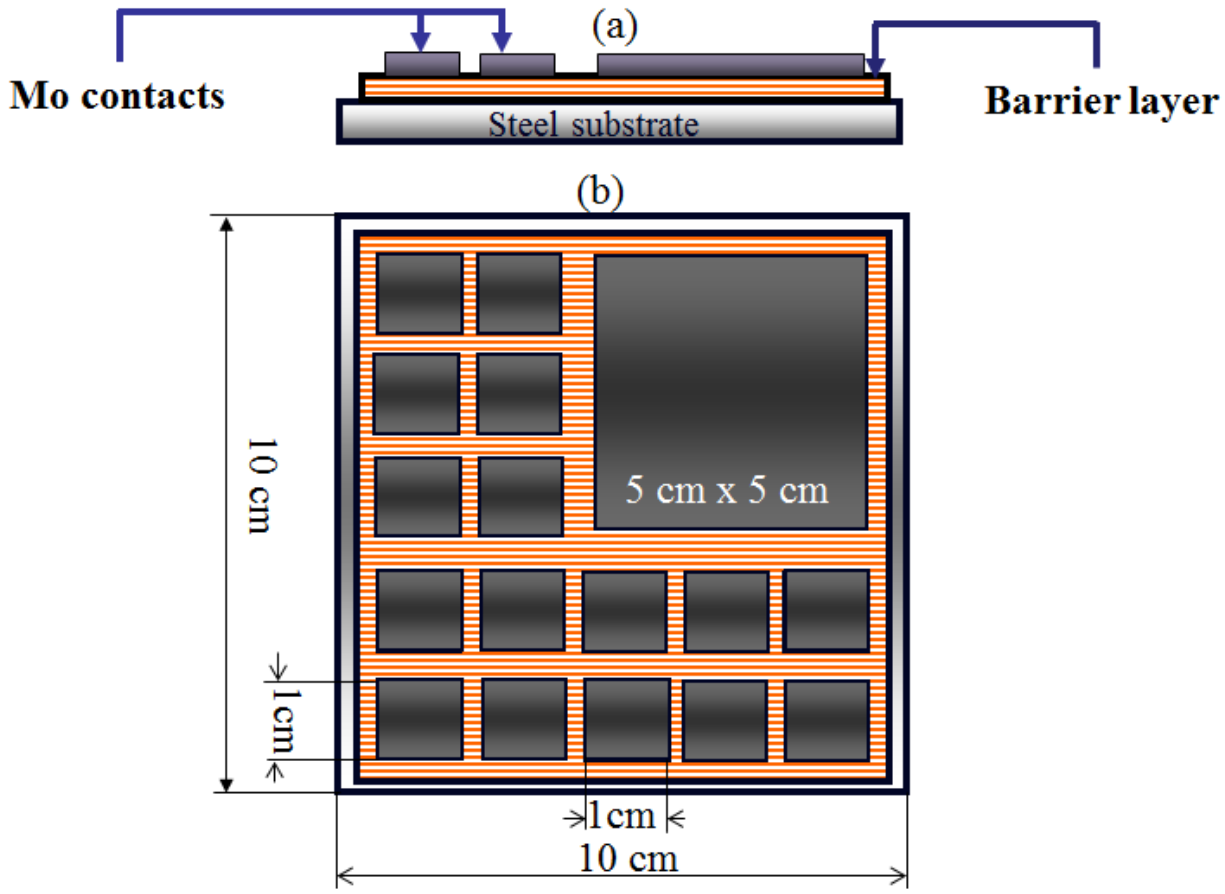

Figure 23: Diagram of matrix of MIM capacitors designed for DC mode electrical measurements: a) front view and b) top view.

For the first evaluation of dielectric quality of our insulating DBL, 5 V bias is systematically applied to each pad and the leakage is then measured; two samples are analyzed for each kind of MIM. The maximum acceptable DC leakage current for MIM capacitors is fixed at 10^{-6} A/cm², which corresponds to 0.1 % of current during normal PV operation. Above this limit, the MIM capacitor is rejected. To compare our DBLs, a yield is defined as ratio between the number of valid MIM capacitors over the total number of tested MIM capacitors:

$$Yield = \frac{Number\ of\ valid\ MIM\ capacitors}{Total\ number\ of\ tested\ MIM\ capacitors} \qquad \text{II.1}$$

A set of MIM based on a single ZN200 layer has been made first; they all presented a leakage current exceeding 10^{-6} A/cm². Therefore we choose to study, ZN200 double layers based MIMs. Plots of leakage current at 5 V bias as a function of top electrodes (pads) for representative samples using a stack of ZN200 double layer are shown in figure 24.a and b. Results obtained with crosslinked ZN200 double layers are shown in figure 24.a and it can be observed that a yield of around 94 % has been reached. As can be seen in figure 24.b where coatings are annealed at 550 °C in HN_x atmosphere, the leakage current dramatically increases and consequently, the number of non-valid MIM capacitors remarkably increased. Therefore, the yield is reduced from 94 % to 52 % indicating in view of dielectric aspects that the annealing up to 550 °C strongly degraded our DBLs. This result could be convenient with gasses evolution previously observed in TGA and ATR analyses since gases formation can lead to a creation of pinholes or pores [40]. If open pores are created, it can be a source of percolation pathways in coatings; the closed pores in turn could be filled by gases and both types of pores should weaken the dielectric strength. Another source of increase in leakage current could be the local thinning caused by either asperities or high surface roughness [41] of the substrate used.

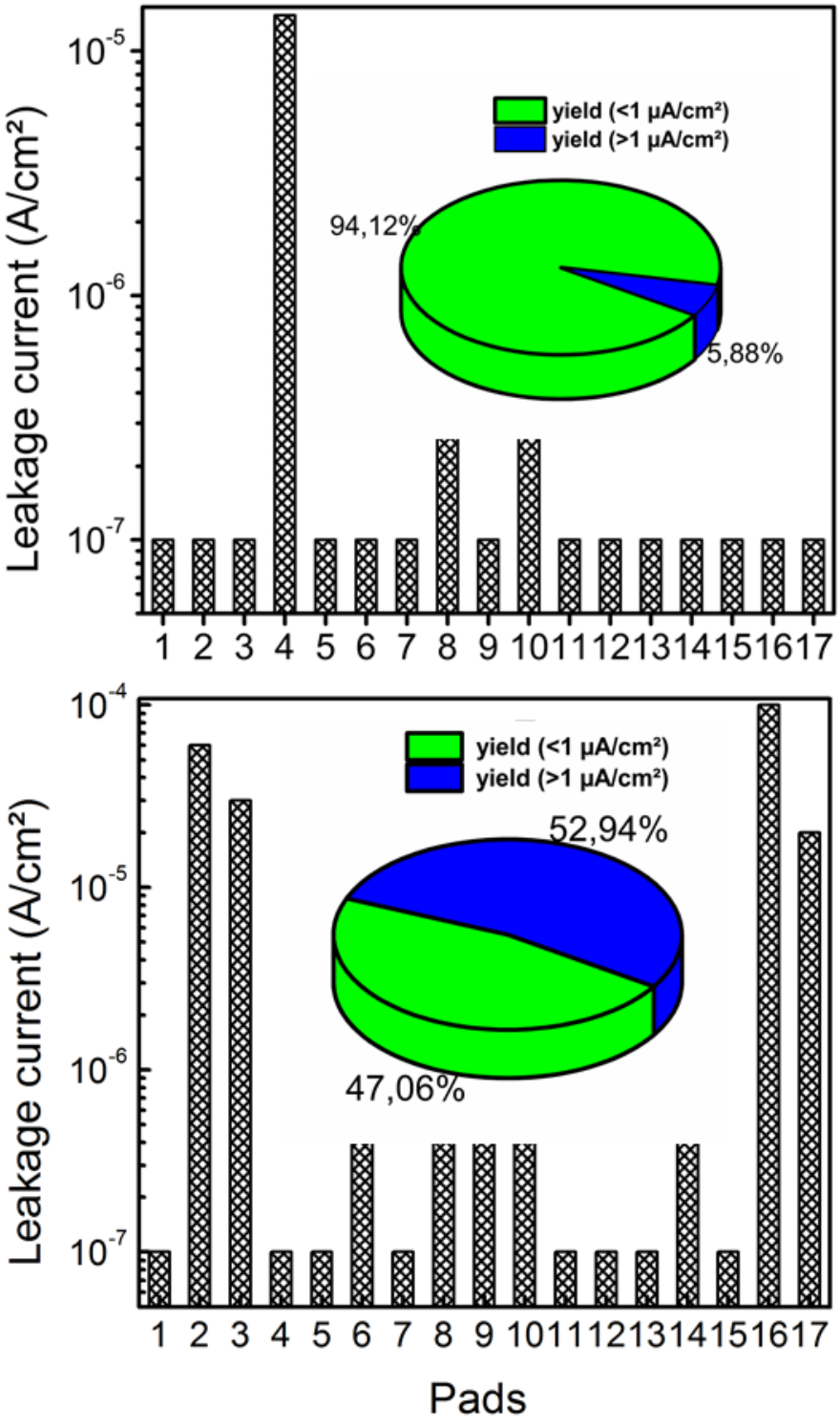

Figure 24: Leakage current of MIM capacitors prepared with (a) crosslinked ZN200 double layer; (b) ZN200 coatings crosslinked coatings and annealed up to 550 °C in HNx atmosphere. Numbers 1 to 16 correspond to pads of 1 cm² and 17 is a pad of 25 cm².

An increase in leakage current could also arise from a reduction in thickness of ZN200 coating after annealing. Dusts and several others contaminants are always present in ambient air and should be revealed strongly detrimental for our coatings since coatings are currently deposited in ambient atmosphere (i.e., without control of dust level); some coatings are prepared in cleanroom for comparison purposes. In table 5, we summarize the yields of crosslinked ZN200 (double layers) based MIMs capacitors deposited with spin coating process (1500 rpm, 60 s) in ambient atmosphere and cleanroom. A significant difference has been observed between both types of coatings since a yield of 67 % has been obtained with coatings performed in ambient atmosphere while a yield of more or less 97 % is reached in cleanroom. This confirms the fact that the control of air pollution can greatly contribute to the improvement of quality of our coatings. The impacts of defects distribution of these coatings has been also checked by comparing MIM capacitors with different sizes. It is observed that the level of yield decreases with area of MIM capacitors. MIMs with diameter lower than 2 mm are remarkably good with a yield of 100 % reached even for coatings deposited in air. Once again, the maximum level of leakage current is often exceeded with the largest MIM capacitors (50 mm × 50 mm), this results from the fact that the probability to find defects in dielectric material increases with area. These results are in good agreement with those reported in the literature [42].

Table 5: Comparison of leakage currents for ZN200 based DBL deposited in cleanroom and these deposited in ambient air.

		Air ambient	Cleanroom
Diameter of Mo pads	Number of MIM	Yield (%)	Yield (%)
10 mm	36	67	97
2 mm	8	100	100
1 mm	8	100	100

To reduce local thinning and pinholes effects on our ZN200 coatings, methods have been devised to increase the number of multilayers in order first to increase the probability to obstruct holes and second to increase the thickness. Several possibilities have been tested. First, a third layer of ZN200 has been added on ZN200 double layers (either crosslinked layer or thermally stabilized layers) but the deposition systematically failed due to a problem of covering. The third layer forms puddles during the step of crosslinking. Another series of insulating stacks we tested is a ZN200 double layer completed with 400-600 nm-thick of $SiAl_xO_y$. MIMs performed with these stacks did not show any change compared to the basic stack in ZN200 double layers. Thus, the later stacks are stabilized ZN200 double layers completed with $SiAl_xO_y$ layer on which an additional layer of ZN200 has been deposited as illustrated in figure 25. ZN200 additional layer covered and adhered well to the SiAlxOy plasma coating which in turn adhered well to the stabilized ZN200 double layer and the final stack can be considered as a single solid unit. This kind of stack involving a reinforced ZN200 layer is called combi-layer.

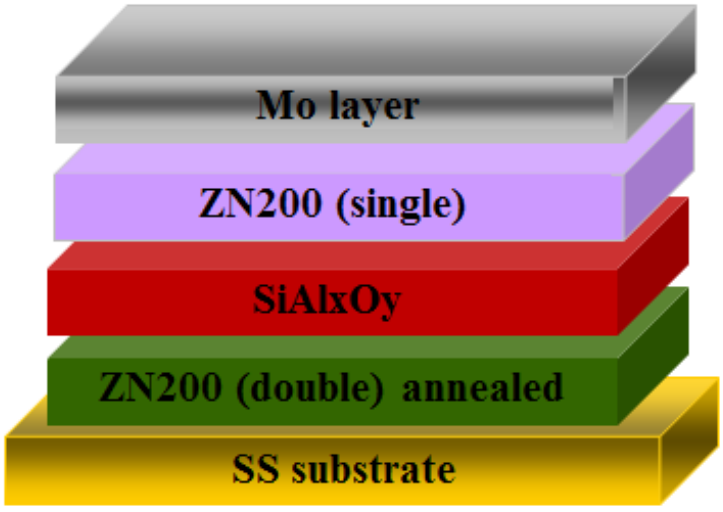

Figure 25: Structure of the combi-layers.

MIMs are then performed with combi-layers prepared in air and their dielectric capabilities have been tested. Figure 26 shows a typical result of leakage current with 5 V applied voltage for representative samples of such combi-layers. A yield of 100 % has been reached; this is a

signature of good electrical insulation and hence makes these stacks our favorite solution for CIGS solar integration on steel substrates.

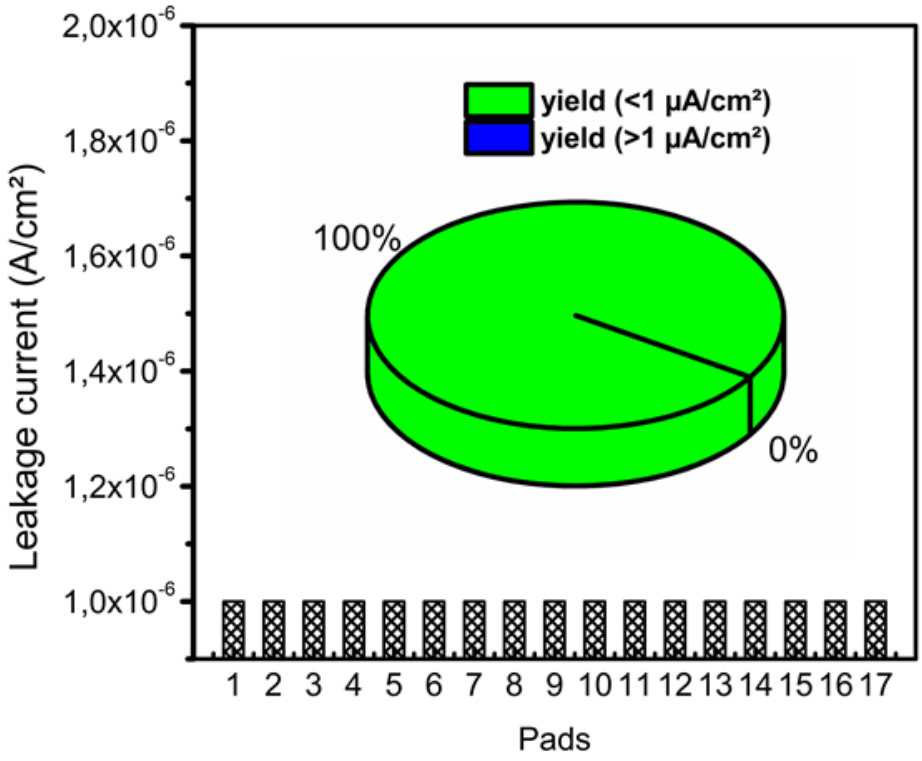

Figure 26: Leakage current of MIM capacitors prepared with combi-layer. Numbers 1 to 16 correspond to pads of 1 cm² and 17 is a pad of 25 cm².

Thus, intensive investigations will be performed in the following sections on these kinds of stacks for further understanding of their dielectric properties.

II.4.2.1.2. Dielectric reliability

II.4.2.1.2.1. Transient current and dielectric strength

Investigations have been carried out to measure the density of leakage current as a function of time by applying a constant voltage stress (CVS) on the combi-layer based MIM capacitors. The leakage current was measured each 0.5 s. Typical results for the non-annealed combi-layer (D1) based MIMs at different voltage ramp rate are shown in figure 27. At each applied voltage, the transient current behavior is clearly seen [43].

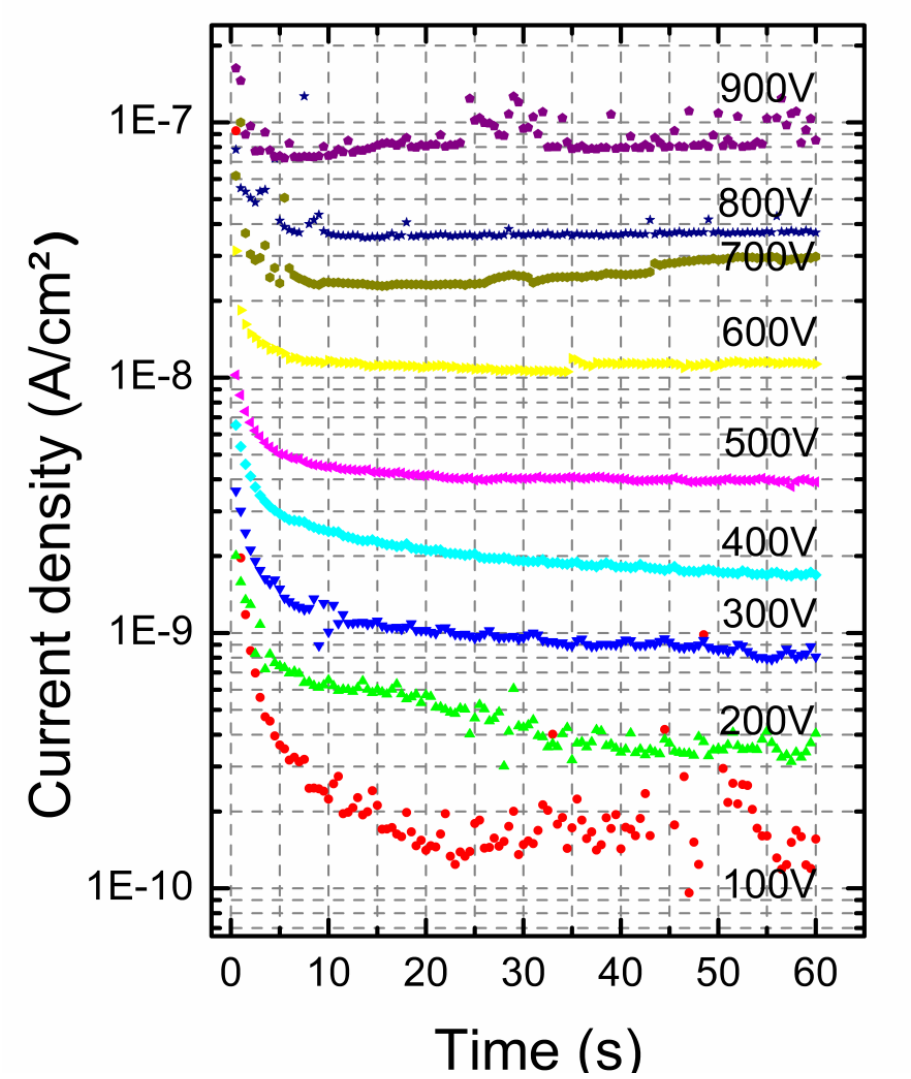

Figure 27: I-t plots for constant voltage stress experiment on non-annealed combi –layer (D1).

The common feature of all current vs. time curves is that the leakage current is higher for the first ten seconds before becoming quite constant. This is the signature of polarization effect in our ZN200 based MIMs. The initial decrease of current indicates the fact that during the constant voltage stressing, some charge carriers which are forced through the dielectric are trapped causing the reduction of electric field across the dielectric [35]. It can also be observed that the current density increases with the intensity of the applied voltage. From 100 V to 900 V, it can be seen that the current density is increased from 5×10^{-9} A/cm² to 8×10^{-7} A/cm². The current increasing with the voltage is a signature of the electric field dependence of leakage current.

CVS measurements have been also performed on combi-layers annealed up to 500°C (D2) and results are shown in figure 28. Compared to non-annealed combi-layers, a similar behavior has been observed in I *vs* t curves, with current levels slightly higher compared to non-annealed samples at similar voltages.

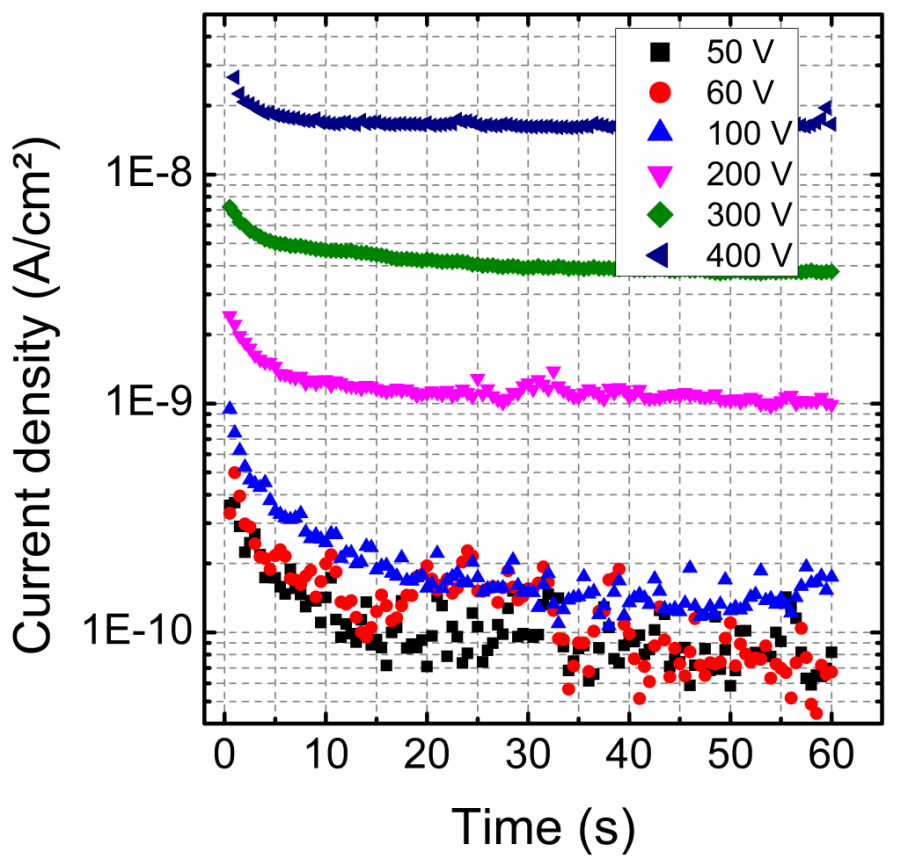

Figure 28: I-t plots for constant voltage stress experiments on D2 combi-layers (D1 annealed at 500 °C).

Furthermore, the time to breakdown of CVS measurements has been recorded and data are plotted in figure 29. Results suggest that the breakdown of our dielectric appears once a certain amount of charge has been forced through the dielectric. As average thicknesses of (D1) and (D2) are respectively 4.4 µm and 3.7 µm, it was then found that non-annealed and annealed combi-layers exhibit disruptive fields of 2.27 MV/cm (maximum voltage: 1000V) and 1.32 MV/cm (maximum voltage: 500V) respectively. The time to breakdown is quite similar (~ 30 s) for both samples while the applied voltage is 40 % higher in case of D1. At the same time, the reduction in thickness after annealing up to 500 °C is found to be 16 % lower. This means that

conduction in our annealed coatings should be strongly electric field dependent. Values of dielectric strengths found here for our DBL coating are better than these recently reported on dielectric materials commonly used for the fabrication of CIGS solar cells on metals. As an example, the disruptive field of our combi-layer is more or less four times higher than the disruptive field reported for MIM capacitors made with SiO_2 in [2].

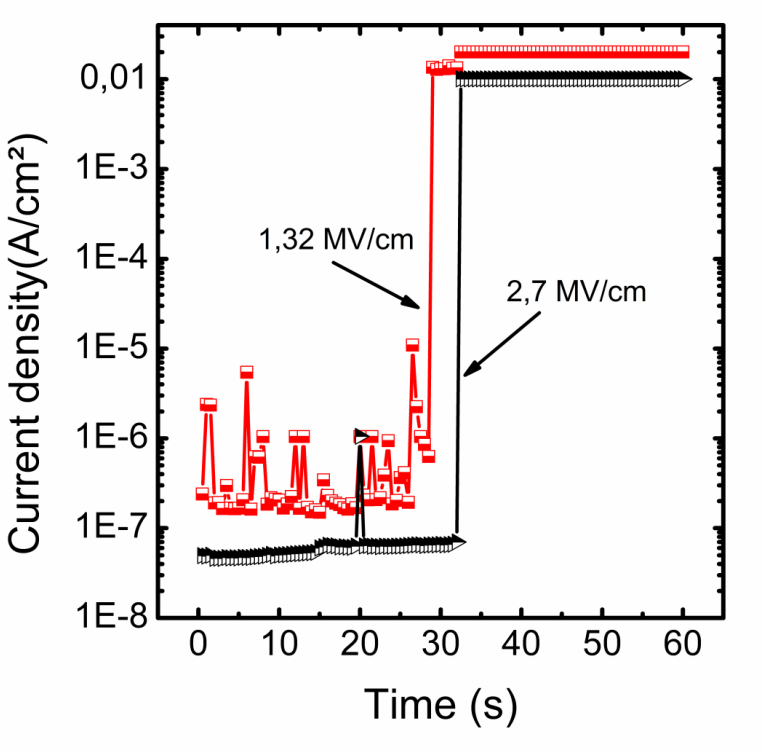

Figure 29: Time to breakdown characteristics at 2.7 MV/cm for D1 (in black colour) and 1.32 MV/cm for D2 (in red colour).

Otherwise, impacts of breakdown voltage on our MIM structure are shown in figure 30. It is clearly found that the final breakdown leaves several craters visible on tested MIM. This is a signature of the explosion of the dielectric material and is a consequence of dissipation of energy which is cumulatively stored in MIM structure [44]. The breakdown can occur almost instantaneously for very high field. Before the ultimate degradation of our MIMs, electrical arcs are often observed and the degradation is usually initiated at several points as can be checked in figure 30.

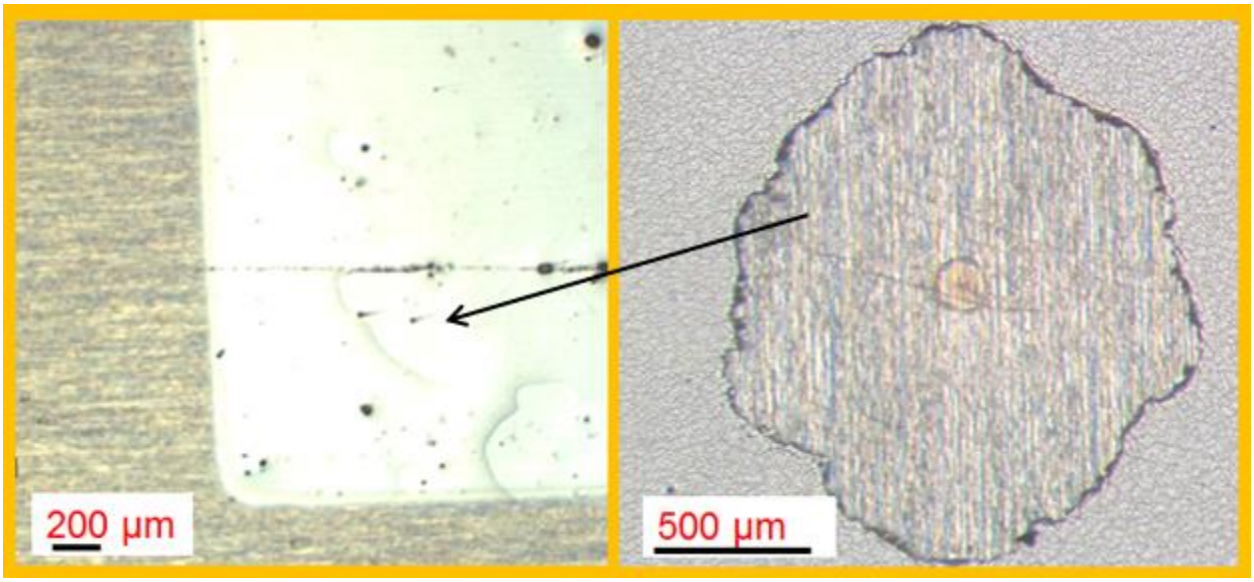

Figure 30: Photograph of electric field impacts on MIM capacitors after breakdown. The final breakdown leaves a crater.

With respect to the limit of leakage current fixed in previous section, the maximum acceptable electrical fields are therefore 2.7 and 1.3 MV/cm respectively for D1 and D2. The total thickness of combi-layers is reduced of around 16 % after annealing while the dielectric strength is approximately decreased by 50 %. One should normally expect a similarity between the decrease in thickness and the increase in leakage current if the thickness of coating is the unique parameter which impacts the conduction in dielectric. Thus, it can be deduced that the contribution in increase of leakage current due to thermal degradation is probably higher than that arising from reduction in thickness everything equal elsewhere. The change in dielectric strength confirms otherwise evolution of the chemical state suggested in our thermal analyses.

Nevertheless, the contribution in increase of current level could rise from local thinning of dielectric and should not be neglected. Indeed, data extracted from SEM cross section images for non-annealed combi-layer shown in figure 31 clearly show an important non-uniformity in thickness. The difference between the highest and the lowest thickness found is remarkably high; it can be as high as 630 nm at some place. As a consequence, a significant increase in leakage current increase may occur.

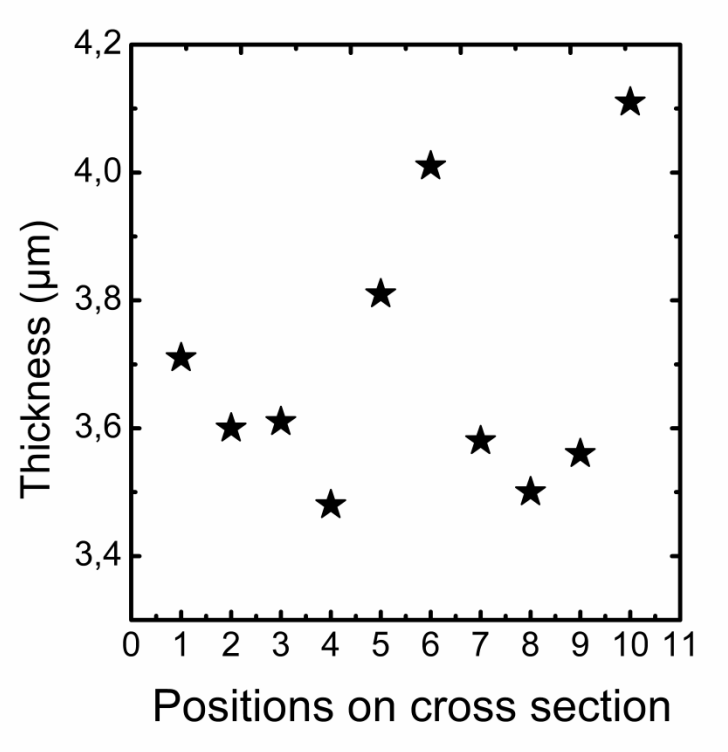

Figure 31: Distribution of thickness of D1 in the cross section.

All these results reveal that the developed combi-layer present good electrical strength for being used as insulating DBL for integration of CIGS solar cells on steel substrates. However, investigations on dielectric properties have been extended for further understanding of combi-layers even if straightforward aspects related to dielectric strength and leakage current previously presented could be basic parameters required for qualification of dielectric materials for solar cells. Especially, ageing tests and defects monitoring should be crucial for dielectric engineering and investigations in the following part of the dielectric section could be seen as preliminary studies of our combi-layers for these concerns.

II.4.2.1.2.2. Conduction mechanisms

To detail the appropriate conduction in our MIM capacitors, a set of CVS have been done. Figure 32 shows an example of $I-t$ characteristics recorded at 2.3 × 10^{-3} MV /cm, 6.7 × 10^{-3} MV /cm, 11.5 × 10^{-3} MV /cm, and 23 × 10^{-3} MV /cm for MIM capacitors fabricated with the non-annealed combi-layer. The level of detected current clearly correspond to the noise for all applied electric field and indicates that charges injection effects can be neglected up to 23 × 10^{-3} MV /cm (10 V).

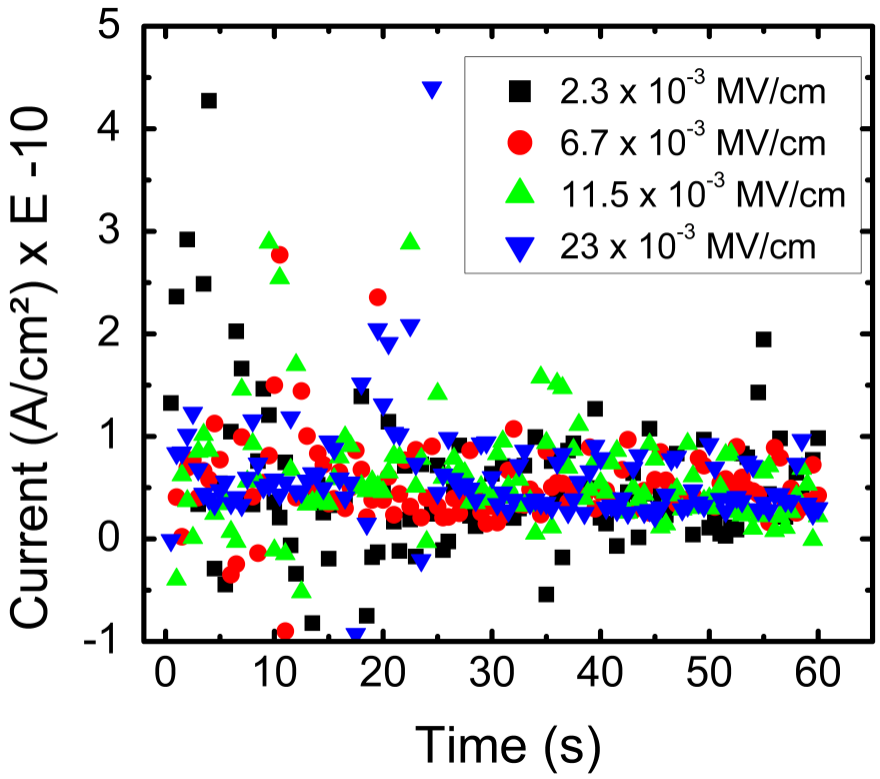

Figure 32: *I-t* characteristics under different applied electric field for non-annealed combi-layer based MIM capacitor.

To investigate conduction mechanisms in our MIMs better, CVS at higher voltages (50 V to 900 V) have been then considered. Generally, at high applied voltage, sufficient charges can be injected into the dielectric (or ejected), thereby their effects should be observable in absorption or desorption currents. Therefore, straightforward profiles of the measured transient current can be used to determine the type of conduction in a solid dielectric. Cupta et al. [45] and Joncher et al [46] demonstrated with help of transient currents profiles that several dielectric materials obey the empirical law introduced by Curie and von Schweidler in [47]:

$$J \sim t^{-n} \quad (n < 1) \qquad \text{II.2}$$

where the value of the exponent n can be used to identify the type of conduction mechanism in the tested dielectrics [48].

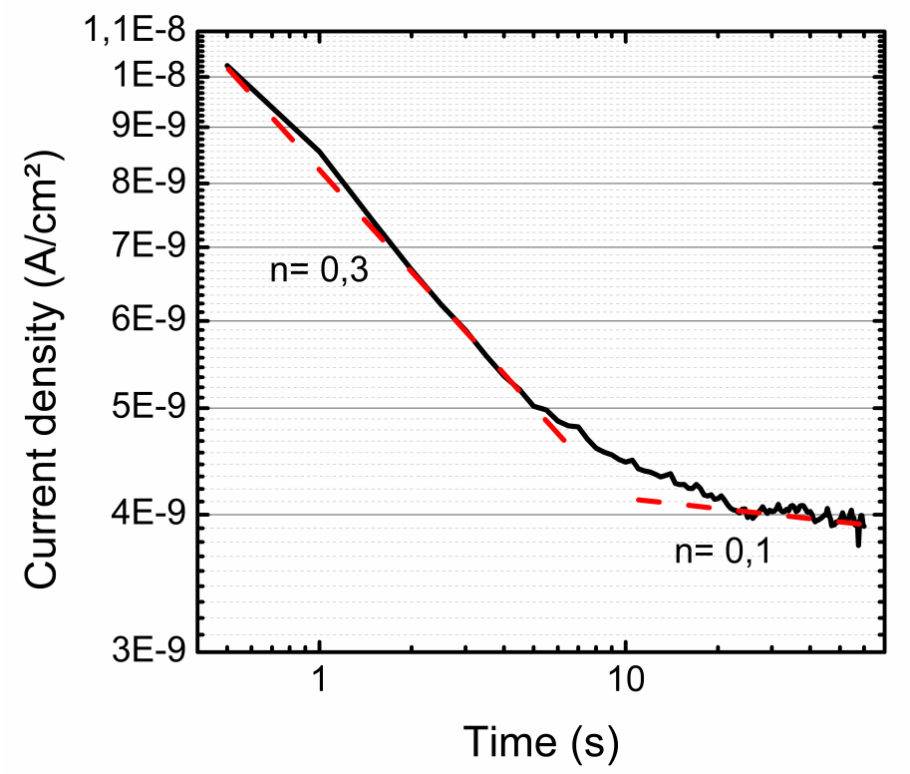

Figure 33: Time dependence of absorption current at 400V for D1 based MIM capacitors.

To test this, the characteristic of $Log(J) - Log(t)$ at the applied voltage of 400 V (arbitrarily chosen) is given in figure 33 as an example and the corresponding values of power factor n are summarized in table 6. Two main zones can be observed:

- for times lower than 10 s (zone 1), the power factor is approximately of 0.3.
- in zone 2 corresponding to times upper than 10 s, the value of power factor is relatively low and is around of 0.1.

Table 6: Variation of power factor, n as function of time.

Zone	Times	Power factor, n
1	< 10 s	~ 0.3
2	> 10 s	~ 0.1

According to the literature [49], the fact that values of n are comprised between 0 and 1 cannot help to distinguish between different probable polarization modes [50]. Thus, attention should be focused on the detailed exploitation of $I-V$ characteristics to evaluate the appropriated conduction mechanism in our combi-layers accurately.

To participate to conduction, charge carriers should be injected (or ejected) from the Fermi level (E_F) of the contact-electrode (interface) into the conducting band (E_C) of the dielectric material [51]. In the presence of an applied electric field, charges injected from interface gain energy additionally to the thermal energy. As a consequence, the barrier height is lowered and more charges can be injected into the conduction band of the host dielectric through mechanisms of thermionic emission (Schottky effect), tunneling emission (Fowler-Nordheim emission) or thermally enhanced tunneling emission. Such mechanisms are illustrated in figure 32.

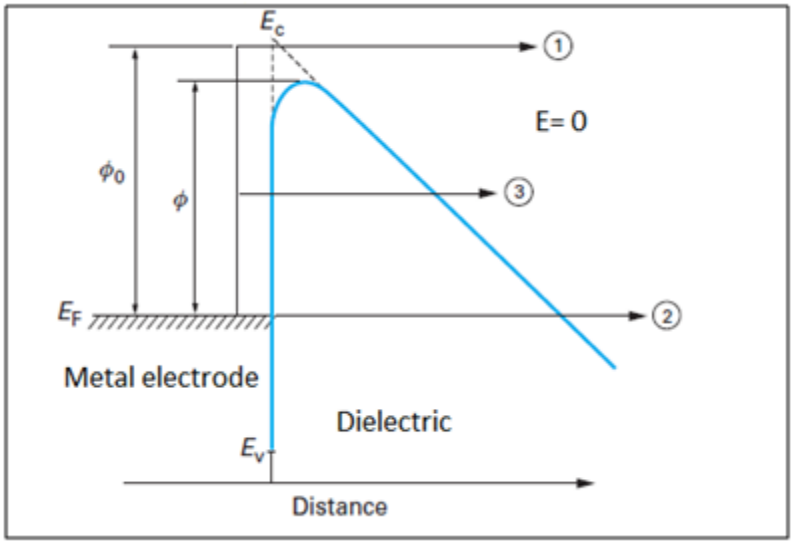

Figure 34: Diagrams band at interface between dielectric and metal, (1) Schottky effect, (2) Fowler-Nordheim and (3) thermally enhanced tunneling emission.

Bulk limited current conduction mechanisms through insulator are also commonly found in MIMs and are mainly known as Poole-Frenkel (P-F) emission and Space Charge Limited Current (SCLC).

Based on our results, only Schottky or P-F effects could be present in our MIMs (see detail below).

Schottky or thermionic emission theory assumes that charge carriers with energy higher than the barrier energy can cross the barrier and enter conduction band; then, it ensures the conduction. The characteristic of the resulting current density J at a given applied field E can be described by the following equation:

$$J = AT^2 exp\left(-\frac{\emptyset_0 - \beta_s\sqrt{E}}{k_B T}\right) \qquad \text{II.2}$$

where A is called the Richardson-Dushman constant, k_B is the Boltzmann constant and T is the absolute temperature. $\emptyset_0$ is the barrier height of the injecting electrode when no electric field is applied and β_s is the Schottky constant given by:

$$\beta_s = \sqrt{\frac{q^3}{4\pi\varepsilon_0\varepsilon_r}} \qquad \text{II.3}$$

Semilogarithmic plots of $\log(J)$ versus $E^{1/2}$ yield a straight line, from the slope of which the permittivity of the insulator can be calculated using equation II.3.

The classical Poole-Frenkel (P-F) effect is the thermal emission of charge carriers from Coulombic (i.e., charged) traps in the bulk of dielectric materials enhanced by application of an electric field [52,53]. The P-F mechanism is driven by electric field which reduces the barrier height on one side of the trap, thereby increases the probability of electron escaping from the trap. It is illustrated in figure 12 where a Coulombic potential well is shown in the presence of an electric field. $q\emptyset$ is the ionization potential, which is the amount of energy required for the trapped electron to escape the trapping center when no electrical field is applied. As the field increases, the potential barrier decreases by $\beta_{PF}\sqrt{E}$ on the trap, making it easier for the electron to vacate the trap and enter the conduction band of the dielectric.

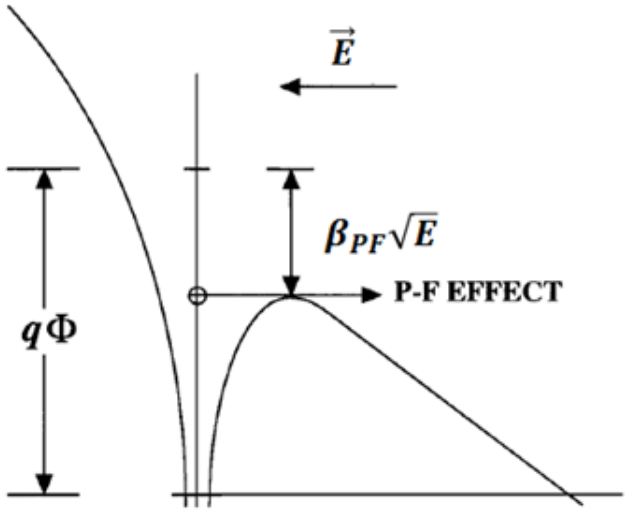

Figure 35: Illustration of Poole-Frenkel effect taken from [54].

In the P-F model, the reduction of barrier height is expressed by:

$$\Delta\emptyset = \emptyset_0 - \emptyset = \beta_{PF}\sqrt{E} \qquad \text{II.4}$$

With

$$\beta_{PF} = \sqrt{\frac{q^3}{\pi\varepsilon_0\varepsilon_r}} = 2\beta_s \qquad \text{II.5}$$

where β_{PF} is known as the Pool-Frenkel constant. The current density is given by the following equation:

$$J = J_0 exp\left[-\frac{\emptyset_0 - \beta_{PF}\sqrt{E}}{k_B T}\right] \qquad \text{II.6}$$

The analytical expression of the P-F model is virtually identical to the one of Schottky emission. However, in the case of Schottky emission the number of trap potential wells is larger by the factor 2. This is because the barrier height reduction is twice larger due to the immobility of the positive charge carriers [55].

$I-V$ characteristics (figures 36 and 37) for both D1 and D2 based MIM capacitors are processed using data extracted from $I-t$ curves of figures 27 and 28. For each applied voltage, values of current recorded at three different ramp rates are considered. Several $I-$

V representations such $log(J)$ vs. E or $log(J)$ vs. $1/E$ etc. have been explored but only the representation of log(J) vs. $E^{1/2}$ is consistent with E^n models. Thus, one can exclude Fowler-Nordheim (F-N) [38] and Space-Charge-Limited (SCL) models [33]. $E^{1/2}$ models however may result from either Schottky emission (interface limiting based model) or Poole-Frenkel (P-F) emission (volume limiting based model) and both can be present in our MIM capacitors [56].

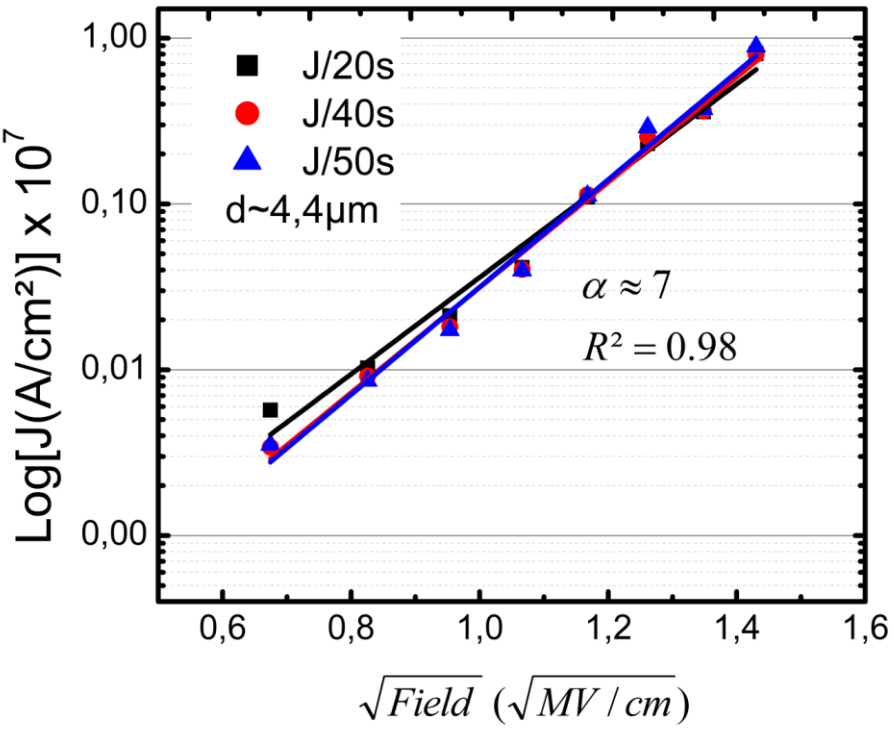

Figure 36: Typical *I-V* characteristic for D1, non-annealed combi-layer based MIM capacitors.

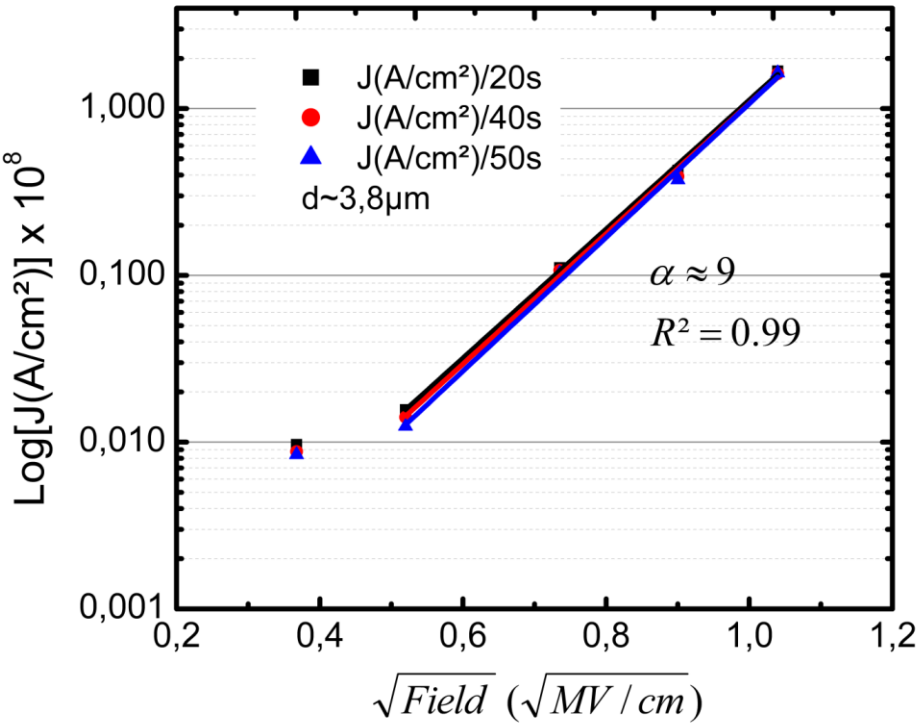

Figure 37: Typical *I-V* characteristic of D2, combi-layer annealed up to 500 °C based MIM capacitors.

According to P-F or Schottky equations, a plot of $log(J)$ versus $E^{1/2}$ should be a straight line and the dielectric constant can be determined by the slope (α) of the curve. It can be checked that the value of the slope depends on the temperature but is assumed constant here since our tests are performed at room temperature. The level of leakage current should be independent from the ramp rate.

Figure 36 shows a representative $I-V$ curves for non-annealed combi-layer. It can be observed from $log(J)-E^{1/2}$ curves that the current is increasing with the applied electric field. This is in agreement with expected models. The fact that graphs with different ramp rate are well superposed is the signature of a saturation due to trapping in the coating [57]. The same type of plotting is recorded for annealed combi-layer based MIM capacitors and is shown in figure 37. Linear lines are also observed and graphs at different ramp rates for annealed combi-layer based capacitors are again well superposed. A slight shift observed at very low applied field (E) in this

case can be tentatively assigned to space charge effect near surface of electrodes and is in line with [56].

However, to determine the appropriate conduction for our coatings, values of dielectric constants have to be calculated and compared using both Schottky and P-F models. Measured slopes for non-annealed and the annealed combi-layers are 7.8×10^4 and 9.5×10^4 respectively. Dielectric constants are calculated from equations II.3 and II.4:

− For Schottky model $$\varepsilon_S = \frac{q^3}{4\pi\varepsilon_0[KT\alpha]^2} \quad \text{with } \varepsilon_S = n^2 \qquad \text{II.3}$$

where n is the index of refraction and,

−For Poole Frenkel model $$\varepsilon_{P-F} = \frac{q^3}{\pi\varepsilon_0[KT\alpha]^2} \qquad \text{II.4}$$

Table 7: Dielectric constants calculated from Poole-Frenkel and Schottky models.

Comi-layer	Calculated dielectric constant, ε (F.m^{-1})	
	Poole-Frenkel	Schottky
Non-annealed	14.4	3.7
Annealed up to 500 °C	11.2	2.8

Table 7 summarizes the calculated dielectric constant values. To our knowledge, there is no dielectric reliability study based on dielectric systems we tested in this thesis to point out a comparison. Thus, to identify the appropriate conduction mechanism, we have to compare constant dielectric values found here with data reported in the literature for dielectric materials more or less close to our combi-layer. Our dielectric systems are composed of polysilazane multilayer with composition close to Si-N-O-C quaternary PDCs combined with $SiAl_xO_y$

coatings. Our dielectric may then respond to electrical field as composite materials. The Maxwell-Wagner-Sillar model [58,59] is commonly used to describe polarization processes in inhomogeneous materials. By using a system composed of spherical particles (with ε_2 dielectric constant) embedded in a homogenous medium (with ε_1 dielectric constant), they found an approximate equivalent dielectric constant:

$$\varepsilon_q = \varepsilon_1 \times \frac{(2\varepsilon_1 + \varepsilon_2) - 2\rho(\varepsilon_1 - \varepsilon_2)}{(2\varepsilon_1 + \varepsilon_2) + 2\rho(\varepsilon_1 - \varepsilon_2)} \qquad \text{II.5}$$

where ρ is equal to volume fraction of embedded particles.

It can be seen that the equivalent dielectric constant of composite is definitely lower than that of the matrix. To extrapolate this approach to our systems, one can then consider that the dielectric constant of our coatings should be comprised between that of SiO_2 and PZS. Wang et al. [15] reported a dielectric constant value of 2.2 on porous polysilazane coatings while the well-known SiO_2 has permittivity of 3.9 [35]. In the P-F model, the calculated dielectric constant is 3.5 times higher than the maximum expected for non-annealed combi-layer while it more or less three times higher in the case of the annealed one. Considering the Schottky model, values of dielectric constants in both cases are comprised between those of SiO_2 and PZS coatings. Then, we conclude that the Schottky conduction mechanism should behe most limiting conduction mechanism in our coatings.

II.4.2.2. Electrical characterization in AC mode

The complex impedance Z^* of our ZN200 double layer prepared in cleanroom using spin coating deposition method was obtained using:

$$Z^* = {}^{V}/_{I} \qquad \text{II.6}$$

Where V and I are the applied voltage and the resulting current respectively.

In figure 38.a and b are respectively represent the frequency dependence of the imaginary ($\mathbf{Z''}$) and real ($\mathbf{Z'}$) parts of the impedance at different bias voltages in a log-log representation. For voltages higher than 2 V and low frequencies (lower than 10^3 Hz), a constant resistivity of around $\mathbf{10^{-6}\ \Omega}$ has been observed. Another plateau seems to be observed for higher frequencies. For voltages lower than 2 V, the plateau is probably high enough to be detected by the used

LCR. For all voltages, evolution of reactance is line segments which become constant at the higher frequencies (higher than $\mathbf{10^{+6}}$ Hz).

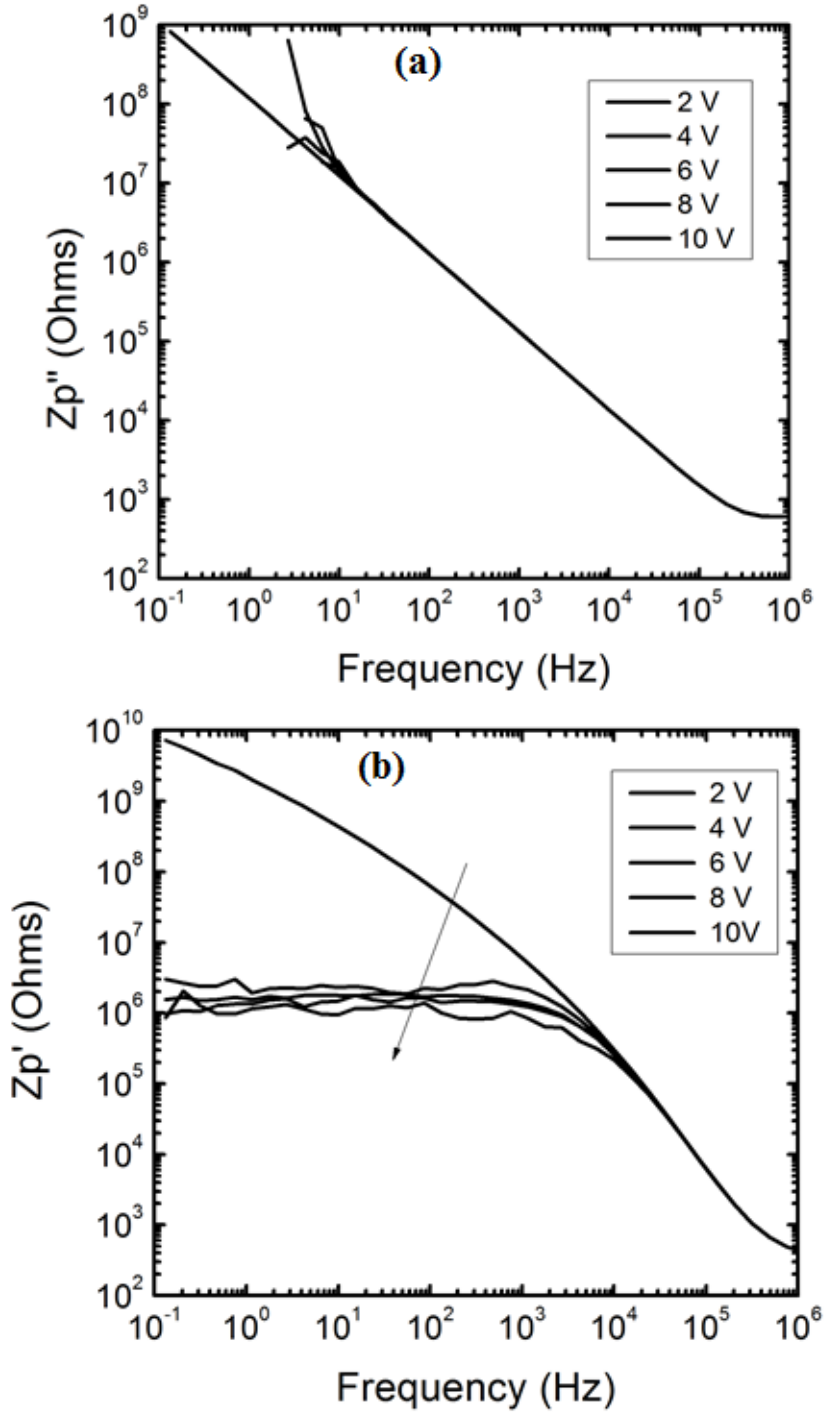

Figure 38: Frequency dependency of (a) imaginary (Zp″) and (a) real (Zp') parts of impedance.

Normally, experiments are carried out at different voltages in order to detected peak-shifts in impedance spectra for conduction mechanism analysis [60] but as can be observed, plots are well superimposed.

The complex impedance plan plots (Z' vs. Z'') are given in figure 39. Usually, the conduction process plotted in this way should lead to semi-circular arcs [34]. The plots in figure 39 can be considered as a portion of combination of small arc with big arc [61]. These curves are similar to portion curves observed in $CaCu_3Ti_4O_{12}$ [62] where phenomena are clearly modelled by combination of big arc and small arc.

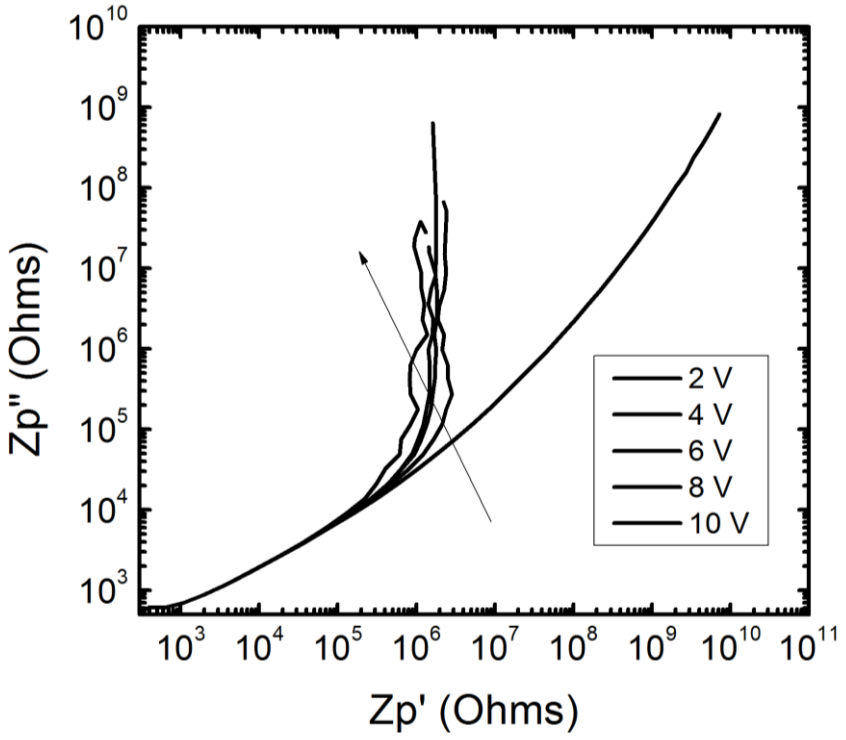

Figure 39: log-log complex impedance plane plot (Zp'' vs. Zp') at different voltages.

To analyze impedance spectra, data are currently modelled using an ideal equivalent circuit consisting of pure resistance (R) and capacitance (C). In this study, experimental data are fitted using equivalent circuit of single parallel resistor R_p and capacitor network C_p with series resistor as schematically shown in figure 40 [62]. The parallel capacitor C_p plays the role of reactive or capacitive component in the solid dielectric while the parallel resistor is used for the average

leakage current (charges carrier transport) through the device. The series resistance Rs represents the contact resistance.

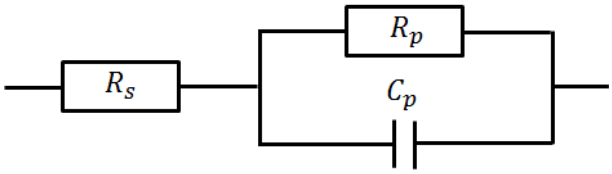

Figure 40: Equivalent circuit used to model electrical signal in AC mode of ZN200 double layers.

Because the top contact has been made with Mo metallization, the interface capacitance which can result from the insulating barriers such as air gap between electrodes and the polymer coating should be negligibly small. We therefore neglect it in our equivalent circuit. According to the used equivalent circuit, the overall impedance of the system is given by:

$$Z^* = Z' + iZ'' \qquad \text{II.7}$$

$$= R_s + \frac{1}{\left(R_p^{-1} + i\omega C_p\right)} \qquad \text{II.8}$$

where

$$Z' = R_S + \frac{R_p}{1 + (\omega C_p R_p)^2} \qquad \text{II.9}$$

and

$$Z'' = R_p \times \frac{\left(\omega R_p C_p\right)}{1 + \left(\omega R_p C_p\right)^2} \qquad \text{II.10}$$

Based on equation II.10, the maximum loss occurs at a frequency of $1/(2\pi R_c C_p)$ and the peak values should be proportional to the parallel resistor. In our curves, resistances are quite superposed here for all DC applied voltages; this confirms the non-clear shifting of peaks observed in figure 38. At lower frequencies the plateau is a contribution of $R_s + R_p$ ($R_s \ll R_p$) with value around of 10^6 Ω for voltages higher than 2 V. At high frequencies the plateau occurs around of 3×10^2 Ω in the Z' spectrum should result from a contribution of the series resistance

only. In the Z'' spectrum, transitions are found at approximately 2×10^5 Hz giving an average capacitance value around 10^{-11} F. Modelling of data recorded at 6 V and 10 V is shown in figure 41. Solid lines are measured data while symbols represent fitting data using the equivalent circuit shown in figure 40.

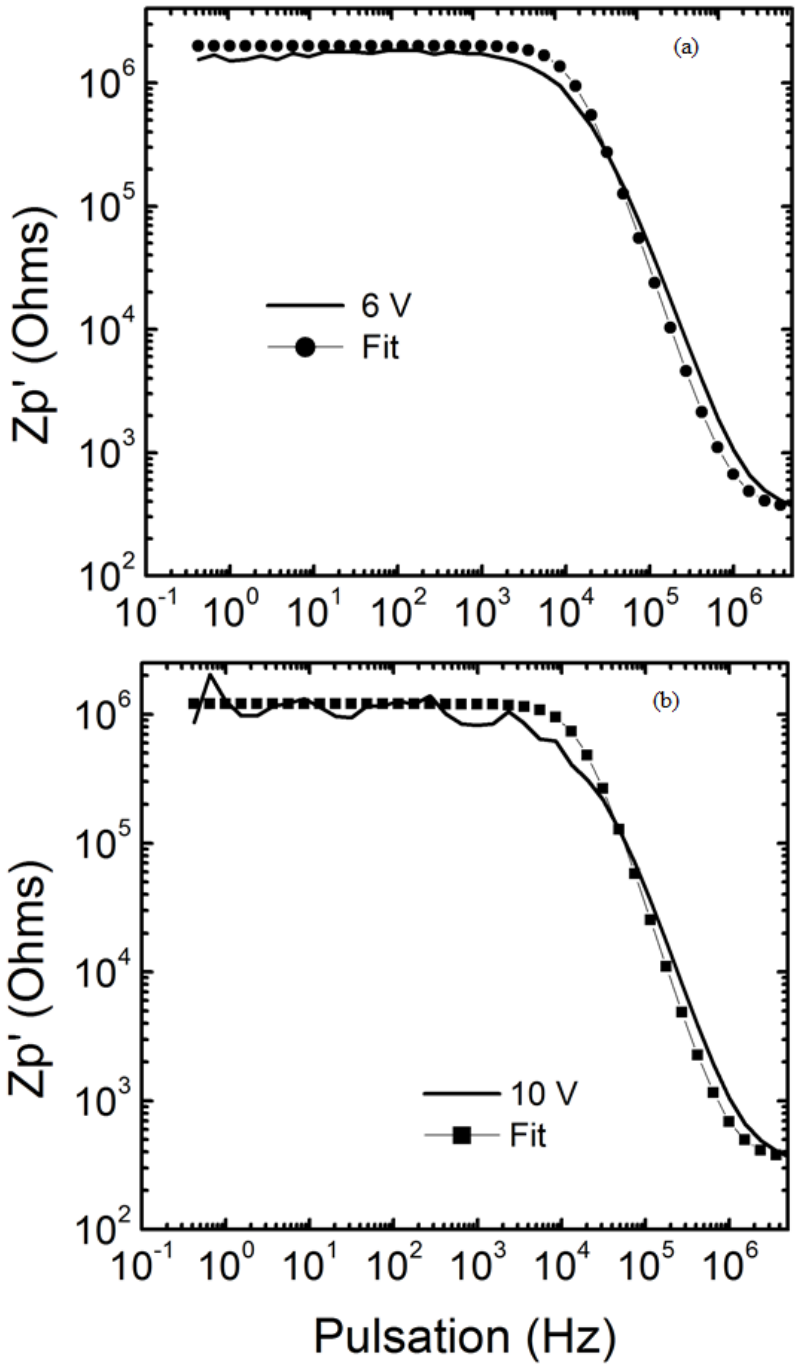

Figure 41: The real part of impedance at 6 V (a) and 10 V (b). Solid lines are measured data and symbols represent fitting results using the equivalent circuit in figure 40.

Fitting parameters are summarized in table 8. It can be observed that the series resistance (contact resistance) remains constant while the resistance of the dielectric coating slightly decreases with DC voltage. This is consistent with the expected behavior for solid dielectric base MIMs (the resistance decreases when the applied electric field increases). According to our fit the value of the capacitance (Cp) is rather constant for both 1 V and 5 V applied voltage indicating independence of capacitive components with respect to bias voltage.

Table 8: Fitting parameters of real part of impedance data at bias voltages of 6 V and 10 V.

Bias (V)	$R_s(\Omega)$	$R_p(\Omega)$	$C_p(F)$
6	350	2×10^6	4×10^{-11}
10	350	1.2×10^6	5×10^{-11}

Based on the values of capacitance, the calculated dielectric constant for a pure ZN200 layer is approximately 2.9, similar to the value reported in the literature [24]; it is in line with dielectric constant values we obtained in dc mode using the Schottky conduction model.

II.4.3. Diffusion barrier properties of ZN200-based DBLs

One of the major aims of this work is to investigate the capability of our ZN200 based DBL systems to act again the diffusion of contaminants such as Fe, Mn, Ni, etc. from SS substrates. To do this, a set of samples has been considered and atomic concentration profiles have been compared. The first series consists in crosslinked ZN200 double layers and the second series is obtained with annealed ZN200 double layers as respectively shown in figure 42.

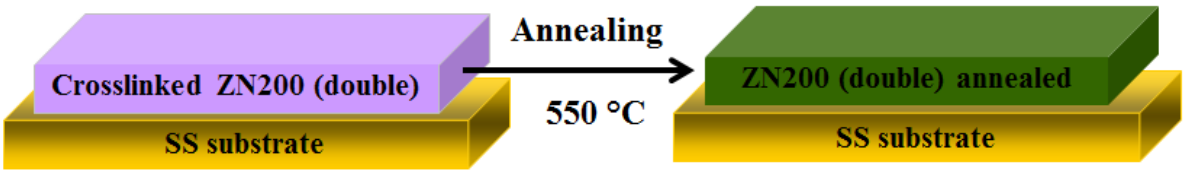

Figure 42: Schematic representation of ZN200 based DBLs retained for atomic concentration profiling: a) Crosslinked ZN200 double layers, b) annealed ZN200 double layers.

GDOES and ToF-SIMS analyses have been combined to evaluate concentration profiles of targeted atoms in different samples. Figure 43 shows results of GDOES depth profiling performed on representative samples of the two series prepared on AISI316 substrates. Concentration profiles of Si, O, and C from ZN200 as well as Fe, Cr, and Ni for steel substrate are depicted versus sputtering time. As can be observed in spectra, there is no significant signal from metallic atoms detected in ZN200 based DBL systems. Interfaces between different layers are clearly identifiable. After annealing at 550°C, intensities (in DBL region) and slope of concentration lines (at interfaces) of transitions atoms are quite similar meaning that there is no or only little diffusion of these atoms into our DBL systems. However, the time to reach the interface between DBL and substrate is remarkably lower for annealed samples than non-annealed samples. This consolidates thermal analyses where it was shown that ZN200 exhibits a significant thickness reduction after annealing over this range of temperature. Another reason for reduction of the sputtering time needed to erode the dielectric material could arise from the strong dependence of sputtering yield on the nature of the sputtered material. Thus, chemical transformations revealed in TGA leading to conversion of the soft polymer coatings into hard coatings can, on the other hand, justify the change observed in the time needed to reach the

interface. However, the sputtering yield of each material has to be properly evaluated to clarify this point.

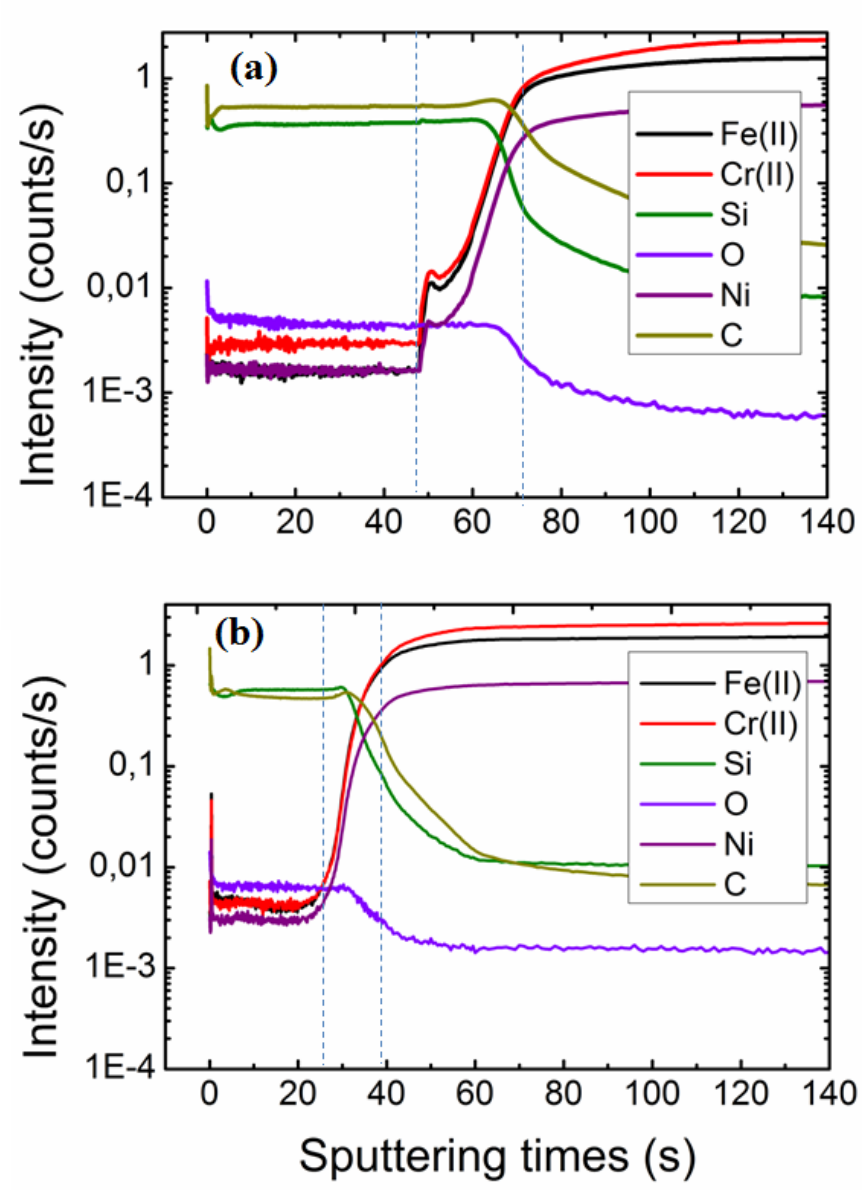

Figure 43: GDOES depth profiling of (a) ZN200 (double)/AISI316 and (b) annealed ZN200(double)/AISI316 .

GDOES depth profiling was also carried out on non-annealed ZN200 coatings and on coatings annealed up to 550 °C in HN_x, both prepared on AISI430, leading to results similar to those obtained previously. Based on these results, one can extrapolate that the combi-layers or reinforced ZN200 double layers retained in the previous section as good dielectric can

additionally block the diffusion of transition metal atoms and hence could prevent CIGS absorbing layer from such contaminants.

ToF-SIMS analyses have also been performed on our ZN200-based DBL to complement GDOES investigations, in order to take advantage of the higher sensitivity and better lateral resolution of ToF-SIMS,. Concentration profiles of SiO, C (ZN200) and Fe and Cr (corresponding to SS) are depicted vs. sputtering time (figure 44) for (i) the crosslinked ZN200 coating and (ii) the ZN200 coating annealed up to 550°C in HN_x. It can clearly be seen that there are no transition metal atoms at the top of DBL since intensities related to these atoms seem to be quite identical before and after thermal treatments.

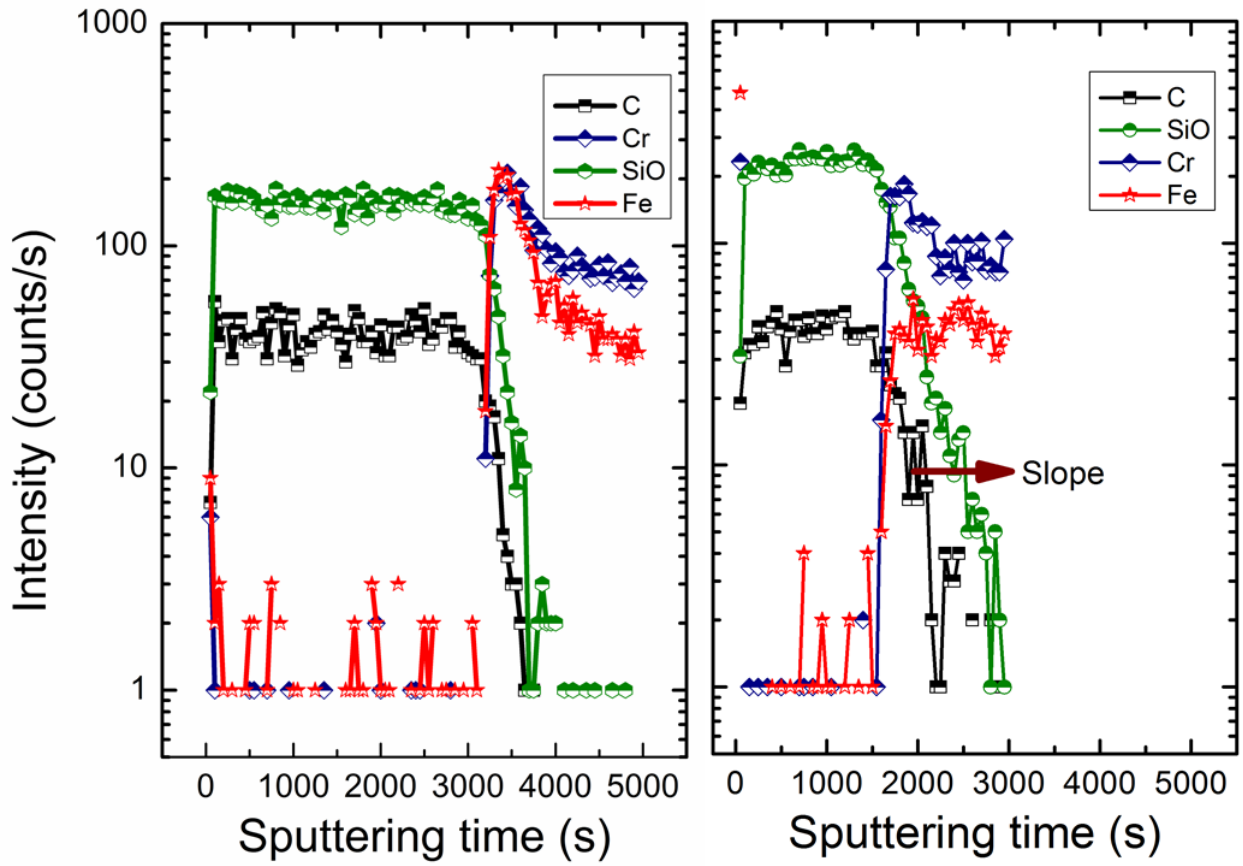

Figure 44: ToF-SIMS depth profiling for (a) crosslinked ZN200 (double)/AISI316 on area of 200 x 200 µm² and (b) annealed ZN200 (double)/AISI316 on an area of 100 x 100 µm².

The annealed sample reveals however some changes. First, compared to as-deposited samples, the signal of iron is lower than that of chromium at near interface of steel substrate. The increase of chromium signal is tentatively assigned to diffusion of chromium at the top most part of steel.

Second, it can be checked that the slopes of the SiO and C lines are slightly increasing towards the steel side for annealed sample. As a first approximation, one can relate this to surface irregularity or streaks on steel substrate (see AFM image in figure 18). The size of streaks present is however around 5 to 10 µm, much lower than the analysed area in SIMS (100 µm × 100 µm). The SIMS signals should probably be independent on the presence of surface asperities, so the increase in slope for C and SiO at the interface could be a hint of some diffusion of these particles into the steel substrate.

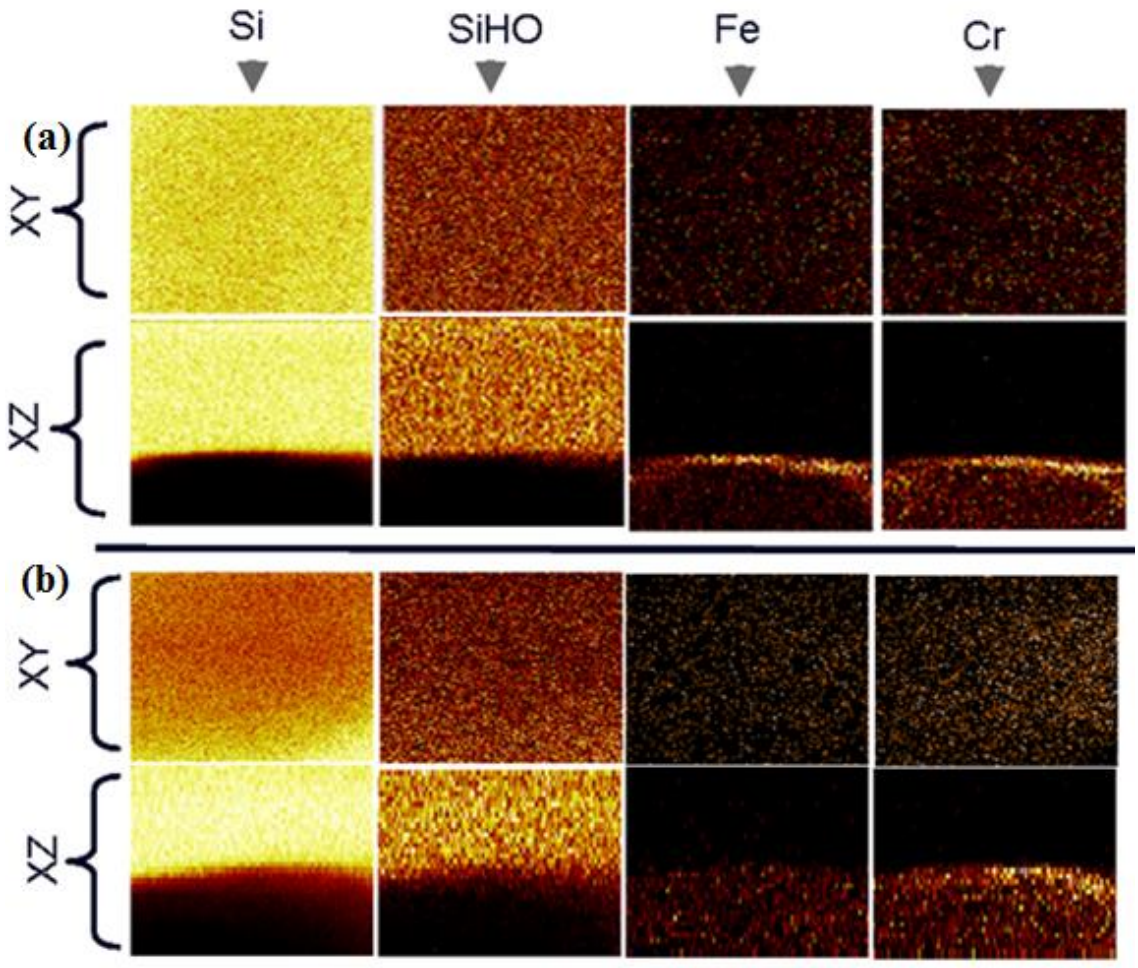

Figure 45: ToF-SIMS images in XY plane (lateral plane: 100 µm x 100 µm) and XZ plane (cross section: depth) of (a) ZN200 double layer on SS and (b) the annealed ZN200 layer on SS.

3D images reconstructed from SIMS data plotted in figure 42 are shown in figure 45 to evaluate the lateral and depth distributions of Si, SiHO (for ZN200) and Fe, Cr (for steel). It clearly shows a homogeneous distribution in the lateral plane (XY) images related to each selected particles for both ZN200/SS and annealed ZN200/SS samples. A strong contrast in color is found between zones related to ZN200 coating and substrate. The absence of any locally intense brightness in surface images confirms the good covering of ZN200 coatings without discontinuity, confirming the absence of cracks even after annealing. This is in line with previous in SEM and AFM observations.

In cross-section or depth mapping, a net transition is observed between images related to ZN200 layers and steel substrate for annealed and non-annealed samples. This correlates with no detection of transition metals at the top of ZN200 layers observed in depth profiles (SIMS, GDOES). It is a signature of the fact that ZN200 coatings still provide the diffusion barrier effects even after high thermal annealing. Depth mapping reveals also that there is an enrichment in Fe and Cr at the interface of ZN200 and SS non-annealed samples. The enrichment in Fe seems to disappear only in the case of annealed sample. This provides additional support to the diffusion of chromium at the interface reported in SIMS depth profiles of annealed samples and could help in understanding adhesion mechanisms at the interface between steel and ZN200 coatings (see chapter IV).

II. 5. Summary

Intensive investigations have been carried out to evaluate structural, electrical and diffusion barrier properties for hybrid polymer based on ZN200 polysilazane. It was shown that ZN200 double layers are an efficient barrier against the diffusion of transition metals. Thermolysis analyses of ZN200 powders revealed an important mass loss. However thermal stabilization was found to occur around 550°C. Coatings prepared on AISI316 or AISI430 stainless steels are free of cracks and exfoliation even after annealing at temperature up to 550°C in various atmospheres. AFM analyses reveal that ZN200 coatings significantly reduce the surface roughness of SS substrate. Indeed, the RMS of uncoated SS substrate is around 500 nm, but, after application of ZN200 coating, the measured RMS is around 8 nm. The surface roughness

ZN200 coatings is slightly altered after annealing since the value of RMS measured for these coatings is 16 nm.

Thermal treatments however strongly weaken a dielectric. Indeed an important increase in leakage current was observed for MIMs fabricated with annealed ZN200 double layers. The weakening of the dielectric strength was especially assigned to the deceased thickness resulting from annealing. On the other hand, volatilizing of gases was also found for the annealed ZN200 coatings thereby creating pinholes which can additionally contribute to weakening the dielectric strength. Coating made in ambient atmosphere and cleanroom are compared showing that the yield is remarkably low in ambient atmosphere. This electrical insulation reducing is attributed to dust inherent to ambient atmosphere processing. Effects of these impurities are found to be more pronounced on large area and are confirmed by the fact that the maximum acceptable level fixed for the leakage current was often reached for the large area MIM capacitors (50 mm × 50 mm). The increase of the leakage current in the largest MIMs is assigned to a possible increase of the amount of impurities in the coating when the area is increasing.

To obtain a strong dielectric, a new stack of dielectric system has been developed, the so-called combi-layer. The combi-layer consists of stabilized ZN200 double layer coupled with a 400 to 600 nm-thick SiO_xAl_y layer and an additional ZN200 single layer. A yield of 100 % was reached with this type of stacks. Accordingly, combi-layers become our favored dielectric solution and were used for investigating dielectric reliability. It was shown that the leakage current mechanism in MIM capacitors fabricated with our combi-layers is better described using the Schottky emission theory. Then, Schottky models enables to obtain a better fit of the dielectric constants using *log(J)-V* semi-logarithmic representations. With the time to breakdown characteristic, it was demonstrated that non-annealed combi-layers with a total thickness of 4.4 µm can tolerate 1000 V. The thickness of the combi-layer is reduced from 4.4 µm to 3.7 µm and the breakdown voltage tolerated by the corresponding MIMs is more or less 500 V. Values of dielectric strength found here for our combi-layers are better than those recently reported on dielectric materials commonly used for the fabrication of CIGS solar cells on metals. As an example, the disruptive field of our combi-layer is about four times higher than the disruptive field reported for MIM capacitors made with SiO_2 in [2]. The maximum value of 300 V is reported on 6 µm-thick Al_2O_3 films by Kessler and co-worker in [63].

Finally, impedance spectroscopy study of ZN200 solid dielectrics was also conducted. The frequency dependence of the real part of impedance is found to be well fitted using equivalent circuit constituted of single parallel resistor R_p and capacitor C_p network with a series resistor R_s and the fitting parameters are consistent with experimental data.

References:

[1] P. Jackson, P.O. Grabitz, A. Strohm, G. Bilger, H.W. Schock, Contamination of Cu(In,Ga)Se_2 solar cells by metallic substrate elements. R P. Jackson/ Philip.Jackson@ipe.uni-stuttgart.de

[2] K. Herz, F. Kessler, R. Wächter, M. Powalla, J. Schneider, A. Schulz, U. Schumacher, Thin Solid Films 403 – 404 (2002) 384/389.

[3] D. Amouzou, P. Guaino, L. Fourdrinier, J-B Richir, F. Maseri, R. Sporken, Thin solid films, (2013), http://dx.doi.org/10.1016/j.tsf.2013.06.043.

[4] R. Wuerz, A. Eicke, M. Frankenfeld, F. Kessler, M. Powalla, P. Rogin, O. Yazdani-Assl, Thin Solid Films 517 (2009) 2415/2418.

[5] A. Martin, Microelectronics Reliability 45 (2005) 834/840.

[6] K. Moriwaki, M. Nomoto, S. Yuuya, N. Murakami, T. Ohgoh, K. Yamane, S. Ishizuka, S. Niki, Solar Energy Materials and Solar Cells, 112 (2013) 106/111.

[7] http://www.polysilazanes.com/americas/products/advanced-materials/htt-1800/.

[8] P.Yimsiri, M.R. Mackley, Chemical Engineering Science 61 (2006) 3496/3505.

[9] Matthew Roberts, An Feng Huang, Phil Johns, John Owen, Journal of Power Sources 224 (2013) 250/259.

[10] Michael Outred, Mark H. Rummeli, Edward B. M. Steers, Journal of Analytical Atomic Spectrometry 9 (1994) 381/384.

[11] R. Payling, D. G. Jones, and A. Bengtson, Glow Discharge Optical Emission Spectrometry, John Wiley & Sons, New York, Weinheim, Brisbane, Singapore, Toronto, 1997.

[12] S. Hofmann, Surface Interface Analysis 4 (1980) 148.

[13] ASTM D3359-07 Standard Test Methods for Measuring Adhesion.

[14] Zhe Chen, K. Prasad, C.Y. Li, S.S. Su, D. Gui, P.W. Lu, X. He, S. Balakumar, Thin Solid Films 462–463 (2004) 223/226.

[15] J.H. Wang, P.T. Liu, T.S. Chang, T.C. Chang, L.J. Chen, Thin Solid Films 469–470 (2004) 393/ 397.

[16] W. R. Schmidt, V. Sukumar, W. J. Hurley, R. Garcia, R. H. Doremus, L. V. Interrante, Amer. Ceram. Sot., 73-8 (1990) 2412/8.

[17] C.Y. Wang, Z.X. Shen, J.Z. Zheng, Appl. Spectrosc. 54 (2000) 209.

[18] M. Sugimoto, T. Shimoo, K. Okamura, T. Seguch, *J. Am. Ceram. Soc.*, 78 (1995) 1849/1852.

[19] Thi Dieu Hang Nguyen, thesis, Université du Sud Toulon Var (2005).

[20] O. Funayama, Y. Tashiro, A. Kamo, M. Okamura, and T. Isoda, *J. Mater. Sci.* 29 (1994) 4883/4888.

[21] D. Bahloul, M. Pereira, P. Goursat, J. *Amer. Ceram, Sot., 76(5)* (1993) 1156/62.

[22] M. F. Gonon, S. Hampshire, J. P. Disson and G. Fantozzi, European Ceramic Society 15 (1995) 683/688.

[23] J.D. Torrey, R. K. Bordia, Jr. C. H. Henager, Y. Blum, Y. Shin, W. D. Samuels, J. Mater. Sci. 41 (2006) 4617/4622.

[24] Torsten Breuning , Journal of Analytical and Applied Pyrolysis 49 (1999) 43/51.

[25] M. Günthner, T. Kraus, A. Dierdorf, D. Decker, W. Krenkel, G. Motz, Journal of European Cermaic Society, 29 (2009) 2061/2068.

[26] Y. Iwamoto, K. Sato, T. Kato, T. Inada, Y. Kubo, European Ceramic Society 25 (2005) 257/264.

[27] Y. Hasegawa, *Mater. Sci.* 24(1989) 1177/1190.

[28] D. Mocaer, R. Pailler, R. Naslain, C. Richard, J. P. Pillot,J. Donogues, *J. Mater. Sci.*, 28 (1993) 2615/2631.

[29] Gabriela Mera, Ralf Riedel, Fabrizia Poli, Klaus Müller, European Ceramic Society 29 (2009) 2873/2883.

[30] PDF file 00-033-0397.

[31] Y. Iwamoto, W. Völger, E. Kroke, R. Riedel, R., *Am. Ceram. Soc.*, 84 (10) (2001) 2170/2178.

[32] P. López Varo, J.A. Jiménez Tejada, J.A. López Villanueva, J.E. Carceller, M.J. Deen, Organic Electronics 13 (2012) 1700/1709.

[33] S.M. Sze, Physics of semiconductor devices, second edition, Wiley Interscience (1981).

[34] A.K. Jonscher, Dielectric Relaxation in Solids (London: Chelsea Dielectrics Press, 1983).

[35] K-H. Allers, Microelectronics Reliability 44 (2004) 411/423.

[36] Allers K-H, Schwab R, Walter W, Schrenk M, Koerner H, IEEE IRW (2002) 96/101.

[37] J. W. McPherson, R. B. Khamankar, A. Shanware, Microelectronics Reliability 40 (2000) 1591/1597.

[38] Y. L. Chiou, J.P. Gambino, M. Mohammad, Solid-state electronic, 45 (2001) 1787/1791.

[39] G. Kreiger, R.M. Swanson, J. Appl. Physics (1981) 25/5710.

[40] C. Mahata, M.K. Bera, M.K. Hota, T. Das, S. Mallik, B. Majhi, S. Verma, P.K. Bose, C.K. Maiti, Microelectronic Engineering 86 (2009) 2180/2186.

[41] H.M. Chenari, H. Sedghi, M. Talebian, M. Golzan, A. Hassanzadeh, Nanomaterials (2011) 190391.

[42] Chao Wang, Ling Fang, Gong Zhang, Da-Ming Zhuang, Min-Sheng Wu, Thin Solid Films 458 (2004) 246/250.

[43] Y. Segui, Diélectrique-courant de conduction-Techniques de l'ingénieur-Traité Génie électrique, article D2301-2000.

[44] D.R. Wolters, J.F. Verwew A.T.A. Zegers-Van Duijnhoven, Dielectric breakdown in SiO_2 (1999).

[45] K. D. Das Gupta and K. Joyner, Journal of Physics D : Applied Physics, 9 (1976) 829/840

[46] A. K. Jonscher, J. Phys. D: Appl. Phys. 32 (1999) 57/70.

[47] E. Von Schweidler, Ann. Phys. 24 (1907) 711.

[48] Nguyen Duc Hoang, thesis on « Étude des propriétés électriques des élastomères silicones utilisés pour l'isolation électrique » 2005.

[49] K. D. Gupta, IEEE, 1997, Vol. 4. No. 2, pp. 149-156.

[50] Tony Blythe, David Bloor, electrical properties of polymers, Cambridge University Press (2005), P.31.

[51] S.M. Sze, Physics of semiconductor devices, second edition, Wiley Interscience (1981)

[52] R. Ongaro, A. Pillonnet, Rev. Phys. Appl. 24 (1989) 1085.

[53] H. Ertap, G. M. Mamedov, M. Karabulut, A. Bacıoglu, luminescence 131 (2011)1376/1379.

[54] W.R. Harrella, J. Frey, Thin Solid Films 352 (1999) 195-204

[55] S.M. Sze, Physics of semiconductor devices, second edition, Wiley Interscience (1981) P.403

[56] A. Moliton. Électronique et optoélectronique organique. Collection telecom. Springer-Verlag: France (2011) 131/172.

[57] P. Solomon. J Appl. Phys. 48 (1977) 3843/9.

[58] Hongbo Lu, Xingyuan Zhang, Hui Zhang, Journal of Appl. Phys. 100 (2006) 054104.

[59] Jianjun Liu, Chun-Gang Duan, Wei-Guo Yin, W. N. Mei, R. W. Smith, and John R. Hardy, Phys. Rev. B 70 (2004) 144106.

[60] S. H. Kim , S. C. Lim, J. H. Lee, T. Zyung, Current Applied Physics 5 (2005) 35/37.

[61] J. Liu, C-G. Duan, W-G. Y. W. N. Mei, R. W. Smith, J. R. Hardy, Physical Review B 70 (2004) 144106.

[62] D. C. Sinclair, T. B. Adams, F. D. Morrison, and A. R. West, Appl. Phys. Lett. 80 (2002) 2153.

[63] R.Wächter, F. Kessler, K. Herz, M. Powalla, Proceedings 10 Bundesdeutsche Fachtagung Plasmatechnologie, 2001, p. 39

CHAPTER 3
Molybdenum Back Contact on Polysilazane Based Barrier Layers

III.1. Introduction

Various metals including molybdenum [1,2], platinum [3], gold, copper and silver [4] or nickel [5] have been investigated as contact for CIGS solar cells. Mo films have emerged as back contact for CIGS solar cells [2] because they are inert in selenium atmosphere, stable at high temperature and do not alloy with components of CIGS film. Mo films are currently being optimized on conventional SLG substrates and it has been shown that properties of Mo films can strongly affect performance of solar cells. Jubault et al. [6] compared Mo films deposited in pressure range of 2.6 x 10^{-1} Pa to 2.6 Pa by DC and RF sputtering for CIGS solar cells and found a large difference in performances of solar cells. They found that photovoltaic performance is much better when Mo back contacts are deposited by DC sputtering. A method is described by Scofield et al. in [2] for fabricating low-resistivity molybdenum films on SLG substrates with good adhesion. It was found that 1 µm-thick Mo films sputtered at low argon pressure (2.6 x 10^{-2} Pa to 2.6 x 10^{-1} Pa) exhibit low resistivity, between 10 and 15 µΩ.cm; films are however under compressive stress and often suffer from poor adhesion. In contrast, Mo films sputtered with high argon pressure (2.6 x 10^{-1} Pa to 2.6 Pa) have resistivity as high as 50 to 250 µΩ.cm; they are under tensile stress and additionally adhere well to glass substrates. By combining Mo films deposited at 1.3 Pa and 1.33 x 10^{-1} Pa respectively, l µm-thick of Mo bilayers were obtained with both low resistivity between 12 and 15 µΩ.cm, and good adhesion.

The purpose of our study is to perform Mo films on ZN200 hybrid-polymers used as DBL for CIGS solar cells (see chapter II). Special emphasis is placed on sheet resistance and good adhesion. These layers are then intended to be used as back contacts for CIGS solar cells. Thus,

surface morphology and optical properties of Mo films were analysed vs. argon working pressure in order to understand the evolution of microstructures of these films.

III.2. Mo film deposition

Mo films are sputtered on SS coated with ZN200 based DBLs prior stabilized in HNx at 550°C. The first series of Mo films was prepared at room temperature in pressure between 2.6 x 10^{-1} Pa to 2.6 Pa. Another series of Mo films is obtained by depositing films directly on heated substrates. In the last case, the temperature of substrate is calibrated using a thermocouple and is kept constant at 550°C during deposition. For all depositions, the DC power is fixed at 400 W and the sample-holder is in rotation.

III.3. Characterization

SEM and AFM analyses were performed to characterize the microstructure and the surface morphologies of Mo films. Resistivity of Mo films was measured using a four-point probe while the optical reflectance of films is recorded using UV-visible spectroscopy in wavelength range of 350 to 2000 nm. Adhesion was evaluated using ASTM D3359-07 adhesion standard test called cross-cut-test. Important results from these characterizations will be discussed in the following sections.

III.3.1. Preliminary study of Mo films

We reported in the previous chapter that Mo films prepared on non-stabilized ZN200 polymer coatings can be completely exfoliated when the whole system is heated due to thermal degradations of the polymer and recommend their stabilization prior to use for CIGS applications. Thus, the first step of Mo film optimization was to check if the polymer coatings are well thermally stable and this especially for Mo films grown on heated substrates. In figure 1 are shows SEM images of Mo films prepared on stabilized ZN200 coating. Figure 1.a shows Mo film deposited at room temperature while figure 1.b shows Mo film annealed up to 550 °C. There is no clear difference between the two images and, in particular, no exfoliation of Mo films.

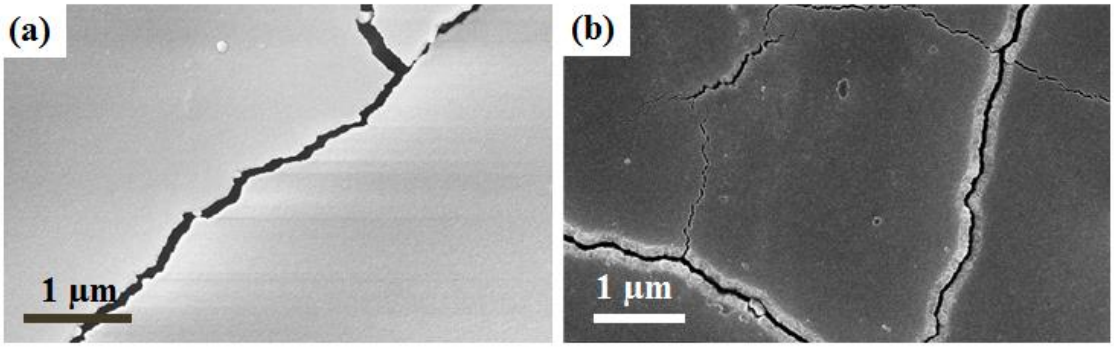

Figure 1: SEM image of Mo films deposited onto stabilized ZN200 coatings (a) films prepared at room temperature (b) film annealed up to 550°C.

III.3.2. Influences of the working pressure

To check effects of working gas pressure on the microstructure of our Mo films, all sputtering parameters such as DC power density, sccm argon, distance between the cathode and the sample-holder are fixed, and the only variable being Ar total pressure. The thickness of Mo films is around 300 nm. Films are examined by SEM.

Based on the surface morphologies and as shown in figure 2, our films can be clearly classified in four different kinds of microstructures (microstructure A $[2.6 \times 10^{-1} - 3.9 \times 10^{-1}$ Pa], microstructure B $[5.3 \times 10^{-1} - 7.9 \times 10^{-1}$ Pa], microstructure C $[9.3 \times 10^{-1} - 1.2$ Pa] and microstructure D $[1.3 - 2.6$ Pa]). It can be observed here that microstructures of Mo films deposited at pressure lower than 3.9×10^{-1} Pa are compact with no cracks (figure 2.a). The microstructure consists in dense platelets and there is no evidence of presence of voids in this type of Mo films and is in line with investigations of Hoffman et al. [7]. The densification of films at low pressure and low temperature is usually assigned to atomic peening effects caused by energetic particles such as atoms or ions [8]. The phenomenon is normally based on the fact that particles from lower working pressure possess high energy then they strike the growing film surface causing locally atomic displacements. As consequence, the distance between aggregates is reduced leading to densification. On another hand, several predictions [11,9] indicate that the densification of thin films could result from incorporation of adparticles into grain boundaries during deposition.

The microstructure B is shown in figure 2.b and is constituted of 10 µm-sized domains or cracks clearly separated by voids. On the nanometer scale, microstructures B are made of elongated grains.

Compared to type B films, no cracks were observed in microstructures C and D films (figure 2.c and d) but grains seem to be smaller and spherical. Voids are seen in films with microstructure D; this can be attributed to the fact that thin films usually become more porous with an increase of working pressure [6]. Porous microstructures are usually obtained in severe kinetic restraints conditions where both, mobility of adparticles as well as that of grains boundaries is especially low [10,11].

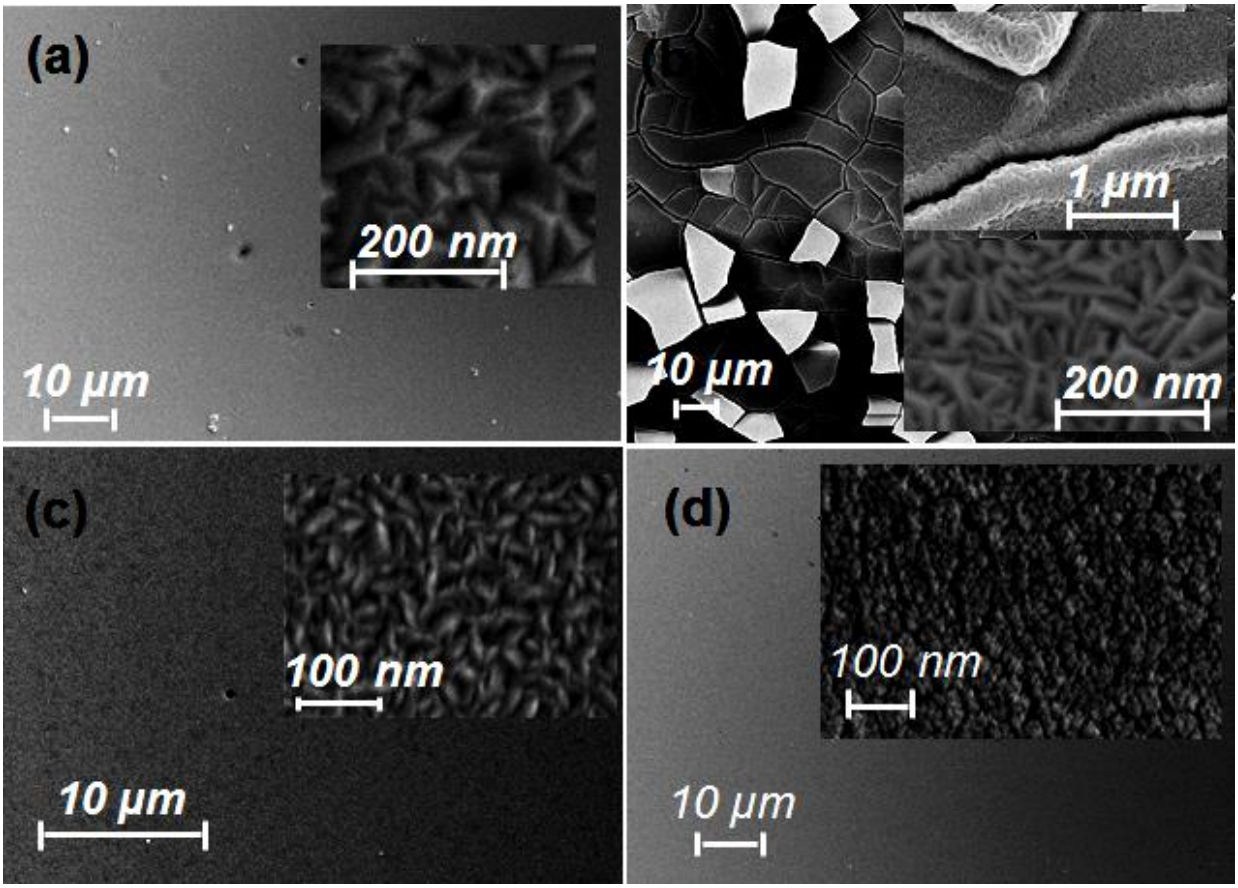

Figure 2: Four different microstructures obtained with Mo films on ZN200 based coatings: (a) microstructure A, (b) microstructure B, (c) microstructure C and (d) microstructure D. Corresponding range of working pressure can be found in the text.

The common feature of all structures found here is the random distribution of grains even if transitions in microstructure with respect to sputtering gas pressure is clearly observed [12].

Normally, the terminology of classification of thin films microstructure was introduced by Thornton in [13] and is widely used. Thornton presented microstructural evolution of pure elemental films as a function of homologous temperature (the homologous temperature is defined as ratio of T_{dep}/T_{melt}, where T_{dep} is temperature expressed in K while T_{melt} is the melting temperature of deposited material also expressed in K). Thus, possible microstructures of thin films are studied and arranged in structure zone models [14, 15]. The concept of classification adopted here does not follow that presented by Thornton. The difference results in the fact that temperature coupling required in Thornton's model is not necessary in ours.

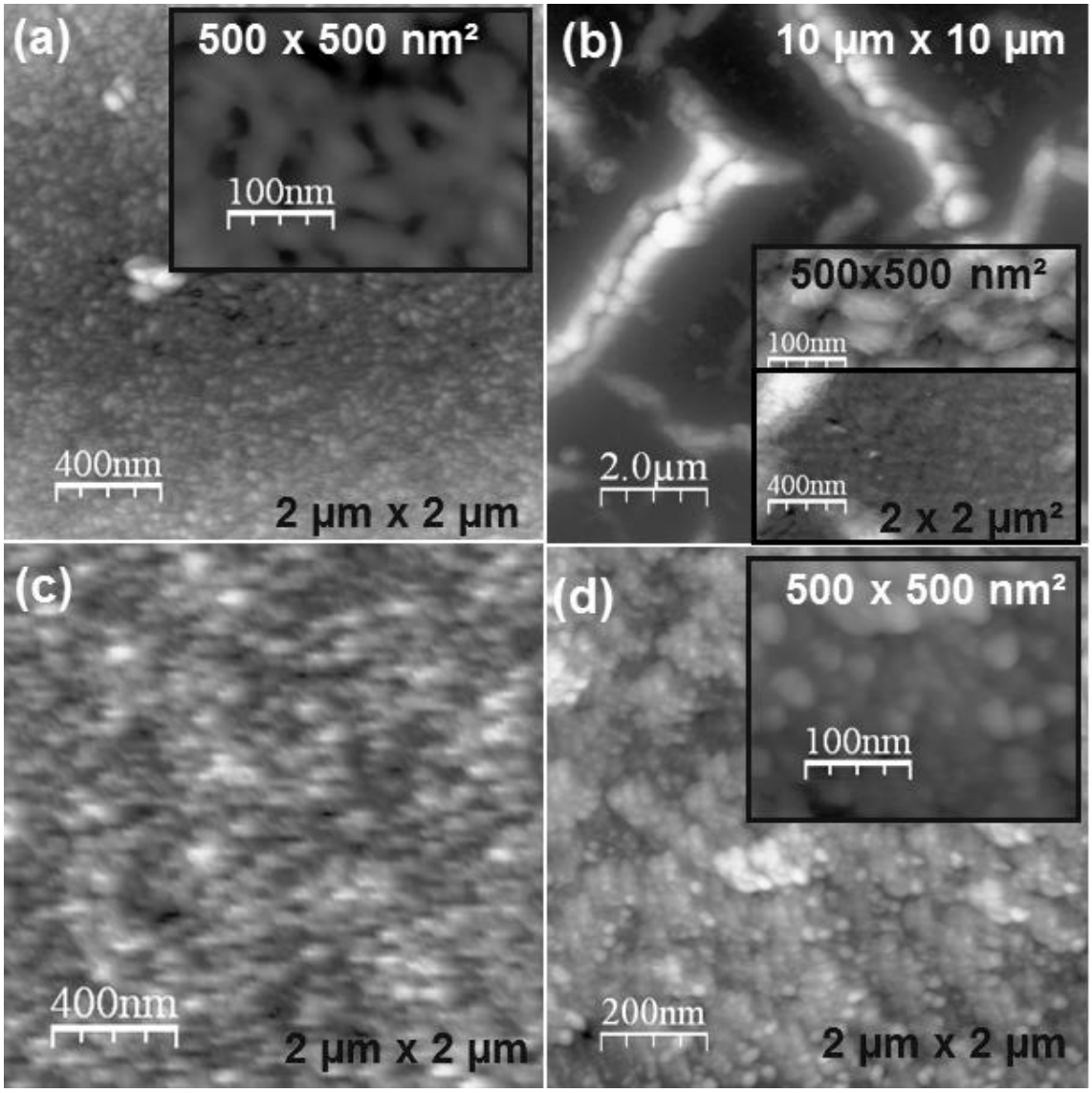

Figure 3: AFM images of Mo films corresponding to (a) microstructure A, (b) microstructure B, (c) microstructure C, (d) microstructure D.

AFM analyses are also performed on selected specimens related to these identified in SEM examinations and indicated similar results (figure 3). Voids between grains are better observed for all films and the porosity seems again to increase with the working pressure. Additionally to a structural analysis, roughness of different films is also evaluated in AFM. The surface roughness is evaluated over three different images with sizes of 10 µm × 10 µm, 2 µm × 2 µm and 500 nm x 500 nm. Average values of peak-to-valley roughness are determined and are 12 nm, 40 nm, 10 nm and 13 nm for microstructure A, microstructure B, microstructure C and microstructure D respectively. In contrast with porosity, this result reveals that roughness does not necessary increase with the working pressure. The roughness increasing on Mo film with microstructures B could associate to cracking. Normally, voids on the surface should contribute to an increase of roughness but the evaluation of their contribution on roughness can become hard in some case since it definitely depends on instrumental resolution. Thus, nanoporous surfaces (pores with a few nanometers of sizes as an example) could be seen as smooth even with highly resolved AFM.

Figure 4 shows the variation of sheet resistance (R_{sq}) of our Mo film with respect to working pressure (error bars is 5 %). Similar results were found for Mo films on glass. Four regions are clearly identified.

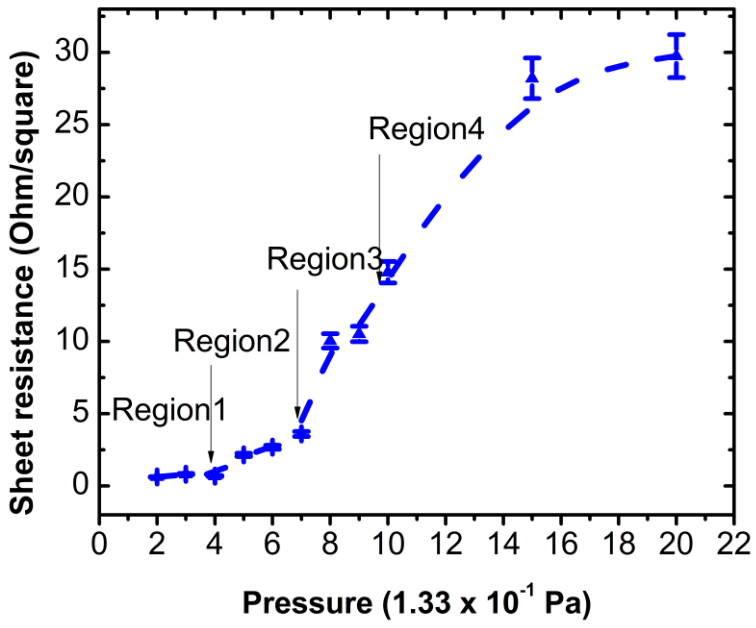

Figure 4: Surface resistivity of Mo films as a function of the working pressure.

As it can be observed, ranges of pressure associated to each region surprisingly correspond to pressure ranges reported for microstructural transitions. This highlights a possible link between Mo films microstructures and their sheet resistance. It is especially noteworthy that a straightforward sheet resistance measurement can then be used to identify the microstructure of Mo films.

At low pressure, below 4×10^{-1} Pa, resistivity is around $0.56\ \Omega/sq$. This is equal to the resistivity of bulk Mo [6]. In the pressure range between $5 \times 10^{-1} - 8 \times 10^{-1}$ Pa, the resistivity is approximately two times higher. For pressures up to 1.33 Pa, the resistivity is near $10\ \Omega/sq$. Above 1.33 Pa, resistivity is remarkably increased with maximal value around $30\ \Omega/sq$ at 2.6 Pa. Resistivity values for pressure up to 1.33 Pa are comparable to that found in the literature [2,16] while above this pressure, values found are approximately ten times higher.

The increase in resistivity with the working pressure can be explained by the increase in porosity. It was found in [6] that by varying the working pressure from 0.26 Pa to 2.66 Pa, the porosity in Mo films increased and the electron mobility decreased from 8 to 1.8 $cm^{-2}.V^{-1}.s^{-1}$. Otherwise, our Mo films are usually exposed to air before measurements, thus, the resistivity could increase due to oxidation. Finally, in order to minimize the series resistance for the solar cells, Mo deposited at low pressures which give rise to the lowest sheet resistance should be preferred. However, the adhesion, an important parameter for the fabrication of CIGS solar cells, especially crucial for scribing step can turn out to be the limiting parameter for Mo films deposited at low pressure.

Table 1: Summary of adhesion level of Mo films deposited at different working pressures.

Type of zone	Pressure ($1{,}33 \times 10^{-1}$ Pa)	Adhesion level
Microstructure A	[2-3]	0/5 (failed)
Microstructure B	[4-6]	5/5 (pass)
Microstructure C	[7-9]	5/5 (pass)
Microstructure D	[10-20]	1-3/5 (warming)

Adhesion tests were then performed on films deposited at various pressures and results are summarized in the table 1. Adhesion often fails when Mo films are deposited at low and high pressure. Similar behaviour was reported on glass in [2,6] but no explanation was given. Films deposited at intermediate pressure [$54 \times 10^{-1} - 9 \times 10^{-1}$ Pa], corresponding to microstructure B and C, show excellent adhesion. One can then try to combine well-adhered Mo films with another Mo film, deposited at low pressure for high conductivity, to form a Mo bilayer. Such an approach has been reported on glass substrates [2]. The best combination in our case could be the combination of microstructure A-type films with the well-adhered C-type films. The problem is that, microstructure C type films can be also cracked sometimes as it can be observed in figure 5.a and b for films deposited at 0.8 and 1.1 Pa respectively.

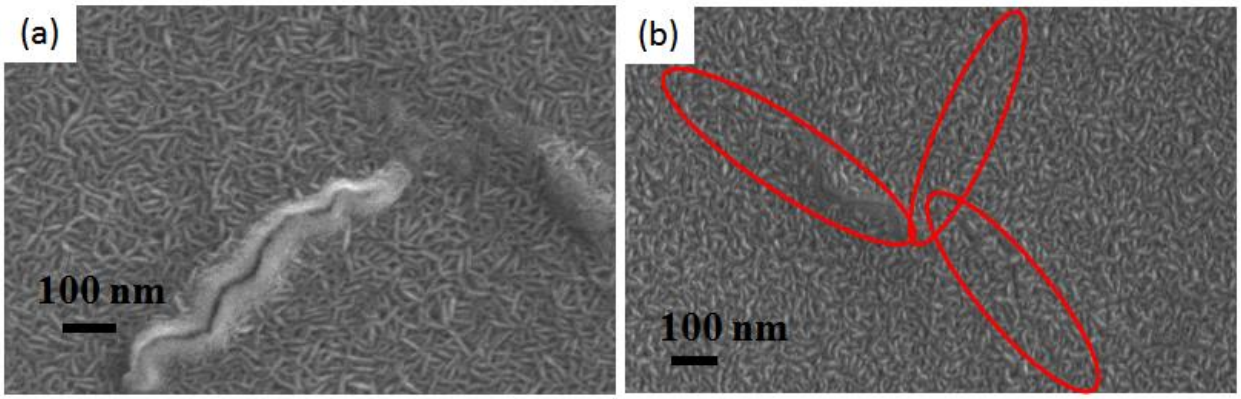

Figure 5: Microstructure C films deposited at (a) 0.8 Pa and (b) 1.1 Pa. Cracks are observed in both films are cracked.

Cracking in type B or C films should have negative impacts on the growth of type A films. For this reason, the well-adhered and more cracked films (microstructure B films) will be discussed in detail in the following section to investigate first the evolution of cracking domains with respect to the thickness and second to determine the appropriate thickness for the layer combination.

III.3.3. Evolution of cracks with thickness for type B films

Figure 6 (a-j) shows SEM images of 10 nm, 20 nm, 30 nm, 40 and 100 nm-thick Mo films deposited at around 5.5×10^{-1} Pa (giving type B like films). 10 nm-thick films are less cracked compared to all other films. It can be observed however that the size of cracked domains, voids between cracks and the depth of cracks clearly increase when the thickness of coatings increases.

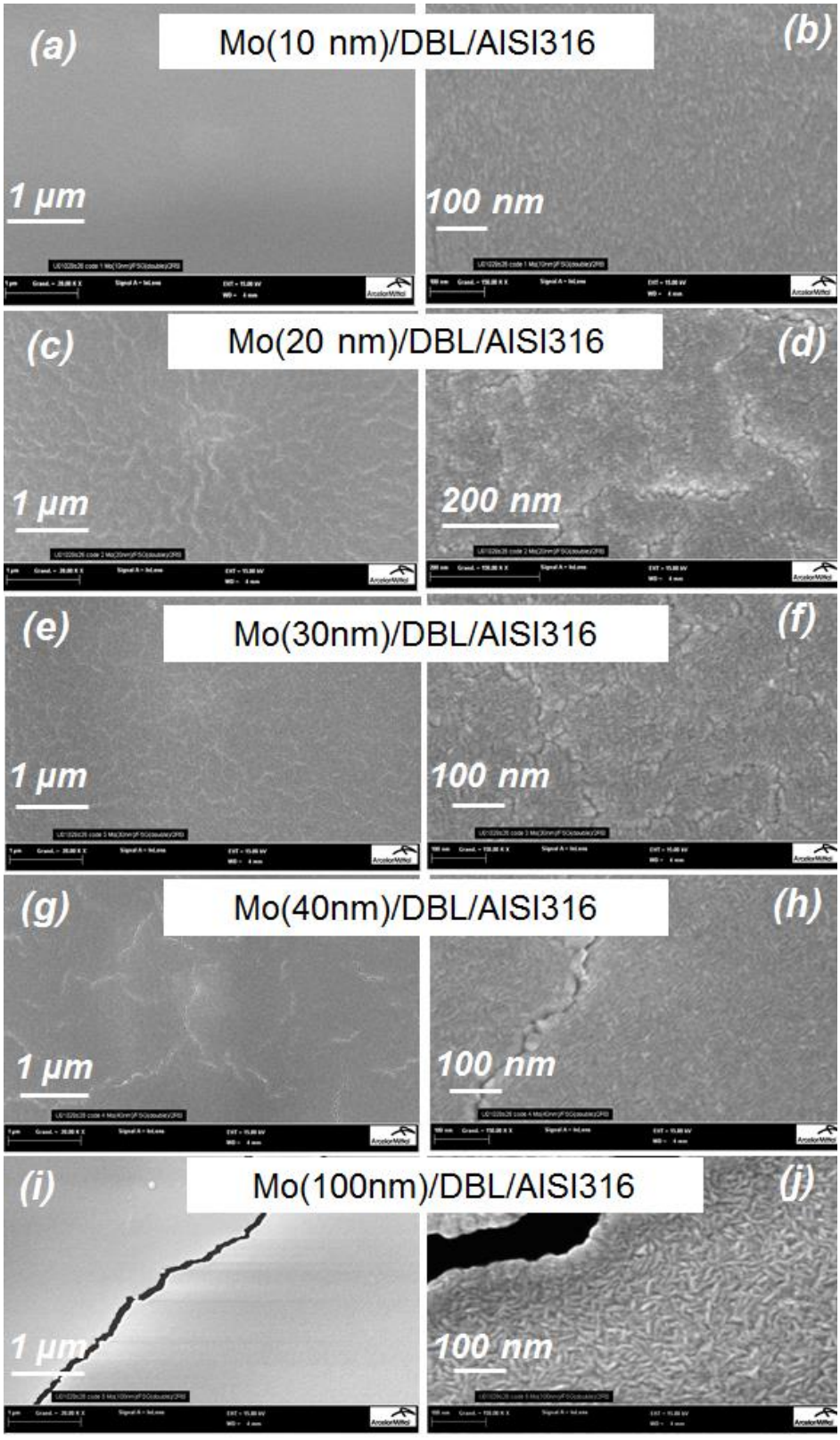

Figure 6: Evolution over thickness of cracked domain for microstructure B type films.

Size of cracking domains also significantly increases with thickness. Cracking of Mo coatings are probably caused by stress in the film since all thin films attached to substrate should be systematically under stress.

Films are under tensile stress when they want to be smaller than the substrate or under compressive stress when they want to be larger than the substrate. A total stress in films is a sum of contributions of thermal expansion (which can be compressive or tensile), ion peening (a compressive stress) and grain boundaries (which usually generate tensile stress), known as extrinsic stress and incorporated defects generate intrinsic stress.

Of all these stresses only the contribution of grain boundaries is thickness-dependent. Others stress contributions are thickness-independent and can be isolated because thickness is the only variable parameter considered in our study.

Various theories have been proposed to explain development of stress in thin films [17,18] and three aspects are usually considered in studies of structure of thin films versus thickness: evolution of stress with thickness, evolution of stress with grain number or width per unit length and finally, evolution of grain size with the thickness. It was reported in [19,20,21,22] that average stress in thin films is a gradient over thickness. As an example, sputtered coatings such as Cr, CrN [23,24] or Mo [25] have been studied and a link between stress and thickness was clearly found. Etch-back experiments have been performed on Cr films, and it was found that tensile stress considerably increases when films become thinner [23]. Janssen et al. reported in [24] that the average stress, σ_{av} in CrN films is a gradient over thickness, t_f and the evolution of this stress can be given by a power law as follows:

$$\sigma_{av}(t_f) \infty C_1 + C_2 t_f^{-\alpha} \qquad \text{III.1}$$

In this model, they attributed the evolution of grain growth to exponent α while the constant C_1 is referred to limiting stress in the film and C_2 as a constant proportional to amount of stress generated per grain boundaries. For CrN films or even for Cr films, a correlation between the stress as function of film thickness and the grain size as function of height in the film has been demonstrated [23]. A power law is then found by Grachev et al. for evolution of grain size with thickness in [26] and is given by:

$$w(t_f) = C\ {t_f}^{\alpha} \qquad \text{III.2}$$

One can easily deduce from equation III.2 that the number of grains $N(t_f)$ per unite area is inversely proportional to thickness probably by $N(t_f) = C(t_f)^{-\gamma}$. Janssen et al [23] found that the number of grains and stress in Cr films obey a power law with the same exponent in equation III.2. Links between grains size, stress and thickness are then found. However, these models do not reveal possible effects of tensile stress on microstructures.

Excessive tensile stress leads to cracking [27,28,29]. The fact that the maximal stress cannot be accurately examined with existing measurement methods, variations of these stresses over thickness are not investigated. In this study, Mo films of type B considered are always cracked. This means that the maximum tensile stress is systematically reached in these films. Therefore, a model which evaluates or takes in account impacts of excessive tensile stress in thin films on microstructure has to be used to expect investigating finely evolution of cracked domains related to maximum tensile stress. To establish this model, the variation of average size of cracked domains (D_{av}) measured from the figure 6 is displayed in figure 7. Symbols are measured data while solid lines represent fitting data.

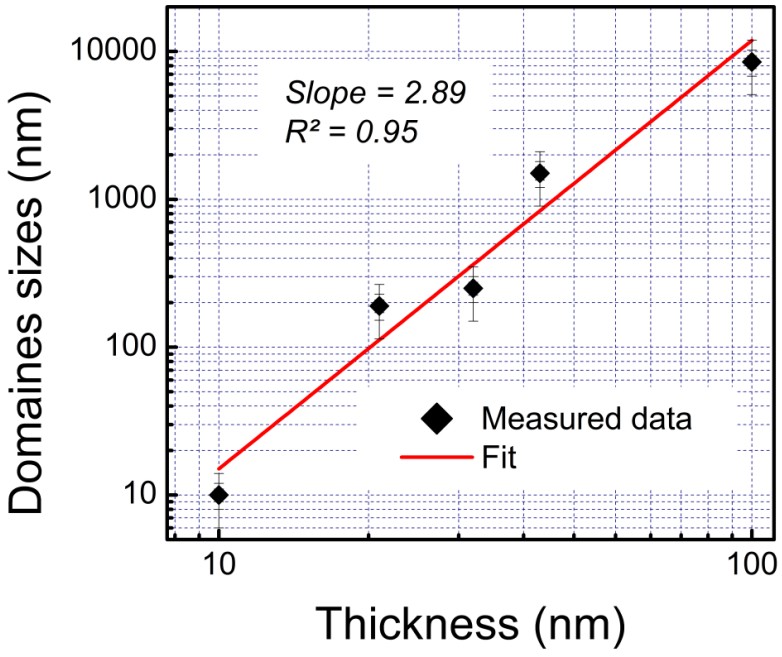

Figure 7: Evolution of size of cracked domains with thickness.

According to our fitting, data can be fitted by analytical model given in equation:

$$D_{av} \infty \zeta(t_f)^{\beta} \qquad \text{III.3}$$

The value of β is around 2.89 while the prefactor ζ is approximately equal to 0.02.The model is close to that previously shown in equation III.2 for the distribution of grain size over thickness. The difference results in value of exponent since current exponent values reported using equation III.2 are lower than unit [30,31]. This could be explained by the fact that both models are based on effect fundamentally different. Indeed, model in equation III.2 deals with evolution of grain size while equation III.3 concerns variation of cracked domains that contains grains. Based on equation III.3, the average size of cracked domains in type B Mo films obeys a power law. An increase in size of cracked domains when the film becomes thicker reveals a change in tensile stress at each thickness. The key question is now to explain how cracked domains are larger in thicker films than in thinner films.

Growth process is shown in figure 8 to illustrate steps of formation of polycrystalline films while process of crystallites coalescence is shown in figure 9. Recent model widely used to explain the tensile stress occurrence in thin films was proposed by Nix and Clemens [32] and is based on coalescence of islands. At coalescence of individual crystallites, the whole energy of the system is lowered by reducing the surface area hence the surface energy. The surface energy arises from difference in nature of bonding between surface and interior atoms in crystallites; atoms at boundaries would have an equilibrium interatomic spacing different from that of interior which are not constrained to remain in atomic registry with underlying lattice. The difference in equilibrium interatomic spacing results in a force per unit length acting on surface of each island, referred as surface stress.

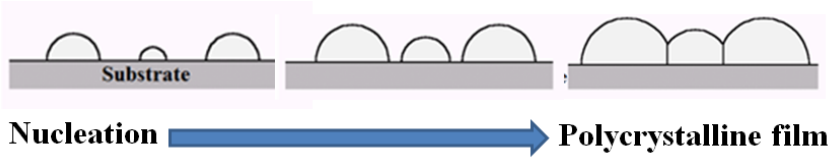

Figure 8: Growth steps of polycrystalline films.

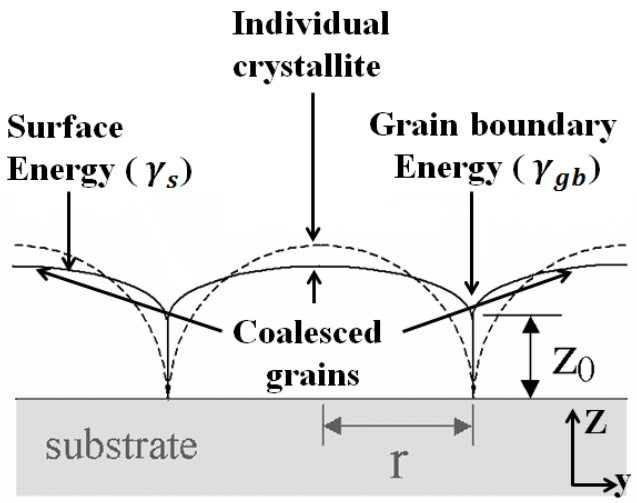

Figure 9: Stresses related to coalescence of crystallites from.

The surface stress can be considered as exerting pressure on finite solid body called Laplace pressure and is equal to difference between the pressure of finite solid and the pressure of surrounding vapor. The surface stress depends on the size of solid and induces a volume elastic strain in the solid.

According to Nix et al. [32], the surface stress is a symmetric tensor with rank two. The average surface stress is related to surface energy (γ_s) of free surface and grain boundaries energy (γ_{gb}) through the expression:

$$\langle\sigma\rangle = \left[\frac{(2\gamma_s - \gamma_{gb})}{r} \times \frac{E}{1-\vartheta}\right]^{1/2} \quad \text{III.4}$$

E is Young's Modulus and ϑ is Poisson's ratio. Another stress that could be responsible to tensile stress exists in thin film; it results from the fact that atoms at grain boundaries exert attractive force over boundaries that lead to displacement in atomic planes. This gives a rise to shrinkage of voids between grains over distance Δ, a fraction of atomic spacing. According to Janssen et al. [23], at each height (h) in the film, this stress can be expressed by:

$$\sigma(h) = \frac{E}{(1-\vartheta)} \times \frac{\Delta}{h} \quad \text{III.5}$$

At a given height, the maximal tensile stress in the film could be reached with gap of shrinkage equal to interatomic distance of unconstrained film and cracking would appear when the gap of

shrinkage exceeds this distance. Energy needed for cracking correspond to energy of decohesion in deposited film, opposite to energy of cohesion. Cohesion energy is an integral over thickness of energy required to break each atomic bond in plane. This energy increases with thickness, all other things equal. Once the maximal average tensile stress is exceeded, the film cracks creating free surface and minimizes the stressing though an increase in surface energy.

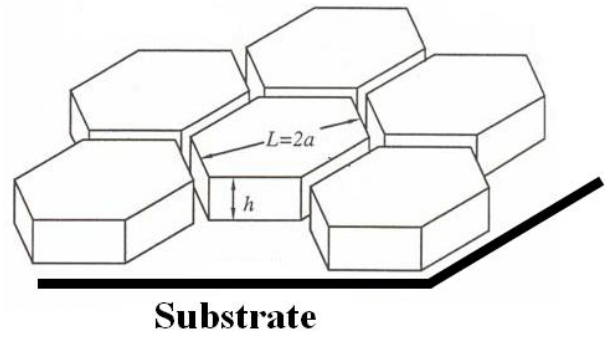

Figure 10: Model to explain evolution of free surface with thickness.

The total free surface generated should be then lower for thinner films and consequently the number of cracked domains in thinner films higher. To check this, we used model in figure 10 where cracked domains are considered as hexagons. The total free surface generated at each height is twice a total surface between hexagons. Considering evolution over thickness of number of cracked domains in our Mo films, we showed that a total free surface (A) generated at each height (t_f) is given by:

$$A = 9.41 \times 10^7 \times t_f\sqrt{t_f} \qquad \text{III.6}$$

The equation III.6 clearly indicates that the total area generated increases with thickness, and is in line with our reasoning and model in equation III.3. The general trend in type B Mo films is that when the film becomes thinner, the number of cracked domains per unity length increase and the domains size decreases as illustrated in figure 11.

$$t_f \searrow \leftrightarrows N \nearrow \leftrightarrows D_{av} \searrow$$

Figure 11: General trend in hard thin films.

III.3.4. Mo bilayers

III.3.4.1. Microstructure and adhesion

Based on the analysis of cracked domains in type B well-adhered Mo films and on adhesion tests, a 300 nm-thick Mo film of type A is combined with a 10 nm-thick Mo film of type B. Figure 12.a and b show SEM images for representative sample of this type of bilayer. No cracking is detected and the microstructure of final bilayer is dictated by the microstructure of the top layer (see figure 2.a). The bilayer additionally passes adhesion test. Thus, this type of Mo bilayer is retained as a solution of back contact for CIGS solar cells and is called S1.

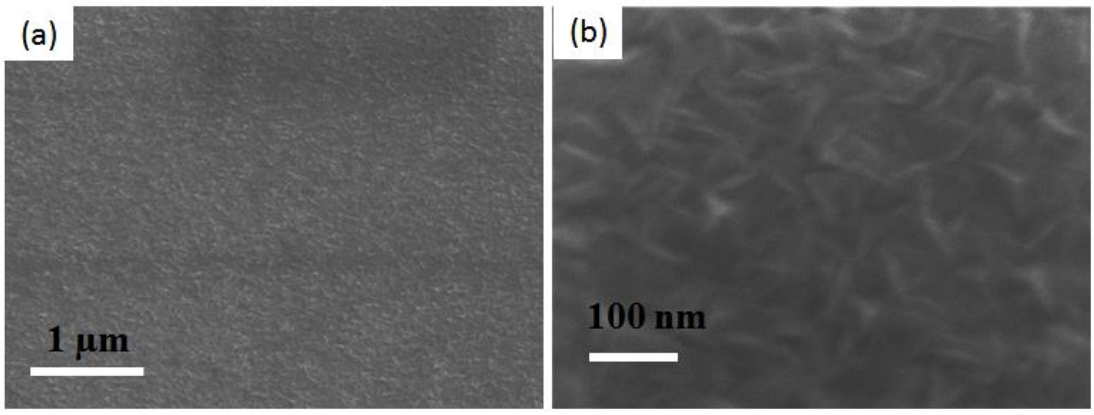

Figure 12: 300 nm-thick Mo film of type A on 10 nm-thick Mo of type B. a) 20.000 X and b) 150.000 X.

One should note however that transitions in pressure between different microstructures found in figure 2 are not absolute and are small enough that accurate measurement of pressure in sputtering chambers could become a problem; the problem can become more critical for industrial processes. A potential problem with films S1 could be a cracking of Mo bilayer if the top layer is deposited at a pressure close to that of type B films. To bypass the problem of pressure control and to ensure good adhesion, further optimization of well-adhered type B Mo films is explored.

Thus, a special attention is paid to growth of Mo films of type B onto the heated substrates. A. Debelle et al. reported that annealing can reduce the tensile stress in Mo thin films [33]. The heating of growing film can in turn modify the microstructure by improving the mobility of arriving atoms on substrate. Series of 300 nm-thick Mo films are then deposited. The temperature of substrate is kept constant at 550 °C during film growth; this corresponds to a

homologous temperature of 0.2. SEM images of surface morphology and cross section of representative sample are shown in figures 13.a and b. Based on the Thornton zone model, the resulting Mo films should be considered as zone 1 type microstructure. Such microstructure normally consists of columns separated by voids with a rough surface. As it can be observed, our Mo films are well crystallized with remarkably facetted grains. The microstructure of these films is dense and grains are definitely larger than that obtained within all others deposition conditions (see figure 2). Surprisingly, films are continuous without any cracks as it can be checked in the low magnification image in figure 13.a. Cross-sectional SEM image also clearly shows that Mo films are arranged in columns (figure 13.b). No evidence of voids between grain boundaries can be observed and this indicates that this type of Mo film is absolutely compact. The contrast with microstructure B type films is obvious. It is clear that higher substrate temperature during growth definitely enhances the microstructure of our films. The absence of cracking is attributed to stress reduction in these films and the densification could be attributed to enhancing in mobility.

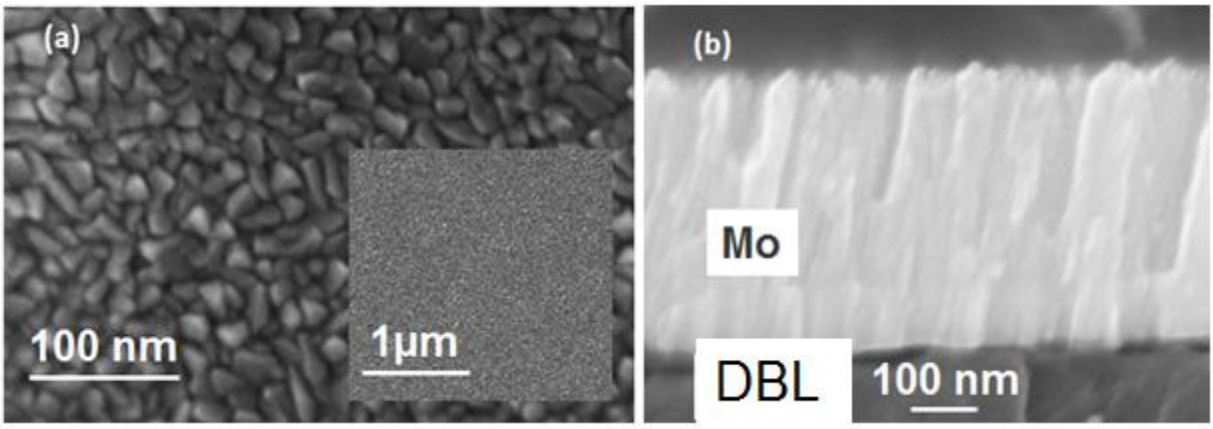

Figure 13: Sputtered Mo films deposited onto substrate heated up to homologous temperature of 0.2. a) The surface morphology and b) Cross-sectional SEM image of the corresponding Mo films.

The problem with this type of films is that adhesion is unfortunately weakened and most films fail the adhesion test. To solve this problem, two steps deposition at fixed pressure is adopted. The first step consists in depositing a 10 nm-thick Mo film deposited at around 5.5×10^{-1} Pa and at room temperature followed by heating to 550°C. Next, a 300 nm-thick Mo film is deposited at the same pressure onto the first layer, at 550 °C. The microstructure of the resulting bilayer is identical to that shown in figure 13 and films moreover pass the adhesion test. The

sheet resistance of this bilayer is less than 0.25 *Ω*/square, two times lower than the sheet resistance of bulk Mo and is by far the best value for our Mo films. This type of Mo bilayer is retained as the second solution for Mo back contact for CIGS solar cells and is named S2.

III.3.4.2. Light reflectance

Reflectivity of back contact is an important parameter for the efficiency of CIGS solar cells. Generally, decreasing the thickness of absorbing layer used in thin film technologies reduces absorption of sun light. Some of the light reflected from the back contact is absorbed as it travels towards the top surface. Increasing the reflectivity of the back contact causes more light to be absorbed hence increases solar cell efficiency.

Figures 11.a and b show the total reflectance (R_T) of microstructure B, S1 and S2 type Mo films. Reflectance is constant in the visible spectrum for all Mo films. R_T of 50 % can be reached in the visible spectrum with microstructure B films. R_T of S1 and S2 are quite similar with 55 % reflectance in the visible spectrum. In infra-red region, total reflectance increases monotonously for all Mo films. R_T of S2 and S2 are still similar but both are higher than that of microstructure B type films. The gap in R_T is approximately 5 % in visible; it can reach 10 % in infra-red.

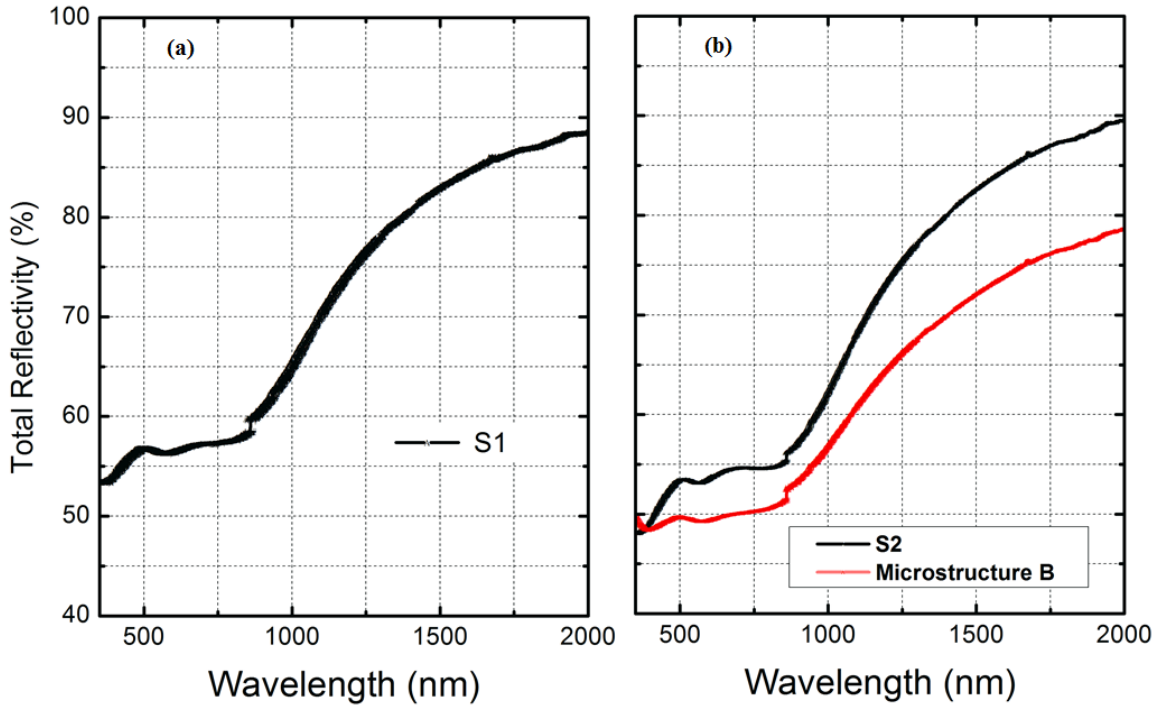

Figure 14: Evolution of the total reflectance of (a) S1 based bilayer and (b) microstructure B and S2.

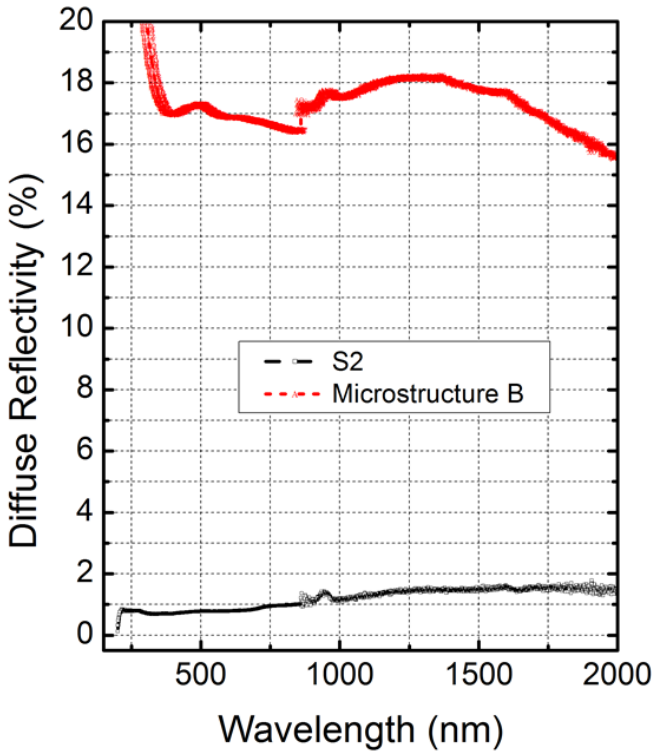

Figure 15: Diffuse reflectivity of microstructure B films compared with that of S2 based M bilayer.

Normally, the total reflectance of opaque films will depend only on the nature of material. Thus, the result reveals that, even if Mo films are well-crystallized after annealing (S2 based films), the surface roughness of S1 and S2 are probably comparable and the surface of both bilayers should be different than that of microstructure B films. The decrease in R_T for type B films can be related to absorption of light in cracks previously identified in SEM and AFM for this type of Mo films. To highlight cracking and evaluate their impacts on reflectivity, diffuse reflectivity of type B and S2 films is measured (figure 12). Diffuse reflectivity is ten times higher for type B films compared to S2 bilayers. As an example, at 750 nm, diffuse reflectance of S2 based films is around 1 % while that of type B films is more or less 17 %. The fact that the diffuse reflectivity is less than 1 % in the visible for S2 is a signature of very smooth surface while the important gap recorded for type B films can be attributed to the loss of light reflectance in cracks probably due to the multi-reflection. [34]

In summary, both low pressure (which gives highly energetic arriving particles) and the heating of substrate during films deposition (which confers high mobility to adparticles) reduce tensile stress in our Mo films and lead to compact and smooth films. The comparison of reflectance of

different Mo films reveals the potential of optical characterization for the classification of microstructures.

III.4. Summary

Microstructures of Mo films prepared on ZN200 based polysilazanes DBL were investigated and influence of sputtering parameters such working pressure and substrate temperature has been identified. By varying the working pressure from 2.6 x 10^{-1} Pa to 2.6 Pa, transitions in Mo film microstructures were observed and four different microstructures were identified. It was observed that Mo films become less dense with an increase of deposition pressure. At the same time, the sheet resistance is increasing with the total pressure. This evolution of sheet resistance is attributed to increasing in porosity at higher working pressure; it is suggested that this may in fact be due to enhanced oxidation of porous films. Otherwise, it was found that the microstructure of Mo films is remarkably improved and cracks completely disappear when films are deposited at 550°C. Resulting films are compact, columnar-like and continuous with facetted grains. This type of Mo films and Mo films deposited at low pressure exhibits very low sheet resistance but do not adhere well to ZN200 coatings. Well-adhered films are often cracked and efforts have been made for understanding evolution of cracked domains with thickness, which is shown to follow a power law. The study allows us to establish a method to produce crack-free and well-adhered films. Two solutions have been obtained by combining well-adhered (type B) with either 300 nm-thick of Mo films deposited at low pressure (named S1) or 300 nm-thick of Mo films deposited on heated substrates at a pressure identical to type B films (called S2). S1 and S2 pass adhesion test and exhibit very low sheet resistance required for Mo back contacts.

References

[1] Chia-Hua Huang, Hung-Lung Cheng, Wei-En Chang, Ming Yi Huang and Yi-Jiunn Chien Semicond. Sci. Technol. 27 (2012) 115020.

[2] John H. Scofield, A. Duda, D. Albin, B.L. Ballard, P.K. Predecki, Thin Solid Films 260 (1995) 26/31.

[3] F. A. Abou-Elfotouh, L. L. Kazmerski, T. J. Coutts, R. J. Matson, S. E. Asher, A. J. Nelson, and A. B. Swartzlander-Franz, Journal of Vacuum Science and Technology (A) 7, 837-841 (1989).

[4] R.J. Matson, O. Jamjoum, A.D. Buonaquisti, P.E. Russell, L.L. Kazmerski, P. Sheldon, et al., Solar Cells 11 (1984) 301.

[5] D. W. Niles, A. J. Nelson, C. R. Schwerdtfeger, H. Höchst, and D. Rioux, Mat. Res. Soc. Symp. Proc. 260, 299 (1992).

[6] M. Jubault, L. Ribeaucourt, E. Chassaing, G. Renou, D. Lincot, F. Donsanti, Solar Energy Materials & Solar Cells 95 (2011) S26–S31.

[7] R.A. Hoffman, J.C. Lin et J.P. Chambers, Thin Solid Films, 206, 1991, 230.

[8] G.C.A.M Janssen, Thin Solid Films, 6654/6664 (2007) 515.

[9] Y. Pauleau, Vacuum 175/181 (2001) 61.

[10] M. Pellicone, T. Karabacak, T.-M. Lu, Phys. Rev. Lett. 96 (2006) 146105.

[11] S. Mahieu, P. Ghekiere, D. Depla, R. De Gryse, Thin Solid Films 515 (2006) 1229/1249.

[12] J. Detor, A. Hodge, E. Chason, Y. Tinmin, H. Xu, M. Conyers, A. Nikroo, A. Hamza, Acta Materialia, 175-171 (2009) 57.

[13] J. A. Thornton, J. Vac. Sci. Technol. A 4 3059/3065 (1986) 6.

[14] Petrov, P.B. Barna, L. Hultman, J.E. Greene, J. Vac. Sci. Technol. A21 (2003) S117.

[15] F. Tang, T. Karabacak, P. Morrow, C. Gaire, G-C. Wang, T-M. Lu, Phys. Rev. B. 72 (2005) 165402.

[16] P.M.P. Salome, J. Malaquias, P.A. Fernandes, A.F. Da Cunha, J. Phys. D: Appl. Phys. 43 345501-1 (2010) 345501/7.

[17] R. C. Cammarata, T. M. Trimble, J. Mater. Res., 15 (2000) 11.

[18] R.C. Cammarata, Prog. Surf. Sci. 46 (1994) 1.

[19] B.A. Movchan, A.V. Demchishin, Fiz. Met. Metalloved 28 (1969) 83.

[20] P.B. Barna, M. Adamik, Thin Solid Films 317 (1998) 27.

[21] Petrov, P.B. Barna, L. Hultman, J.E. Greene, J. Vac. Sci. Technol. A21 (2003) S117.

[22] F.A. Doljack, R.W. Hoffman, Thin Solid Films 12 (1972) 71.

[23] G.C.A.M. Janssen, A.J. Dammers, V.G.M. Sivel, W.R. Wang, Appl. Phys. Lett. 83 (2003) 3287.

[24] G.C.A.M. Janssen, F.D. Tichelaar, C.C.G. Visser, J. Appl. Phys. 100 (2006) 093512.

[25] T. J. Vink, M. A. J. Somers, J. L. C. Daams, A. G. Dirks, J. Appl. Phys. 70 (1991) 4301/4308.

[26] S. Yu. Grachev, F.D. Tichelaar, G.C.A.M. Janssen, J. Appl. Phys. 97 (2005) 073508.

[27] A. Bagchi, A.G. Evans, Interface Sci. 3 (1996) 169.

[28] M.W. Moon, H.M. Jensen, J.W. Hutchinson, K.H. Oh. A.G. Evans, J. Mech. Phys. Solids 50 (2002) 2355.

[29] R. Abermann, R. Kramer, J. Mäser, Thin Solid Films 52 (1978) 215.

[30] S. Yu. Grachev, F.D. Tichelaar, G.C.A.M. Janssen, J. Appl. Phys. 97 (2005) 073508..

[31] M. Pellicone, T. Karabacak, T.-M. Lu, Phys. Rev. Lett. 96 (2006) 146105.

[32] W.D. Nix, B.M. Clemens, J. Mater. Res. 14 (1999) 3467.

[33] A. Debelle, G. Abadias, A. Michel, C. Jaouen, and V. Pelosin, J. Vac. Sci. Technol. A 25,. 1438 (2007), http://dx.doi.org/10.1116/1.2771554.

[34] Xia D. He, Computer Graphics, 25 (1991) 4.

CHAPTER 4
Molybdenum/ZN200/Steel Interface Analysis

IV.1. Introduction

Mo films must adhere well to ZN200-based DBL which itself must adhere well on SS even under stress if they are to be used as part of CIGS-based photovoltaic modules. Polysilazane based ZN200 coatings prepared on both AISI316 and AISI430 stainless steels (SS) as insulating DBL for CIGS usually pass the standard adhesion test even after being annealed up to 550°C. The key question is to understand how this material adheres well on steel substrates. In this chapter, we discuss chemical interactions between both types of steel and polysilazanes precursors and their effect on adhesion. X-ray Photoelectron Spectroscopy (XPS) and Infrared Reflection Absorption Spectroscopy (IRRAS) are used to probe different interfaces. Prior to interface analyses, the chemical composition of steel surfaces is analyzed to determine which chemical functional groups promote adhesion. In a second part, we address interaction between Mo and ZN200 coatings in the case of both good and bad adhesion, as previously discussed in the chapter III [1].

IV.2. Sample preparation and characterization

The chemical composition of AISI316 and AISI430 SS substrates is summarized in table 1. Each steel substrate is cleaned using the procedure described in section II.2.1.2 before the deposition of ZN200 coatings.

Table 1: Compositions (wt. %) of AISI316 and AISI430 SS used as substrates.

Stainless steel	Fe	C	Cr	Ni	Mo	Mn	Si
ASI316	65	0.05	16 - 17	10 – 12.5	2 – 2.5	2	0.03
AISI430	80	0.12	16 - 18	0.5	0.2 – 0.6	1.5	1-8

Mo films with microstructure A and Bh (poor adhesion), and microstructure B (good adhesion), as discussed in chapter III, are then deposited on ZN200 for the interface analysis.

A Thermo VG-Scientific Sigma Probe spectrometer with an Al Kα source (1486.6 eV) was used for XPS analysis. The photoelectron take-off angle is 45°. Thermo Avantage 4.7 V data acquisition and analysis software was used to record XPS spectra and to process data. Energy calibration was performed by centering the C-C contribution of the C 1s peak at a binding energy of 284.6 eV. The energy resolution was 1 eV at pass energy of 200 eV for survey scans and 0.5 eV at pass energy of 50 eV for high resolution scans. XPS depth profiles of uncoated substrates and of Mo/ZN200 interfaces were recorded by alternating cycles of XPS analysis and sputtering using an argon ion beam (3 keV, 1 µA) incident at 45° with a spot size of 200 × 200 μm^2. AFM (in tapping mode) was used to check for cracks in the ultra-thin Mo films.

IRRAS analyses of SS coated with ZN200 were performed from 400 to 2000 cm^{-1} using NEXUS spectrometer.

IV.3. Part I: polysilazane and steel interface analysis

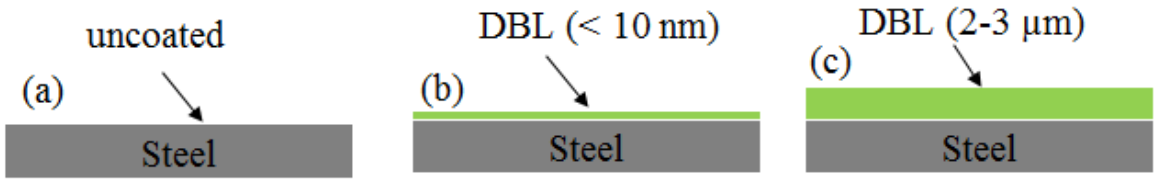

Figure 1: The three samples used for ZN200 and SS substrates interface analysis. a) Uncoated steel, b) steel coated with ultra-thin coating of ZN200 to probe the interface without modifications directly and c) steel coated with the thicker ZN200 coating.

Three samples were prepared for each type of steel substrate as shown in the figure 1. Fe 2p, Cr 2p, O 1s, and Si 2p core level peaks were measured on uncoated steel and compared with steel surfaces modified by an ultra-thin ZN200 coating (thinner than 10 nm to probe the interface directly without modifications). O 1s and Si 2p spectra were also collected on ZN200 coatings (2 - 3 µm-thick film of ZN200 prepared on each SS substrates). As our ZN200 coatings have to be thermally stabilized at 500°C to complete the deposition of Mo films successfully, steel substrates coated with ultra-thin ZN200 films and annealed up to 550°C have also been analysed.

IV.3.1. Preliminary study

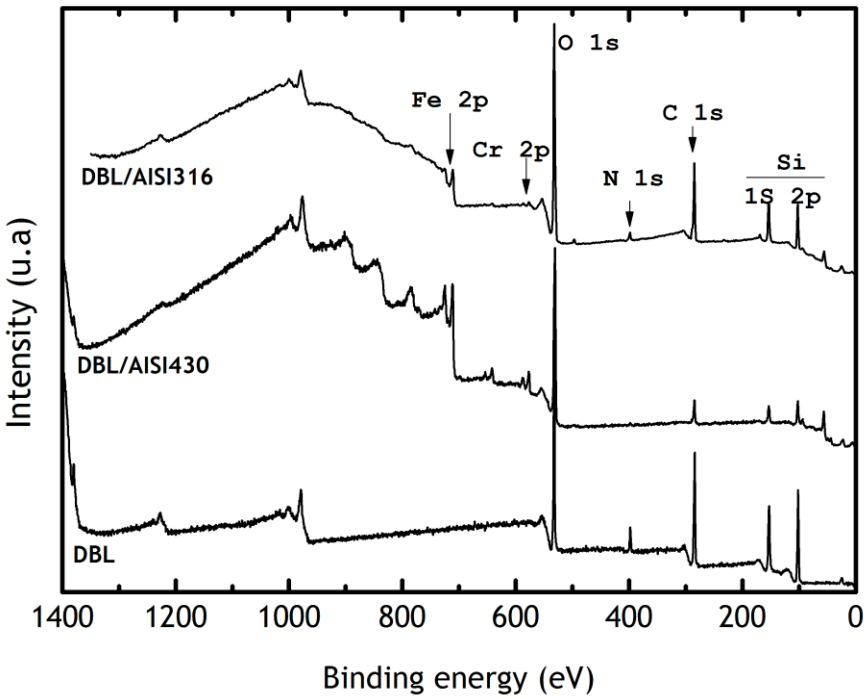

Figure 2: Survey spectra performed on ZN200 = DBL, and both AISI316 and AISI430 coated with ultra-thin ZN200 coatings.

To compare chemical environments in the three samples, a preliminary analysis is to check if one can detect the steel substrate through the ultra-thin polysilazanes coatings. Thus, XPS survey spectra for polysilazane and those of the two steel substrates coated with ultra-thin polysilazane are displayed in the figure 2. Cr 2p and Fe 2p peaks are clearly seen; they are related to the substrate, as PSZ does not contain these elements. Similar results were obtained with the survey spectra recorded on annealed steel substrates coated with ZN200 ultra-thin films. By comparing atomic transitions in unmodified samples with these modified by PZS based ZN200 precursors, one can determine the chemical interactions between these materials.

For this purpose, once the top surface of our steel substrates is well understood, the chemical states of Cr, Fe, O and Si atoms elements will be recorded in each sample and compared.

IV.3.2. Composition of the top surface of steel substrates

XPS depth profiles have been performed on uncoated SS substrates to obtain the relative atomic concentration of species in each SS substrate. The depth scales are calibrated using sputter rate of

iron. The intersection of the oxygen line with those of Fe and Cr allows us to estimate the thickness of the native oxide layer (also called passivation layer) which should be present on the top surface of steel. Figure 3 shows the atomic concentration of main atoms in AISI316 and AISI430. As can be checked, the thickness of the native oxide layer on both substrates is around of 2 - 3 nm/eq.Fe.

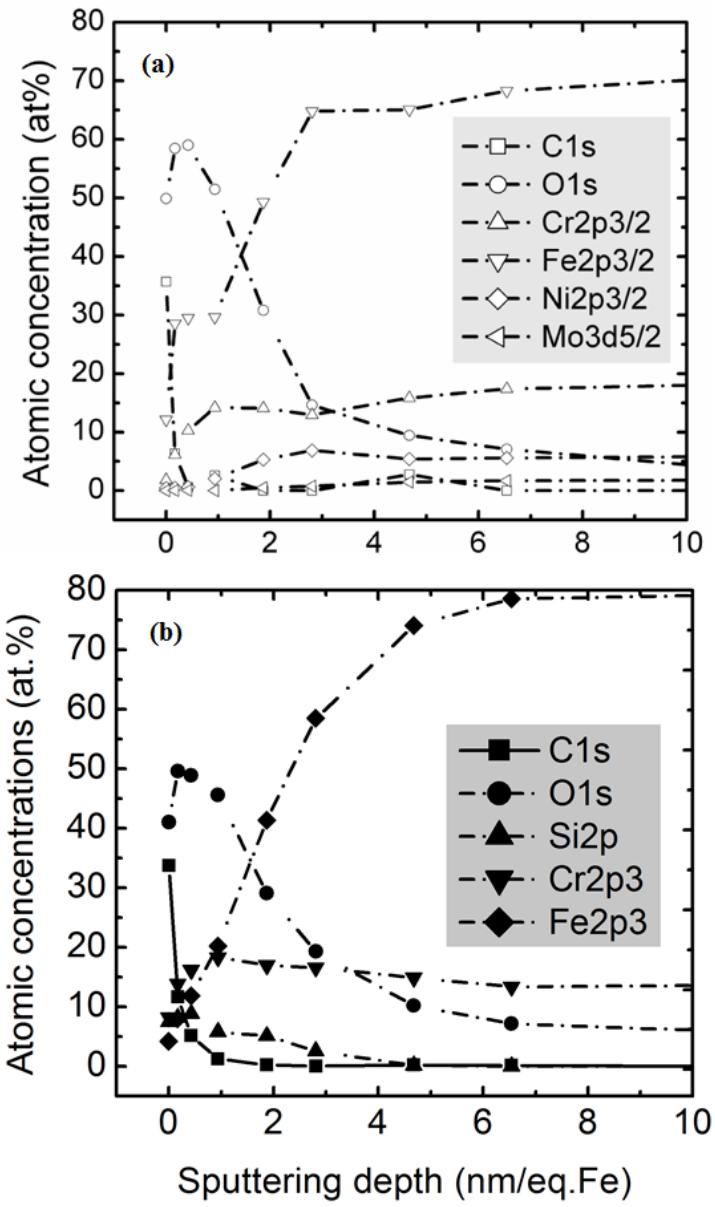

Figure 3: Atomic concentration in cleaned and uncoated (a) AISI316, and (b) AISI430 stainless steels.

These results are in accordance with values currently reported for Fe-Cr alloys [2-3]. In the bulk AISI316, Fe concentration is 3-5 at.% above the stoichiometric composition while Ni

concentration seems to be 5 at.% lower. The concentration of Cr in bulk for both types of steel is in agreement with the literature (see table 1).

To evaluate the distribution of the main oxides in the passivation layer, e.g.: AISI316 substrate, the concentrations of iron, chromium and nickel are plotted in figure 4. A concentration gradient is clearly observed. The outer region of the passivation layer is enriched in iron; a strong enrichment of chromium is observed in the center of the passivation layer while enrichment in Ni is found for the region close to the interface with the metal. This is in agreement with some published reports [3,4] and can be attributed to a double-oxide stratification of both Cr_xO_y and Fe_xO_y being present at the top surface of the native oxide.

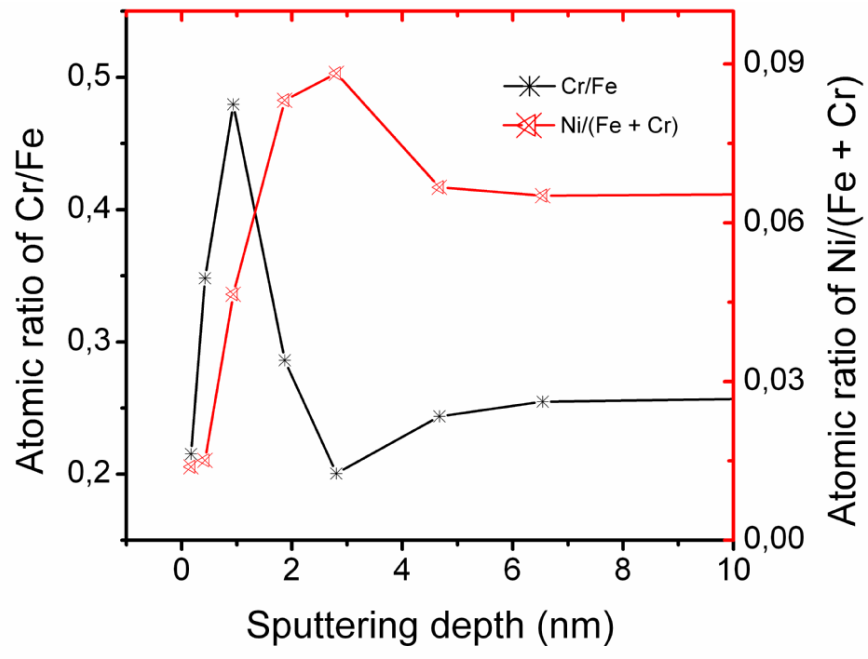

Figure 4: Enrichment of Cr, Fe and Ni in the passivation layer calculated from raw data for AISI316.

In some previous studies [5,6], Cr enrichment was however observed at the top surface of stainless steels. To try understanding this, we have listed in table 2 the values of Gibbs' free energy of formation for different oxides which could be present on the top surface of SS substrates. By comparing these values, it can be found that Cr_2O_3 (hematite) should be the favored species initially formed on the surface as reported in [7,8,9]. In addition, it has been reported in [9] that Cr can easily diffuse trough the ferrite matrix to form Cr_2O_3 oxide on the top surface. Thus, one can reasonably exclude the effect of stratification of Fe_xO_y/Cr_xO_y oxides in

the passivation layer and consider that both oxides could simultaneously be present at the top of the surface.

Table 2: Gibbs free energy of formation of main oxides formed within the passivation layer on stainless steels.

Type of oxide	- ΔGr(KJ/mol)			
	25°C		700°C	
FeO	245.84	[6]	201.88	[6]
Fe_3O_4	1017.83	[6]	802.52	[6]
Fe_2O_3	742.33	[6]	569.39	[6,8]
$FeCr_2O_4$	-	[6]	214.00	[7]
Cr_2O_3	1059.14	[6]	881.98	[6]
CrO_2	543.83	[6]	425.21	[6]
CrO_3	505.46	[6]	-	-
NiO	238.39	[6]	151.78	[6]

For further understanding of the surface of our steel substrates, both spectral regions of Cr $2p_{3/2}$ and Fe $2p_{3/2}$ are shown in figure 5. Spectra from the passivation layer consist of two overlapping peaks, one due to the metal in its oxide form at higher binding energy and the other one representing the metallic form at the lower binding energy. The metallic peaks are small compared to the much stronger oxide peaks. The fact that the pure metallic forms are detected through the passivation layer suggests that the latter is thinner than 10 nm. Cr oxide seems to extend deeper than Fe oxide: Cr is detected over 12 sputtering cycles while Fe oxide disappears after the 5^{th} sputtering cycle. In accordance with the literature, Ni is not detected at the surface of the sample [7,9].

These results imply that chromium and iron oxides probably coexist within the passive layer as reported in [9]. We speculate then that the passivation layer should be constituted of a solid solution of iron and chromium oxides; no evidence was detected of nickel oxides during the first etching steps even if steel clearly contains nickel. A comparison of Cr $2p_{3/2}$ and Fe $2p_{3/2}$

transitions in depth profiles indicates that Cr is still present in its oxide form while Fe is detected in its metallic form.

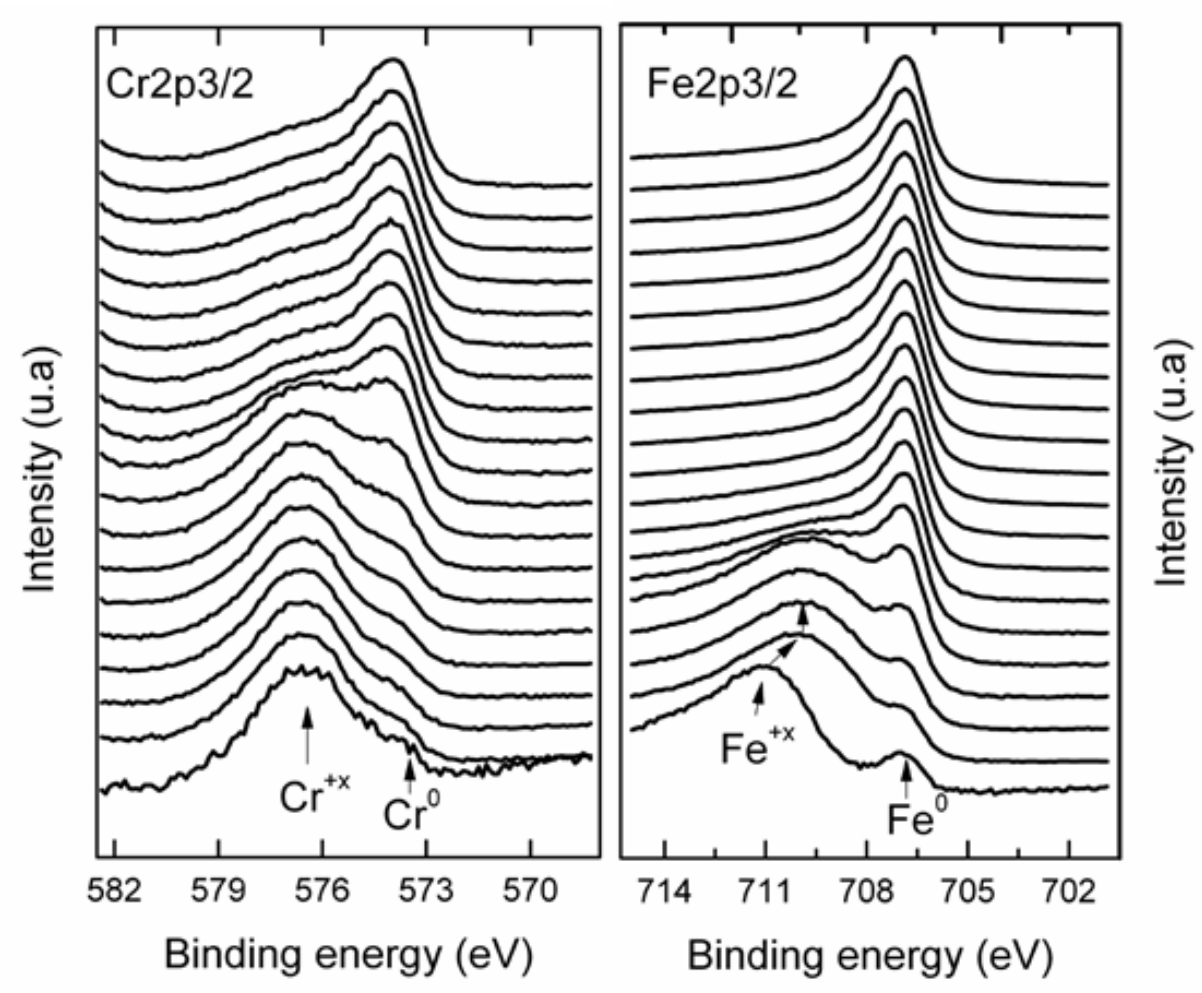

Figure 5: Successive XPS depth spectra of Cr 2p (left) and Fe 2p (right) transitions. From bottom to top spectra correspond to the surface toward the bulk.

IV.3.3. XPS analysis of the interface between ZN200 and steel

Figures 6 shows Fe and Cr transitions recorded on AISI316 substrates coated with crosslinked ZN200 ultra-thin films, before and after annealing at 550°C. Spectra from uncoated AISI316 substrates are shown for reference. As it can be observed, peaks of Cr $2p_{3/2}$ transition are centered at 576.5 eV for all samples, corresponding to oxidized chromium. A shoulder at lower binding energy, around 574 eV, is observed for all samples and corresponds to elemental chromium (Cr^0). Similar results have been also obtained on AISI430 as shown in figure 7.

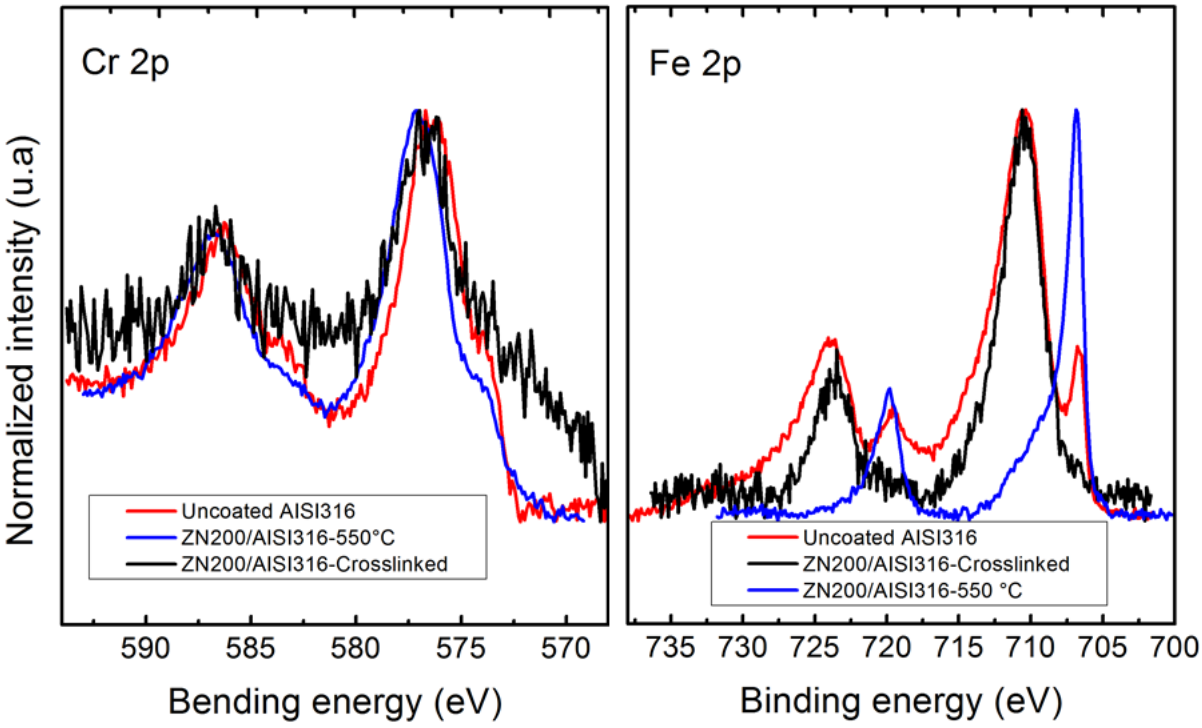

Figure 6: Comparison of chromium (left) and iron (right) transitions in uncoated AISI316, AISI316 coated with crosslinked ZN200 ultra-thin films and AISI316 coated ZN200 ultra-thin films annealed up to 550°C.

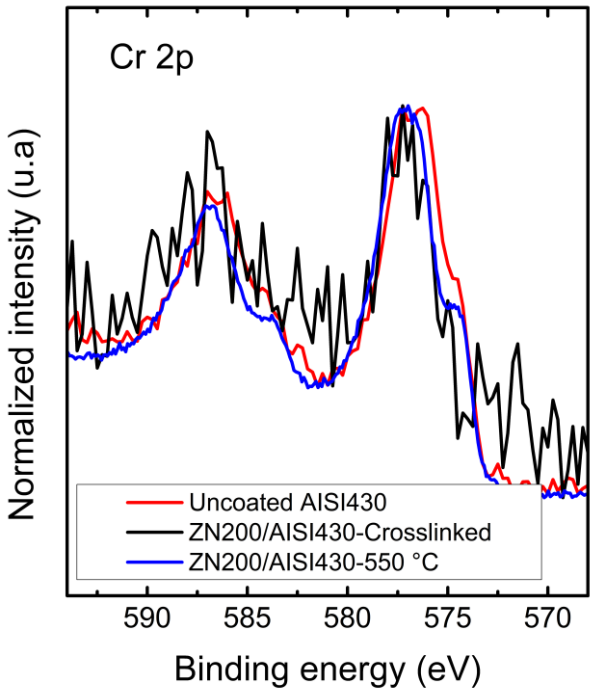

Figure 7: Comparison of chromium transitions in uncoated AISI430, and non-annealed and annealed AISI430 coated with crosslinked ZN200 ultra-thin films samples.

The Fe 2p transition in uncoated steel is a contribution from metallic and oxidized Fe. In the case of non-annealed ZN200 ultra-thin films on AISI316, the Fe 2p spectrum is dominated by the peak from the oxidized state, while the peak from elemental Fe is predominant in AISI316 coated with ZN200 and annealed at 550°C.

Detailed analysis of these XPS spectra should help to identify chemical reactions between polysilazane precursors and steel substrates. One expects polysilazane precursors (-Si-HN-Si-) to react with the hydroxide functional groups on the top surface to form Fe-O-Si and Cr-O-Si bonds [10,11,12]. After fitting (see figure 9) the spectra from AISI316 surfaces due to the smaller number of peaks, we conclude that Cr $2p_{3/2}$ and Fe $2p_{3/2}$ core levels include Cr_2O_3, Fe_2O_3 and Fe_3O_4 oxides as well as $(Fe(OH)_2)$ and $Cr(OH)_3$. The corresponding binding energies are listed in table 3.

Table 3: Binding energy of Cr $2p_{3/2}$ and Fe $2p_{3/2}$ used for peak fitting.

Species	Binding energy (eV)	Reference
Cr_2O_3	576.1 eV	[13]
$Cr(OH)_3$	577.5	[9]
Fe_2O_3	710.75	[14]
Fe_3O_4	709.4	[14]
$(Fe(OH)_2)$	709.7	[9]

Hydroxide peaks are much smaller than oxide peaks for both Fe and Cr. Hence it is not surprising that the deposition of ZN200 does not cause drastic changes of the Cr and Fe peak shapes. At this point, peak fitting confirms the presence of hydroxides on AISI316 surfaces. Moreover, at least in the case of Fe 2p, one can conclude from figure 6 that the deposition of ZN200 polysilazane reduces the amount of hydroxides, in line with previous investigations in [13,14].

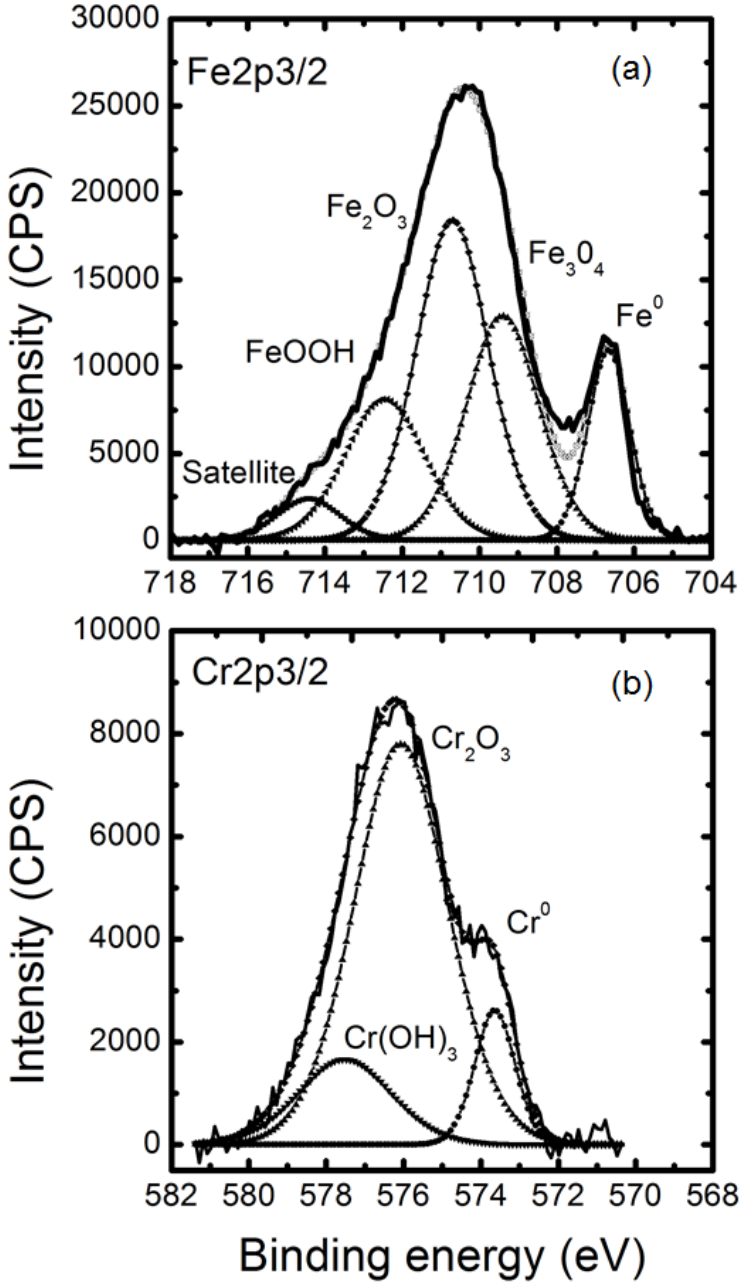

Figure 8: Fitting of (a) Fe2p and (b) Cr 2p transitions on the top surface of the uncoated AISI316 substrate.

Furthermore, Si 2p and O 1s transitions from the three previous samples are compared with those from pure ZN200 coatings (figure 10). The main component of O 1s transition in ZN200 is at 532.1 eV and is attributed to Si-O-Si bonds [15]. Spectra of O 1s from AISI316 modified with ultra-thin ZN200 coating (before and after annealing) have their main peak centered at 532.6 eV which is attributed to SiO_2 [16]. The shoulder at lower binding energy, near 530.3 eV, could be a contribution of Me-O-Si [17,18]. Although overlap with peaks from FeOOH and $Cr(OH)_3$

hydroxides can lead to confusion, the absence of contribution from elemental Fe and Cr in spectra from non-annealed steel coated with ZN200 ultra-thin film (figure 6) is consistent with the suggestion that Me-O-Si bonds are formed at the interface.

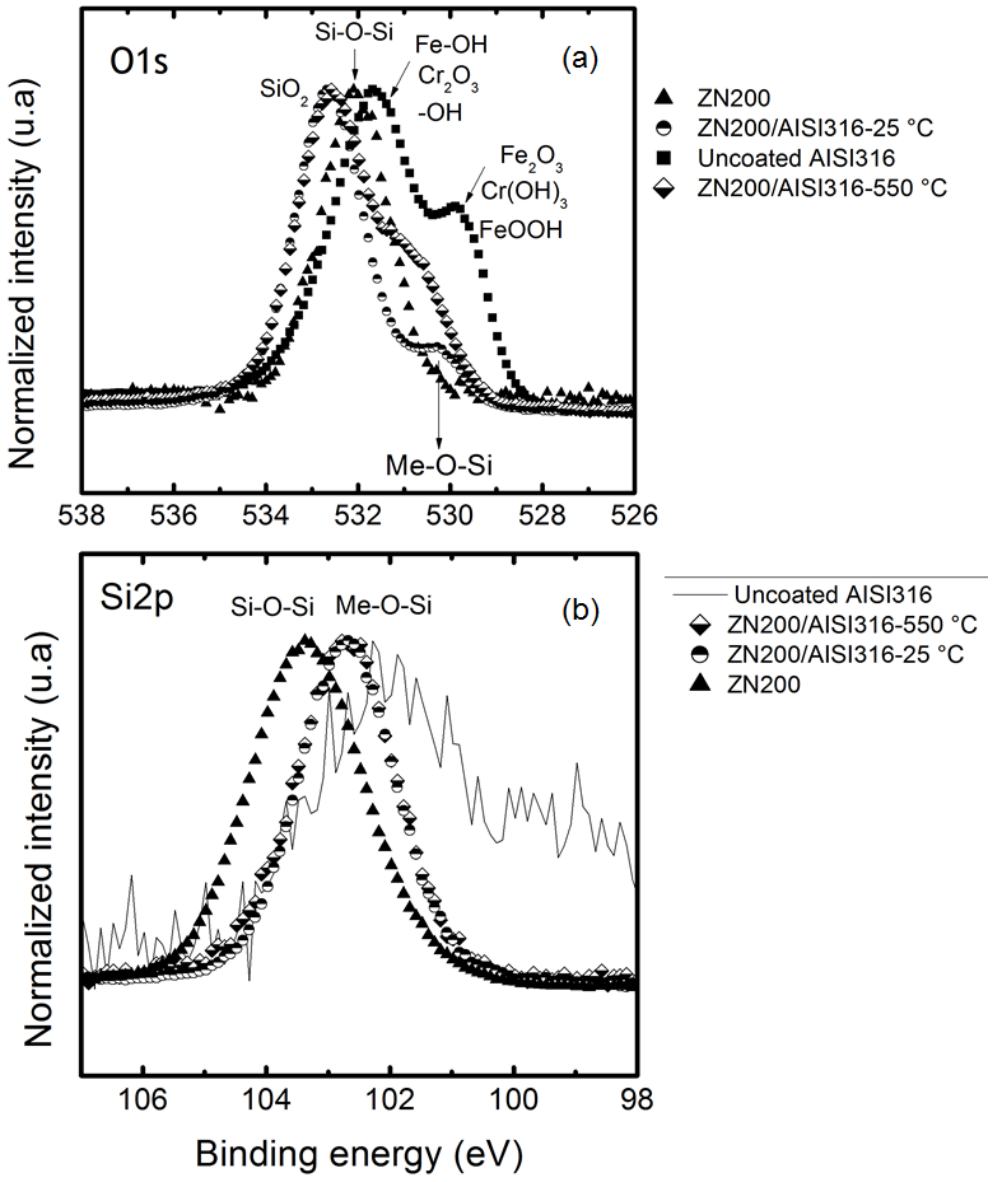

Figure 9: Comparison of O 1s and S i2p transitions in uncoated AISI316, ZN200 coating, non-annealed and annealed (550 °C) AISI316 coated with ultra-thin ZN200 samples.

In Si 2p transitions, three main observations can be made:

- The amount of silicon on the surface of AISI316 is very small;

- The main peak detected in pure ZN200 is centered at 103.4 eV and is assigned to Si-O-Si bonds [19].
- Annealing of ZN200 on AISI316 has almost no effect on Si 2p spectra, but the binding energy of Si 2p in thin ZN200 on AISI316 is about 0.7 eV lower that in pure ZN200. We suggest that this is due to the formation of Fe-O-Si and Cr-O-Si bonds.

O 1s transitions in samples performed on AISI430 are otherwise compared as shown in the figure 11. Peaks at 532 eV and 531 eV binding energies assigned to Si-O-Si and Me-O-Si respectively are detected on uncoated AISI430. This could rise from the fact that AISI430 contains much higher amount of Si compared to AISI316 where these peaks were not found. The peak of Mo-O-Si is probably a contribution of both Cr-O-Si and Fe-O-Si species. Both peaks are detected in AISI430 modified with ZN200 even after annealing.

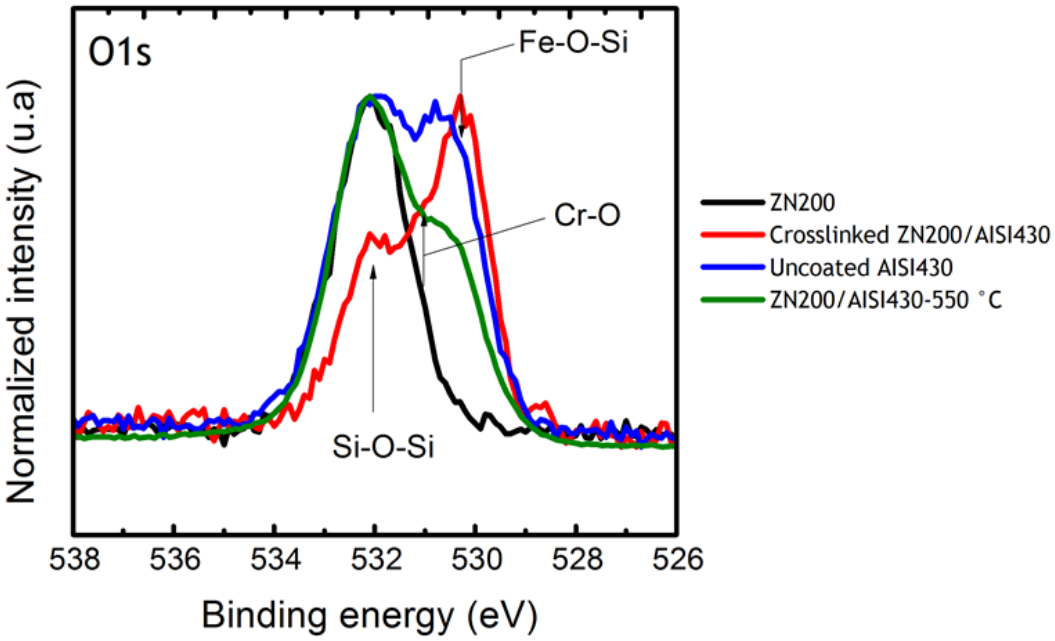

Figure 10: High resolution XPS spectral analysis of O 1s transition in AISI430 based samples.

In summary, covalent bonds (metallosiloxanes) are detected at the interface between ZN200 precursors (polysilazane) and steel substrates.

IV.3.4. IRRAS analysis of interface between ZN200 and steels

To complement XPS results, IRRAS analysis has been recorded to investigate chemical interactions between ZN200 coatings and both AISI316 and AISI430 substrates. Two different

samples are considered for each steel substrate. The first sample is ZN200 coating (steel coated with thick ZN200 (2 - 3µm) in order to detect ZN200 coating only) and the other sample is steel coated with ultra-thin ZN200 to allow the detection of the steel surface through ZN200. Results are shown in figure 12 and 13. Vibrational peaks previously found in ATR (see chapter 2) are present and are in accordance with published reports [20,21]. The spectral range between 750 cm^{-1} to 500 cm^{-1} is especially interesting because peak at 615 cm^{-1} and a shoulder near 700 - 730 cm^{-1} are observed on only steel surfaces modified by the ultra-thin film. These peaks are respectively assigned to Fe-O-Si [22,23] and Cr-O-Si bond [24].

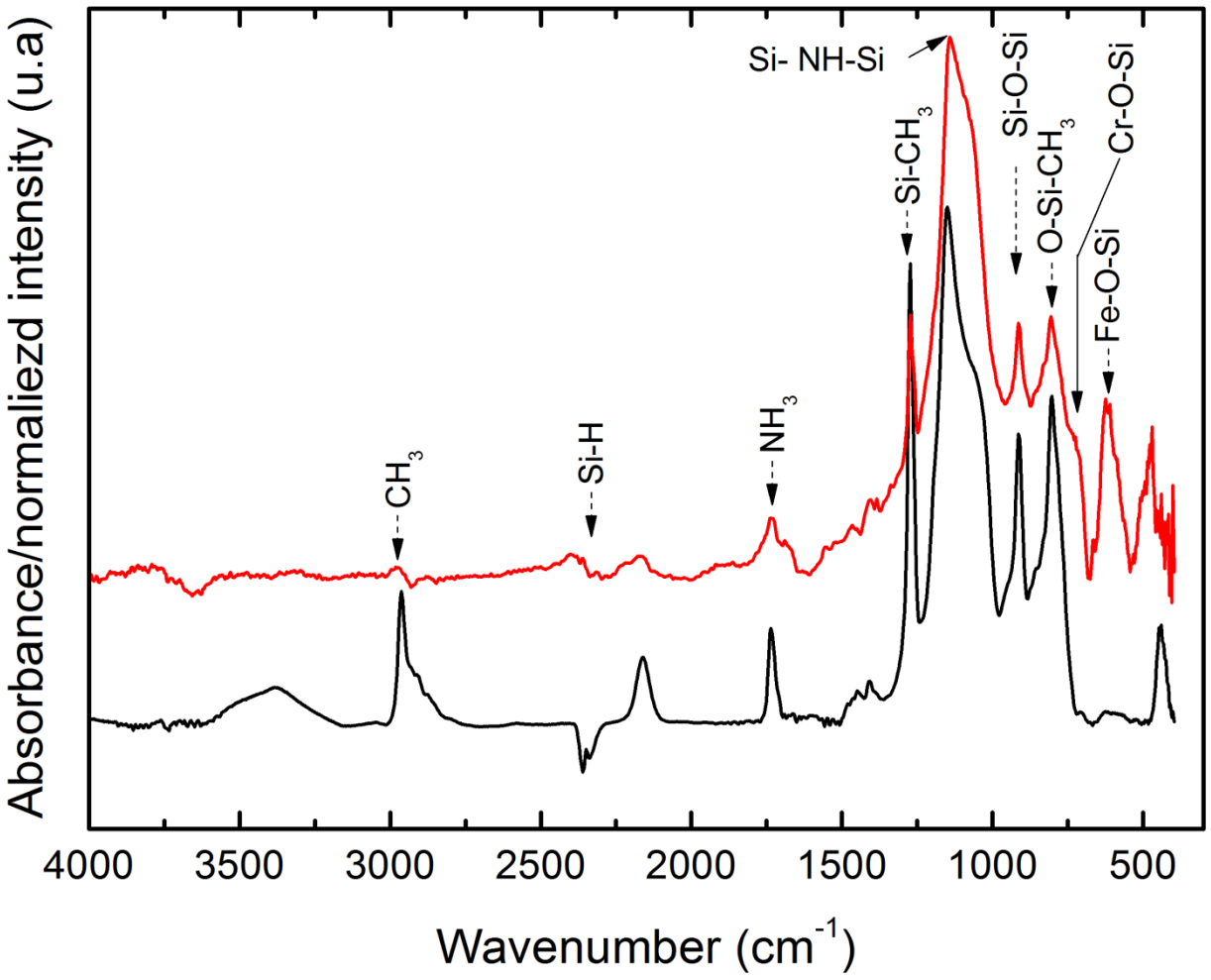

Figure 11: Comparison of IRRAS spectra on AISI316. In black color is shown a spectrum of pure ZN200 coating while the surface of AISI316 modified by ZN200 ultra-thin film (less than 10 nm-thick) is presented in red color.

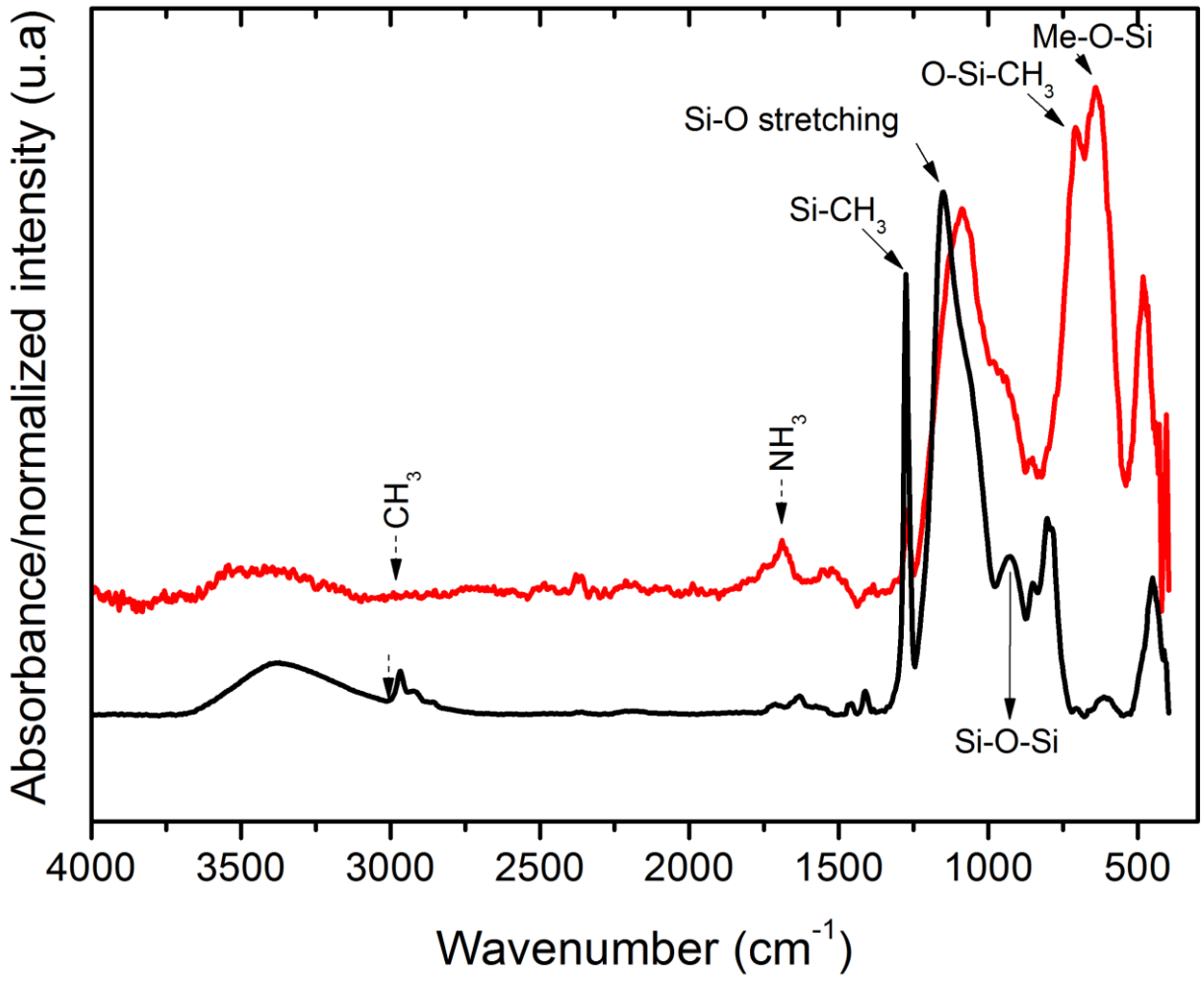

Figure 12: Comparison of IRRAS spectra on AISI430. In black color is shown a spectrum of pure ZN200 coating while the surface of AISI316 modified by ZN200 ultra-thin film (less than 10 nm-thick) is presented in red color.

IV.3.5. Adhesion mechanism between ZN200 and steel

XPS and IRRAS allow us to understand the chemical interaction between polysilazane precursors and the tested steel substrates. It was found that metallosiloxane (Me-O-Si) covalent bonds are formed between both materials, in agreement with others [21,25]. These metallosiloxanes found could be a result of chemical bonding of –Si–HN2– (in ZN200 polysilazane precursors) with hydroxyl groups detected on the surface of uncoated steel, as reported earlier in the case of silane complexes on steel [11]. Hence, ZN200 precursors probably react with steel surfaces according to the simplified reactions scheme [27] shown in figure 14:

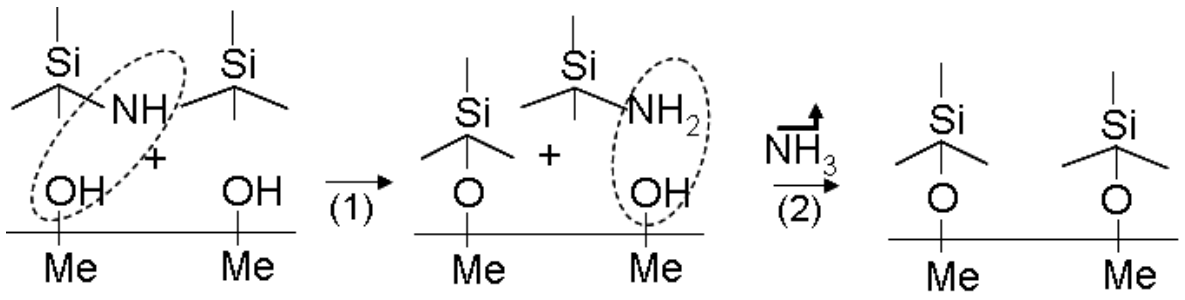

Figure 13: Simplified illustration of bonding mechanism between polysilazane and hydroxyl groups on the surface of SS substrates.

The presence of covalent Me-O-Si bonds can explain the good adhesion observed between ZN200 coatings and SS substrates. This has been tested according to ASTM D3359-07 standard test methods (figure 15). As it can be seen, no delamination is observed after cross-cut testing indicating that ZN200 hybrid-polymer adheres well to the steel substrate.

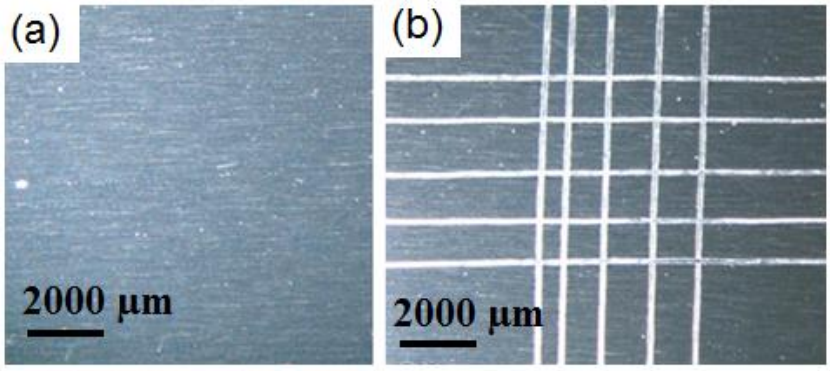

Figure 14: Surface image of SS substrate coated with ZN200 films (a) before adhesion test, (b) after ASTM D3359-07 adhesion standard test called cross-cut-test.

We demonstrated through these studies how well ZN200 coatings adhere to steel substrates. We are going to investigate in the following section the other interface between ZN200 and Mo films. It was shown in chapter 3 that Mo/ZN200 samples can be in view of adhesion classified in poorly adhered and well-adhered Mo/ZN200 samples. Hence, it was necessary to investigate the interface between ZN200 and Mo films to understand chemical interactions in order to explain adhesion between both materials.

IV.4. Part II: polysilazane and molybdenum interface analysis

In this section, we investigate the interface between ZN200 coatings and Mo films with especial emphasis on understanding adhesion loss with microstructure A and microstructure Bh. Ultra-thin Mo films (2-5 nm) are deposited on ZN200 coatings to probe the interface by XPS directly and to avoid long sputtering times in XPS depth profiles of Mo films.

IV.4.1. Preliminary studies

Prior to XPS analysis, AFM images were recorded to check the covering of ultra-thin Mo films. An example of topographic and phase image is given in the figure 16 for 2-5 nm-thick Mo films of microstructures B and Bh. A good coverage of Mo films is clearly seen.

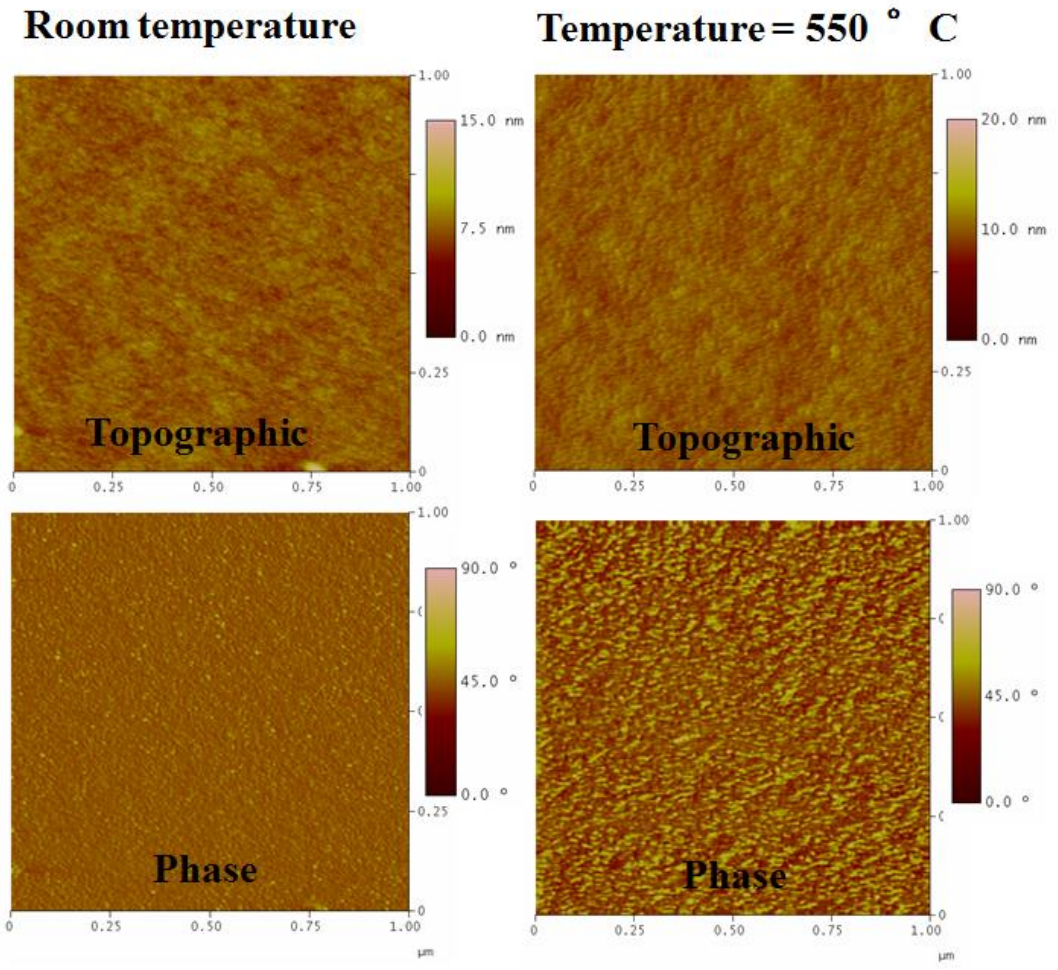

Figure 15: AFM images of microstructure B like Mo films (2-3 nm) deposited onto ZN200. (Left) Mo films are deposited at room temperature and (right) Mo films deposited onto substrates heated up to 550°C.

Depth profiles have been then recorded on these samples by alternating cycles of XPS measurements and sputtering of the Mo sub-coatings with Ar ions. The time needed to reach the interface (TRI) was evaluated for each sample using an argon ion beam at an incidence angle of 45° operating at 100 eV with a spot size of 200 × 200 μm^2. Samples were typically analyzed three times: as deposited (hereafter called "Area A"), after sputtering during TRI ("Area B") and after sputtering for a longer period, to probe the ZN200 coating itself ("Area C") as shown in the figure 17. One should mention that all samples were exposed to air before they could be measured by XPS.

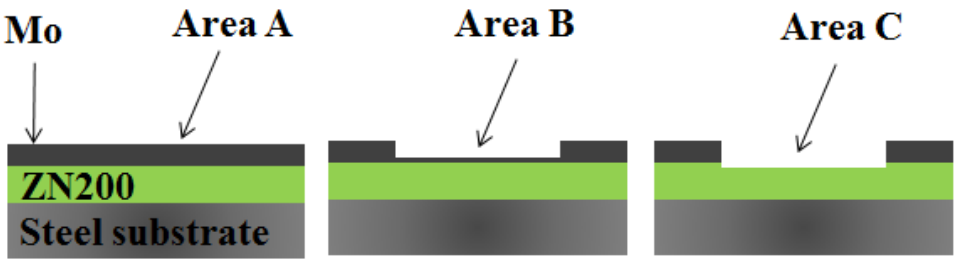

Figure 16: Illustration of areas analyzed on samples used for Mo/ZN200 interface analysis. In area A corresponding to as received sample, the interface between Mo and ZN200 coating is probed through 2-5 nm-thick Mo film; area B corresponds to area analyzed once Mo coating is etched and area C is related to inner ZN200 due to XPS successive profiling.

IV.4.2. Poorly adhered ZN200/Mo samples

Interface of either microstructure A or microstructure Bh like Mo films and ZN200 coatings (samples which often failed adhesion test) are analysed in this section.

IV.4.2.1. Interactions of microstructure A Mo films with ZN200 coating

XPS high resolution spectra of Mo 3d, O 1s, Si 2p and C 1s transitions are displayed in figure 18 for microstructure A like Mo films (Mo deposited at low pressure in room temperature). According to our fitting, Mo transition in "areas A" (as deposited samples) is mainly a combination of MoO_3 and Mo_2O_5 which are centered at binding energies of 233.0 and 232.0 eV respectively [26,27]. In the C1s transition, the important peaks are centered at 284.9 eV and 286.4 eV and are assigned to C-C (contamination) and C-N/C-O bonds respectively. Oxygen and silicon transitions seem to reveal a chemical bonding between Mo film and ZN200 coating since the main peaks at 102.8 eV (Si 2p) and 531 eV (O 1s) are attributed to Mo-O-Si.

After Mo sub-layer etching ("area B"), the stronger peak detected in "area A" for Mo oxides remarkably become smaller and the main peak detected in Mo transition is shifted to lower binding energy. Based on investigation in [28], peaks corresponding to either Mo_2C or Mo_2Si could appear at 228.5 eV. The smaller peak at 283.7 eV of Mo_2C in the "area A" is relatively higher in this area. Mo-O-Si in areas A and B are quite constant and could be related to homogenously distribution of this component at the interface.

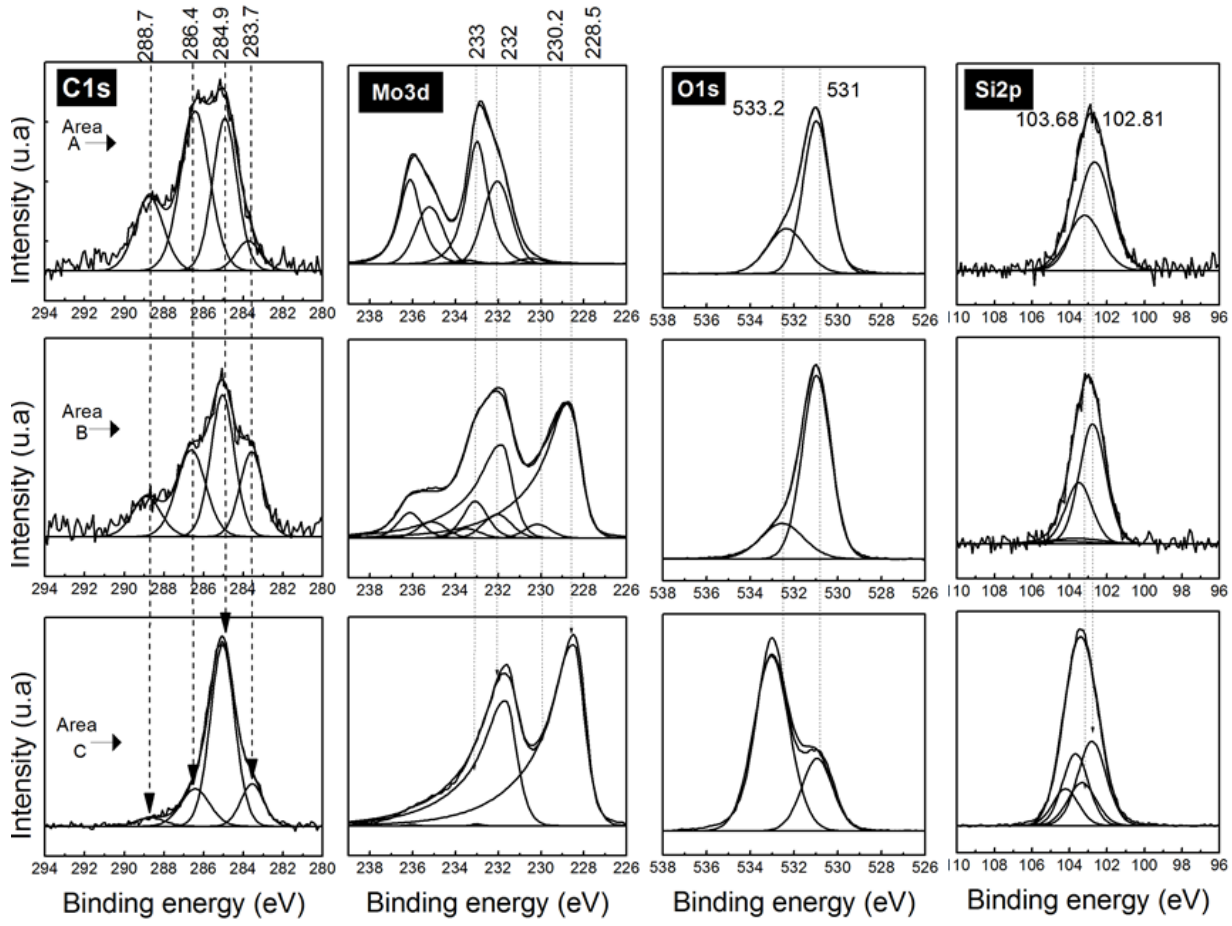

Figure 17: High resolution XPS of Mo 3d, C 1s, O 1s and Si 2p in zone A, Zone B and Zone C for 2-5 nm-thick Mo films deposited at 0.26 Pa on ZN200 coatings.

In "area C" and especially for Mo 3d transition, the peak of Mo-O-Si has disappeared and the main contribution is for Mo_2C. In O 1s transition, an inversion in intensity is clearly observed between SiO_2 (533.2 eV) [29] and Mo-O-Si peaks, and the SiO_2 peak becomes stronger. In Si 2p region also a peak centered at 103.7 eV corresponds to SiO_2. The presence of SiO_2 is probably related to ZN200.

All these results suggest the presence of a new chemistry different from both ZN200 and Mo at the interface. This could be attributed to the formation of a kind of ceramic tentatively assigned to a mix of $MoSiO_xC_y$ hard compounds.

IV.4.2.2. Interactions of microstructure Bh Mo films with ZN200 coating

Investigations have been also performed on the other poorly adhered sample, ZN200 coated with microstructure Bh like Mo film (Mo deposited on heated ZN200/SS) to check if the adhesion failure rises from chemistry change at the interface as previously found for Mo films deposited at low pressure. Thus, signals from C 1s, Mo 3d and Si 2p transitions in the three areas are fitted and compared as displayed in the figure 19.

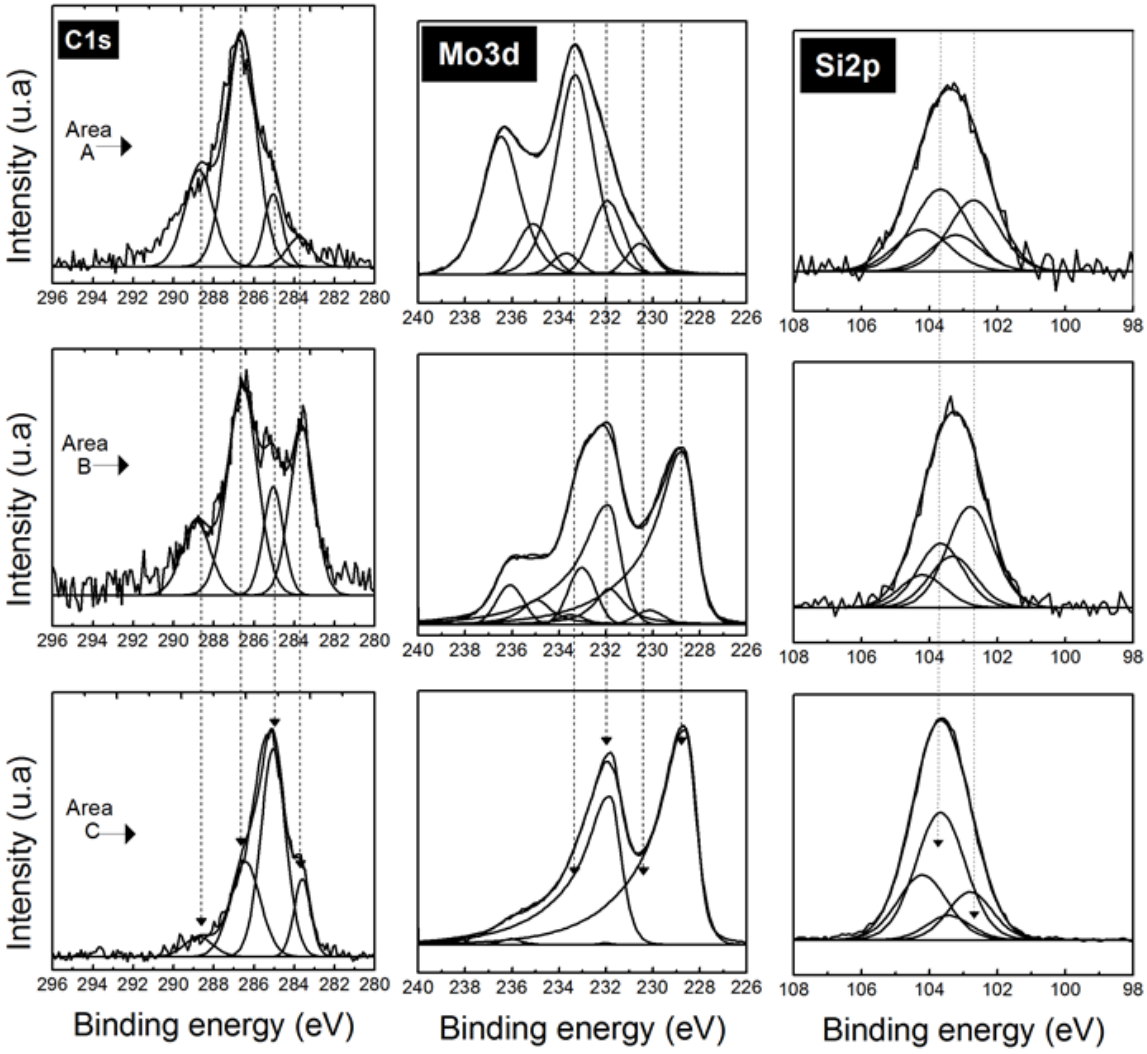

Figure 18: High resolution XPS of Mo 3d, C 1s and Si 2p in areas A, B and C for ZN00 film coated with ultra-thin (2-5 nm) microstructure Bh like Mo films.

Important compounds in the sample with respect to our fitting are summarized in the table 4. It can be found that these compounds are identical to those previously identified for microstructure A based sample. Additionally, the evolution of peak intensity in different areas seems to be also identical. Based on these analyses, one can deduce that the interface between Mo film and ZN200 coatings is probably forms of $MoSiO_xC_y$.

Table 4: Summary of main components in ZN00 coated the microstructure Bh like Mo films according to our fitting.

Composition	Lines	B.E (eV)	Ref.
Mo_2Si/Mo_2C	Mo 3d5/2	228.6	[30]
Mo_2N	Mo 3d5/2	230.3	[29]
Mo-O-Si	Si 2p3/2	102.8	[30]
Mo_2O_5	Mo 3d5/2	231.9	[29]
MoO_3	Mo 3d5/2	233.0	[29]

For further understanding of this type of interface, 300 nm microstructure Bh like Mo films are deposited. Mo films are then peeled off using adhesive tape as illustrated in figure 20, creating two surfaces ("tape" side and "steel" side), which are then analysed by XPS.

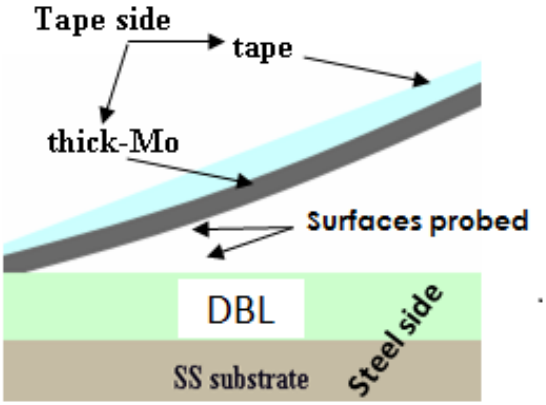

Figure 19: Illustration of Mo film's peeling off from ZN200 (DBL)/SS substrate in order to analyze the "tape" side and "steel" side using XPS

Figure 21.a shows XPS survey scans at seven different zones (from 1 to 7) arbitrarily chosen on "tape" side. As it can be observed, Mo 3d peak is clearly detected in zones (5), (6) and (7); traces of Mo 3d can be also seen in zones (1), (2) and (4). However, peaks related to Si 2p, Si 1s, N 1s and C 1s are detected in all analyzed zones and their intensities are significantly higher than that of Mo.

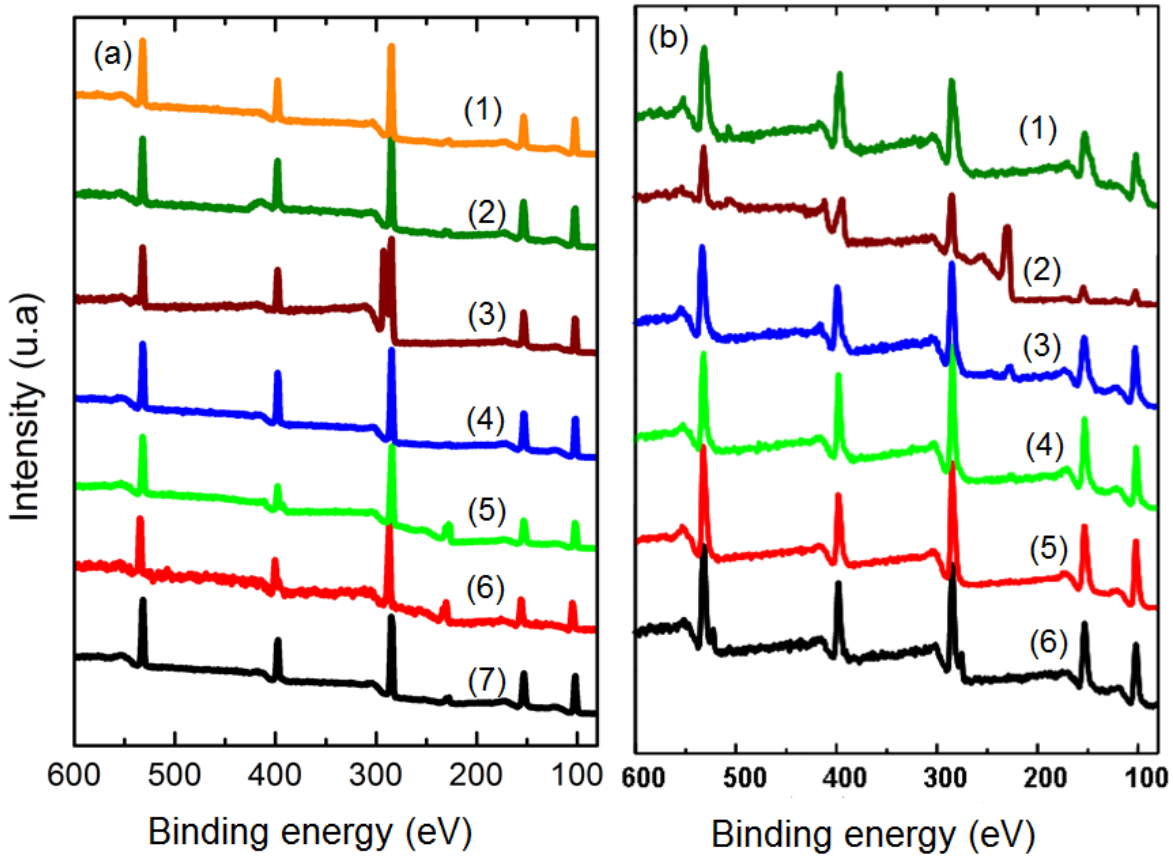

Figure 20: XPS surveys of interfaces of Mo/ZN00 sample after Mo films peeling off (a) the tape side and (b) steel side according to figure 18. There is no link between the positions of areas in figure a and b.

The composition of the "tape" side is determined using Si 2p, N 1s and Mo 3d transitions as summarized in the table 5. It is found that Si 2p and N 1s, both related to ZN200, correspond to more than 90 at. %. This implies that ZN200 coating is pulled off together with Mo.

Table 5: Compositions of silicon, nitrogen and molybdenum in "tape" side

Zones	Si 2p at.%	N 1s at.%	Mo 3d at.%
1	63.3	36.7	0
2	62.0	38.0	traces
3	63.3	36.7	0
4	61.2	38.8	0
5	70.3	23.2	6.48
6	69.3	28.1	2.67
7	64.0	35.9	traces

Another series of XPS survey scans have been also recorded at six different zones on the "steel" side. One should mention that there is no link between zones position numbering in both figures 21.a and b. Mo 3d peaks are clearly detected in zones (2) and (3) only and intensities are smaller than those detected for atoms related to ZN200. Any atoms from the SS substrate are not detected at all. Compositions in atomic percentage are summarized in the table 6 and indicated that the "steel" side is also in ZN200.

Table 6: Compositions of silicon, nitrogen and molybdenum in "steel" side

Zones	Si 2p at. %	N 1s at. %	Mo 3d at. %
1	62.2	37.8	0
2	62.4	37.6	0
3	63.3	36.6	traces
4	56.6	43.3	0.08
5	23.0	61.1	15.9
6	61.1	38.9	0

Based on both "tape" side and "steel" side analyses, we concluded that the adhesion loss occurs certainly within the ZN200 coating. This implies that Mo films adhere well to ZN200 coating and the good adhesion can be linked to covalent bonding at the interface. On the other hand, the decohesion may result from the weakening of ZN200 due to $MoSiO_xC_yN_z$ ceramic films newly formed at the interface. The fact that ZN200 film is still sticking to SS substrate consolidates the good adhesion of ZN200 and steel interface analysis even after annealing up to 550°C pointed out in part I.

IV.4.3. Well-adhered ZN200/Mo samples

Detailed XPS measurements have been performed on microstructure B like Mo films (which was a well adhered sample) to investigate reasons for the good adhesion and results are compared with these obtained with the poorly adhered samples. High resolution spectra of Mo 3d, O 1s, Si 2p and C 1s transitions are displayed in figure 22. Spectra are surprisingly quite similar to those obtained with poorly adhered samples, except for a small change in Mo 3d transitions. Compared to figures 19 and 20, Mo peaks are shifted to 0.4 eV higher binding. Thus, in area B especially, peaks at lower binding energy are centred at binding energies of 229.0 and 229.9 eV, and are assigned to MoO_2 and MoN_2, respectively. In poor adhered samples however, the peak at lower binding energy in area B was attributed to molybdenum carbide. The interfacial chemistry in this sample could be certainly a mixture of $MoSiO_xN_y$ compounds while a carbide ceramic was observed for samples with poor adhesion.

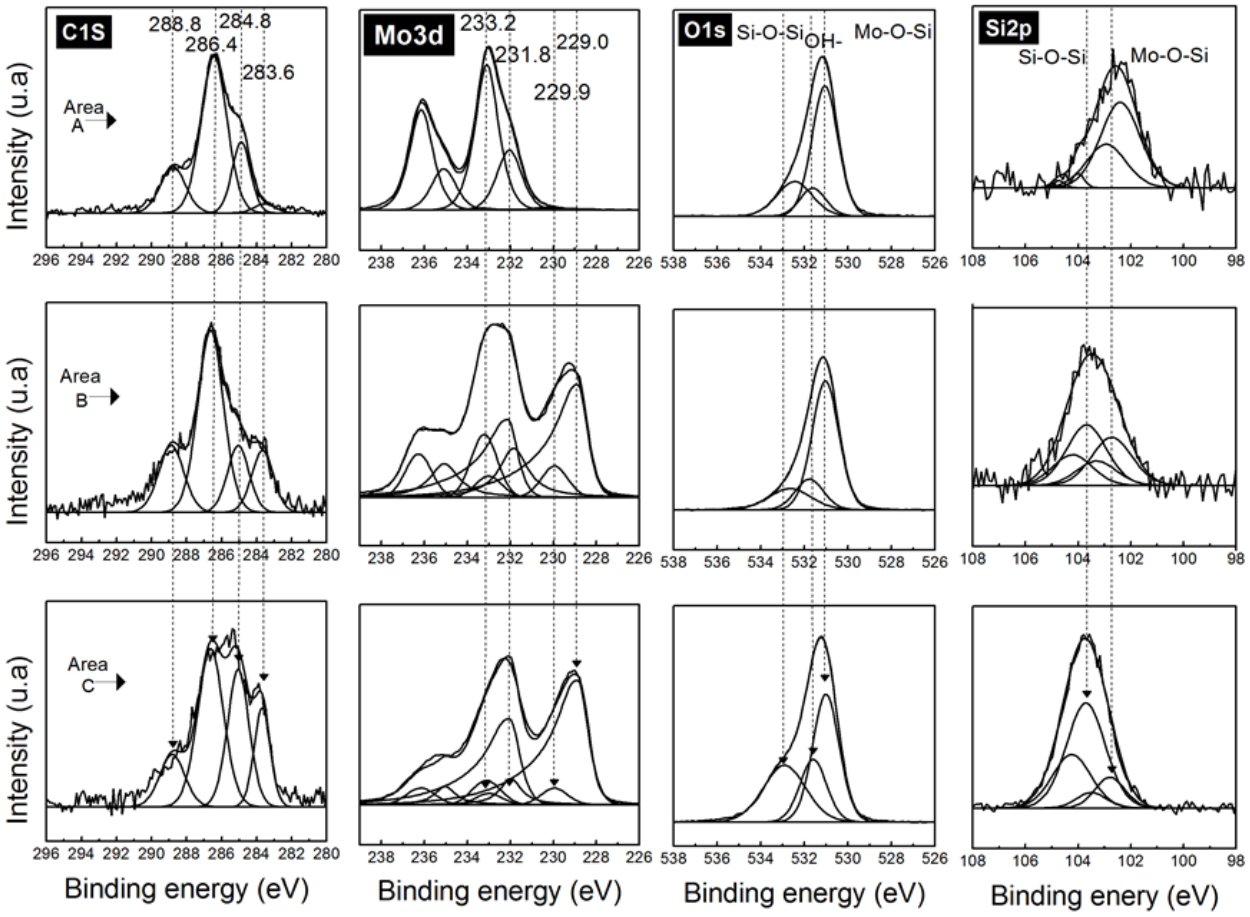

Figure 21: High resolution XPS of Mo3d, C1s, O1 and Si2p in zone A, Zone B and Zone C for 2-5 nm-thick Mo films deposited at 4 mTorr on PSP based coatings

IV.5. Summary

Surface analysis on steels reveals that thin natural oxide and hydroxide are formed on the top surface. Based on XPS depth profiling, Cr and Fe oxides probably co-exist in the native oxide detected at the top surface of our steels and the fact that these oxides are simultaneously detected excludes any stratification of both oxides. The analysis of steel modified by ultra-thin ZN200 using both XPS and IRRAS reveals the presence of Cr-O-Si and Fe-O-Si covalent bonds which may explain the good adhesion observed with ZN200/steel samples. Based on these investigations, an adhesion mechanism between steel and ZN200 precursors has been proposed.

Interfaces of a set of Mo films on ZN200 were also studied. There seems to be a link between Mo-O-Si covalent bonds and good adhesion at the interface. Adhesion loss of microstructure Bh

based sample occurred due to decohesion in ZN00 film itself. The decohesion is assigned to the weakening of ZN200 due to the formation of molybdenum carbide at the interface.

References

[1] D. Amouzou, J. Dumont, L. Fourdrinier, J-B. Richir, F. Maseri, R. Sporken, Thin Solid Films, 531-15 (2013) 535/540.

[2] C.-O.A. Olsson, D. Landolt, Electrochimica Acta 48 (2003) 1093/1104.

[3] C. Donik, A. Kocijan, D. Mandrino, I. Paulin, M. Jenko, B. Pihlar, Applied Surface Science 255 (2009) 7056/7061.

[4] R. Kirchheim, B. Heine, S. Hofmann, H. Hofsäas, Corrosion science 31 (1990) 573.

[5] R.O. Adams, A review of the stainless steel, Vacuum Science and Technology A (1) (1983)12/18.

[6] I. Saeki, H. Konno, R. Furuichi, T. Nakamura,K. Mabuchi, M. Itoh, corrosion science 40 (2/3) (1998) 191/200.

[7] A. James, Jr. Poston, V. Ranjani, Siriwardane, J.S. Dunning, Applied Surface Science 253 (2007) 4872/4885.

[8] S.E. Zeimniak, L.M. Anovitz, R.A. Castelli, W.D. Porter, Chemical Thermodynamics 39 (2007) 1472/1492.

[9] T-S. Shih,Y-S. Huang, C-F. Chen, Applied Surface Science 258 (2011)81/88.

[10] Y.J. Du, M. Damron, G. Tang, H. Zheng, C.-J. Chu, J. H. Osborne, Progress in Organic Coatings 41 (2001) 226/232.

[11] V. Palanivel, D. Zhu, W.J. van Ooij, Progress in Organic Coatings 47 (2003) 384/392.

[12] M.F. Montemora, M.G.S. Ferreira, Progress in Organic Coatings 60 (2007) 228/237.

[13] D. Zhu, W.J.V. Ooij, corrosion science 45 (2003) 2177/2197.

[14] D. Wang, G. P. Bierwagen, progess in organic coatings 64 (2009) 327/338.

[15] D. Pleul, R. Frenzel , M. Eschner, F. Simon, Anal. Bioanal. Chem. 375 (2003)1276/1281.

[16] B. Carriere - D. Brion - J. Escard - J.P. Deville, Journal of Electron Spectroscopy and Related Phenomena, 10 (1977) 85/91.

[17] A. Mekki, D. Holland, C.F. McConville, M. Salim, Journal of Non-Crystalline Solids 208 (1996) 267/276.

[18] I. Bertoti, A. Toh, M. Mohai, R. Kelly, G. Marletta, M. Farkas-Jahnke, Nuclear Instruments and Methods in Physics Research B 122 (1997) 510/513.

[19] M. E. Simonsen, C. Sonderby, Z. Li, E. G. Sogaard, J Mater Sci (2009) 44:2079/2088.

[20] J.H. Wang, P.T. Liu, T.S. Chang, T.C. Chang, L.J. Chen, Thin Solid Films 469-470 (2004) 393/397.

[21] Ki Do Kim, Sung Soo Kim, Yong-Ho Choa, and Hee Taik Kim, J. Ind. Eng. Chem., Vol. 13, No. 7, (2007) 1137/1141.

[22] A. L. Andrade, D. M. Souza, M. C. Pereira, J. D. Fabris, R. Z.Domingues, Cerâmica 55 (2009) 420/424.

[23] R. De Palma, S. Peeters, M.J. Van Bael, H. Van den Rul, K. Bonroy,W. Laureyn,J. Mullens,G. Borghs,G. Maes, Chem. Mater.19 (2007) 1821/1831.

[24] J.S.T. Mambrim, H.0. Pastore,C. U. Davanzo,E.J. S. Vichi,O. Nakamura,H. Vargasl, Chem. Mater. 5 (1993)166/173.

[25] M. Günther, T. Kraus, A. Dierdorf, D. Decker, W. Krenkel, G. Motz, European Ceramic Society 29 (2009) 2061/2068.

[26] L. Ovari, J. Kiss, Vacuum 80 (2005) 204/207.

[27] Zhengping Li, Lian Gao, Shan Zheng, Applied Catalysis A: General 236 (2002) 163/171.

[28] M. Herranen, A. Delblanc Bauer, J.-O. Carlsson, R.F. Bunshah, Surface and Coatings Technology 96 (1997) 245/254.

[29] D. J. Stacchiola, M. Baron, S. Kaya, J. Weissenrieder, S. Shaikhutdinov, H.-J. Freund, App. Phys. Letters, 011911 (2008) 92/94.

[30] J. Finster, E ;-D. Klinkenberg, J. Heeg, Vacuum 41 (190) 1586.

General conclusions

This exploratory work aimed to investigate appropriate dielectric systems and also the optimization of molybdenum layers as contacts for the fabrication of "high temperature" flexible CIGS solar cells on stainless steel substrates.

Firstly, a review of recent progress in flexible CIGS solar cells led to various observations. The high temperature treatment steps involved in the growth of CIGS absorbing layers limit the choice of suitable inexpensive substrates. It was shown that, of all tested substrates, the metallic substrates such as stainless steels are more attractive for "high temperature" flexible CIGS solar cells due to their quality/price ratio. However, steel sheets contain Fe or Ni atoms which were identified as contaminants for the CIGS absorbing layer thereby an additional layer should be interposed between the substrate and the active stacks to block the diffusion of such impurities. This layer is referred to as a diffusion barrier layer (DBL). Conventional CIGS solar cells manufactured on glass substrates do not need this additional layer. For solar cells intended to be monolithically interconnected on steel sheets, the DBL has to be an insulator to electrically isolate cells from each other. The success of electrical insulation is especially difficult because of the high temperature treatment step required for the growth of the CIGS layer.

Insulating barriers thicker than 10 µm, such as plasma CVD or PVD layers, high-temperature varnishes and enamel layers, were investigated. As they are thick, such barriers possess good electrical insulation, but often suffer from surface roughness, cracks and reduced flexibility. These disadvantages could be overcome by barrier layers thinner than 10 µm. The best barrier layer in the literature is certainly that obtained by K. Herz and co-workers with 6 µm-thick of combi-layers SiO_x (SiO_x (double sol-gel layers + stirring at 500°C)/three SiO_x layers (PECVD) or Al2O3 (sputtered)/ three SiO_x layers (PECVD)). Such combi-layers yield a good electrical insulation on Ti substrates since a breakdown voltage of > 300 V can be reached on the non-annealed coatings but worse on stainless steels. The fact that a cleaning step is required between each layer makes the process especially complex. Ceramics prepared with wet coating deposition techniques can be revealed as good candidates but their limitations arise mainly from the reduced flexibility. Thin ceramics can tolerate some conformability but are definitely porous therefore suffer from electrical isolation.

Polysilzanes widely used in industry for corrosion inhibition and high temperature resistance were identified as potential DBL in the fabrication of CIGS solar cells.

Two kinds of polysilazanes have been tested; the main difference between both products rises from their dry content. The first product referred as ZN100 has a dry content of 75 wt. % while the second once called ZN200 has a dry content of around 20 - 50 wt. %. A set of coatings with different thickness were prepared and tested on two kinds of steels substrates: AISI316 (austenitic) and AISI430 (ferritic). It was found that ZN100 based coatings are systematically cracked after annealing even the thinner of around 2.3 µm-thick. ZN200 being less viscous than ZN100, it definitely gives thinner films. ZN200 single layers are typically 0.5 - 1 µm-thick while the double layers are around 2 µm-thick. ZN200 single or double layers crack-free even after annealing. Based on these tests, it was concluded that the single layers of ZN100 are not suitable and hence we retained ZN200 as our core dielectric material.

Thus, ZN200 coatings were investigated using appropriate tools of characterization to evaluate structural, electrical and chemical properties with respect to requirements related to the fabrication of CIGS solar cells. Our efforts were focused on four important aspects for ZN200 coatings: electrical insulation, adhesion, thermal degradation and diffusion barrier properties. Important results can be summarized as following:

- TGA results reveal an important mass loss of around 25 wt. % for ZN200. The mass reduction was assigned to chemical transformations of ZN200 since a volatilizing of different gases and the evolution of solvent were clearly observed. Such degradations cause severe weakening of the dielectric strength. It was shown that ZN200 can be stabilized after annealing at 550°C.
- With suitable combination of three layers of ZN200 and a sputtered SiOxAly layer we succeeded to grow a crack-free dielectric stack with total thickness of more or less 4 µm. It was found that the stack has a good dielectric quality because all MIM capacitors based on it show a leakage current lower than the maximum leakage current fixed in this work (1×10^{-6} A/cm²). Constant voltage stress measurements reveal that the conduction mechanism in the dielectric is best described using Schottky emission theory which enables a better fit of the dielectric constants using log(J)-V semi-logarithmic representations. The calculated dielectric constant is 2.8. With time to breakdown

measurements, it was found that the dielectric can tolerate an applied voltage of 1000 V before annealing and 500 V after annealing. In AC mode characterizations, the frequency dependence of the real part of impedance is found to be well fitted using equivalent circuit consisting of a single parallel resistor Rp and a capacitor Cp network with a series resistor Rs and the fitting parameters are consistent with experimental data. The dielectric constant of 2.9 was calculated using capacitance extracted from fitting parameters and is in line with a model of equivalent dielectric constants for composite materials. Based on the dielectric performances combined with the thermal stability of the combi-layer one can conclude that it is better than existing barriers in the literature.

- Mo films were also optimized on our dielectric stacks. By varying the working pressure from 2.6 x 10^{-1} Pa to 2.6 Pa, transitions in Mo film microstructures were observed and four different microstructures were identified. The concept of classification adopted here is based on straightforward changing in microstructures thereby does not follow the well-known model presented by Thornton in 1986. The difference results in the fact that the temperature coupling required in Thornton's model is not necessary in ours. It was also found that Mo films deposited at 0.53 – 0.8 Pa are systematically cracked and the size of cracked domains vary with thickness. Evolution of such domains was investigated and found to obey a power law. For further understanding of Mo cracking, theories of tensile stress were used. Based on the fact that the minimum energy needed to crack a film corresponds to the energy of cohesion in the film combined with the fact that films crack creating free surface to minimize the stress, we deduce that the total free surface in thin films should increase with thickness. Considering cracked domains as hexagons and using the evolution of cracked domains as a function of thickness, we found that the total area generated after cracking increases with the thickness. This is in agreement with the model that we proposed. In summary, the optimization of Mo films allowed us to establish a method to produce crack-free and well-adhered Mo films. Two solutions were found and each solution was obtained by combining two different layers. Two solutions have been obtained by combining the well-adhered (10 nm-thick of type B films) with either 300 nm-thick of Mo films deposited at low pressure (named S1) or 300 nm-thick of Mo films deposited on the heated substrates at a pressure identical to type B films (called S2). Solutions pass adhesion testing and exhibit very low sheet resistance required for Mo

back contacts. S1 is similar to the solution proposed by Scofield et al. even if the pressure ranges are not exactly the same but has the advantage of being three times thinner. The thickness of Mo films used today in CIGS is typically 1 µm thus efforts are ongoing to reduce the thickness in view of a reduction in production cost and deposition time. To our knowledge, S2 has not previously been proposed in the literature.

- The interface between a set of Mo films and polysilazane was also studied. There seems to be a link between Mo-O-Si covalent bonds and good adhesion at the interface. Adhesion loss observed for some Mo/polysilazane samples occurred due to decohesion in polysilazane itself. The decohesion is assigned to the weakening of polysilazane due to the formation of molybdenum carbide at the interface. Finally, the analysis of steel modified by ultra-thin polysilazane reveals the presence of Cr-O-Si and Fe-O-Si covalent bonds which may explain the good adhesion observed with polysilzane/steel samples.